

## University of Southampton Research Repository ePrints Soton

Copyright © and Moral Rights for this thesis are retained by the author and/or other copyright owners. A copy can be downloaded for personal non-commercial research or study, without prior permission or charge. This thesis cannot be reproduced or quoted extensively from without first obtaining permission in writing from the copyright holder/s. The content must not be changed in any way or sold commercially in any format or medium without the formal permission of the copyright holders.

When referring to this work, full bibliographic details including the author, title, awarding institution and date of the thesis must be given e.g.

AUTHOR (year of submission) "Full thesis title", University of Southampton, name of the University School or Department, PhD Thesis, pagination

UNIVERSITY OF SOUTHAMPTON

# Leptoquark Production at Next-to-Leading Order

Jason Benjamin Hammett

*Presented for the degree of*

**Doctor of Philosophy**

*Southampton High Energy Physics*

Department of Physics and Astronomy

Faculty of Science

University of Southampton

November 2014

This version of the thesis was submitted for examination in November 2014,  
and may differ from later versions.

# ABSTRACT

University of Southampton,  
Faculty of Engineering, Science and Mathematics  
School of Physics and Astronomy

## DOCTOR OF PHILOSOPHY

“Leptoquark Production at Next-to-Leading Order”

by Jason Benjamin Hammett

In this thesis we study the effective leptoquark model of Buchmüller, Rückl and Wyler, focusing on a particular type of scalar ( $R_2$ ) and vector ( $U_1$ ) leptoquark. The primary aim is to perform the calculations for leptoquark production at next-to-leading order (NLO) to establish the importance of the NLO contributions and in addition to this to determine how effective the narrow-width-approximation (NWA) is at NLO.

For both the scalar and vector leptoquarks it is found that the NLO contributions are large, with the largest corrections occurring to the vector leptoquark calculations. For the scalar leptoquark it is found that the NWA provides a good approximation for determining the resonant peak, however the NWA is not as effective for the vector leptoquark - where large differences are observed at NLO. For both the scalar and vector leptoquarks it is found that there are large contributions away from the resonant peak, which are missing from the NWA results, and these make a significant difference to the total cross-section.

# Contents

<b>Declaration</b>	<b>x</b>
<b>Acknowledgements</b>	<b>xi</b>
<b>1 Introduction</b>	<b>1</b>
1.1 Where do Leptoquarks Come From? . . . . .	2
1.1.1 The $SU(5)$ Grand Unified Theory . . . . .	2
1.1.2 $SU(5)$ and Proton Decay . . . . .	4
1.2 A General Leptoquark Model . . . . .	5
1.2.1 Leptoquark Single and Pair Production . . . . .	9
1.2.2 Single Leptoquark Production and the NWA . . . . .	10
1.3 Motivation for Studying Leptoquark Production . . . . .	10
1.4 Including Next-to-Leading Order Corrections . . . . .	10
1.5 The Narrow-Width Approximation . . . . .	11
1.6 Thesis Plan . . . . .	15
<b>2 Perturbative QFT - Higher Order Corrections</b>	<b>16</b>
2.1 Loop Calculations . . . . .	17
2.1.1 Dimensional Regularisation . . . . .	17
2.1.2 Unitary Cuts - A Numerical Approach . . . . .	18
2.1.3 SAMURAI - A Unitary Cut Tool . . . . .	24
2.2 Bremsstrahlung Calculations . . . . .	26
2.2.1 The Dipole Subtraction Method . . . . .	27
2.3 Set-Up for Performing the Perturbative Calculations . . . . .	29

<b>3</b>	<b>Scalar Leptoquarks</b>	<b>31</b>
3.1	Helicity Projections . . . . .	32
3.2	Scalar Leptoquarks in the NWA . . . . .	33
3.2.1	Virtual Corrections to the Production Process . . . . .	33
3.2.2	Virtual Corrections to the Decay Process . . . . .	35
3.2.3	External Leg Corrections . . . . .	36
3.2.4	Preparing the Virtual Corrections for SAMURAI . . . . .	39
3.2.5	Bremsstrahlung Corrections to the Production Process . . . . .	41
3.2.6	Bremsstrahlung Corrections to the Decay Process . . . . .	47
3.2.7	Combining the Production and Decay Processes . . . . .	49
3.2.8	Additional NLO contributions in the NWA . . . . .	52
3.2.9	Validating the Results: The Ward-Takahashi identity . . . . .	54
3.2.10	Results in the NWA . . . . .	55
3.3	Scalar Leptoquarks: The Full Non-Factorisable Process . . . . .	67
3.3.1	Non-Factorisable Virtual Contributions . . . . .	68
3.3.2	Instabilities in the Non-Factorisable Virtual Corrections . . . . .	69
3.3.3	Non-Factorisable Bremsstrahlung Corrections . . . . .	72
3.3.4	Calculating the Cross-Section . . . . .	73
3.3.5	Additional Contributions to the Full Process . . . . .	74
3.3.6	Results for the Full Process . . . . .	75
<b>4</b>	<b>Vector leptoquarks</b>	<b>81</b>
4.1	Vector Leptoquarks in the NWA . . . . .	82
4.1.1	Virtual Corrections . . . . .	82
4.1.2	Bremsstrahlung Corrections . . . . .	83
4.1.3	Combining the Production and Decay Process . . . . .	85
4.1.4	Additional NLO Contributions . . . . .	86
4.1.5	Results in the NWA . . . . .	86
4.2	Vector Leptoquarks: The Full Non-Factorisable Process . . . . .	91
4.2.1	Non-Factorisable Contributions . . . . .	91
4.2.2	Additional Contributions to the Full Process . . . . .	92
4.2.3	Results for the Full Process . . . . .	92

<b>5</b>	<b>Conclusions</b>	<b>97</b>
5.1	Scalar Leptoquarks . . . . .	97
5.2	Vector Leptoquarks . . . . .	98
5.3	Future Work . . . . .	99
	<b>Appendices</b>	<b>100</b>
<b>A</b>	<b>Helicity Projection</b>	<b>101</b>
A.1	Projecting an Even Number of $\gamma$ -matrices . . . . .	101
A.2	Projecting an Odd Number of $\gamma$ -matrices . . . . .	103
A.2.1	Simplifying the Final Expression . . . . .	104
A.3	Generalising the Projection . . . . .	104
<b>B</b>	<b>Analytic Loop Calculations</b>	<b>105</b>
B.1	External Massless Fermions . . . . .	105
B.2	External Gluons . . . . .	107
B.3	External Scalar Leptoquarks . . . . .	109
B.4	External Vector Leptoquarks . . . . .	111
<b>C</b>	<b>Feynman Rules</b>	<b>113</b>
C.1	Standard Model . . . . .	113
C.2	Scalar Leptoquark . . . . .	115
C.3	Vector Leptoquark . . . . .	119
<b>D</b>	<b>External Leg Corrections</b>	<b>123</b>
D.1	External Leg Corrections: Scalar Leptoquark . . . . .	123
D.1.1	The Electron and Positron . . . . .	123
D.1.2	The Gluon . . . . .	124
D.1.3	The Leptoquark . . . . .	125
D.2	External Leg Corrections: Vector Leptoquark . . . . .	127
D.2.1	The Massless Fermions . . . . .	127
D.2.2	The Gluon . . . . .	127
D.2.3	The Leptoquark . . . . .	127

<b>E</b>	<b>Lorentz Invariant Phase-Spaces</b>	<b>129</b>
E.1	Phase-Spaces for Scattering Processes . . . . .	129
E.1.1	2-Body Phase-Space with a Massive Final State . . . . .	129
E.1.2	3-Body Phase-Space with a Massive Final State . . . . .	130
E.1.3	4-Body Phase-Space with Massless Final States . . . . .	131
E.2	Phase-Spaces for Decay Processes . . . . .	133
E.2.1	2-Body Phase-Space . . . . .	134
E.2.2	3-Body Phase-Space . . . . .	134
	<b>Bibliography</b>	<b>136</b>



# List of Figures

1.1	The leptoquark interactions of the $X$ and $Y$ bosons. These give a direct coupling between the quark and leptonic sectors. . . . .	4
1.2	The diquark interactions of the $X$ and $Y$ bosons showing the quark and anti-quark interactions. These interactions allow the transformation of quarks into anti-quarks - violating baryon number. This is indicated by the clashing fermion lines. . . . .	5
1.3	The $SU(5)$ model introduces possible decay channels for the proton. In this example $p \rightarrow \pi^0 + e^+$ via the exchange of an $X$ boson. . . . .	5
1.4	Diagrams representing LQ pair production, where the LQs are represented as scalars. . . . .	9
1.5	Diagrams representing single LQ production, where the lepton is represented as a double fermion line. . . . .	9
1.6	When a scattering process can be factorised into a production and decay process there will be a large contribution from the resonance of the intermediate massive particle. Any non-factorisable contributions will be non-resonant and therefore only add a small contribution to the process. . . . .	12
2.1	A general $n$ -point loop diagram illustrating the momenta flow around the loop. . . . .	19
2.2	A general $n$ -point integral can be “pinched” to give an effective 2-point topology where $P = p_1 + \dots + p_j$ . By performing the pinch the effective vertices $\mathcal{A}_1$ and $\mathcal{A}_2$ will now contain propagator denominators. . . . .	20

3.1	The factorisable contribution to $u+g \rightarrow e^-+e^++u$ with the production of an intermediate scalar LQ. This process will be useful for calculating NLO corrections in the NWA. . . . .	32
3.2	The leading-order contributions to $u+g \rightarrow e^-+R_2$ where the u-quark has colour $i$ , the LQ has colour $j$ and the gluon has Lorentz index $\mu$ and colour $a$ . . . . .	33
3.3	QCD bubble graphs for LQ production. . . . .	34
3.4	QCD triangle graphs for LQ production. . . . .	34
3.5	QCD box graphs for LQ production. Note: These graphs illustrate the different topologies, but do not show the in and out states in a consistent way. . . . .	35
3.6	Electroweak bubble graphs for LQ production. . . . .	35
3.7	Electroweak triangle graphs for LQ production. . . . .	36
3.8	Electroweak box graphs for LQ production. Note: These graphs illustrate the different topologies, but do not show the in and out states in a consistent way. . . . .	37
3.9	Leptoquark bubble graphs for LQ production. . . . .	37
3.10	Leptoquark triangle graphs for LQ production. . . . .	38
3.11	The leading-order contribution to $R_2 \rightarrow e^++u$ where the LQ has colour $i$ and the u-quark has colour $j$ . . . . .	38
3.12	QCD triangle graph for LQ decay. . . . .	39
3.13	Electroweak triangle graphs for LQ decay. . . . .	39
3.14	External leg corrections to the u-quark . . . . .	40
3.15	QCD bremsstrahlung corrections to the LQ production process. . . . .	42
3.16	QED bremsstrahlung corrections to the LQ production process. . . . .	43
3.17	A diagrammatic representation of the dipole subtraction term for an initial-state emitter and final-state spectator indicating the momenta and colours of the various external particles. . . . .	44
3.18	QCD bremsstrahlung corrections to the LQ decay process. . . . .	48
3.19	QED bremsstrahlung corrections to the LQ decay process. . . . .	49

3.20	The additional factorisable NLO contributions to the LQ production process. . . . .	53
3.21	An example process with an initial state singularity. In this example the singularity occurs when the radiated anti-quark becomes collinear to the internal quark line. . . . .	53
3.22	LO results for producing a scalar LQ - comparing the NWA to the full non-factorisable process (CTEQ6M). . . . .	55
3.23	NLO results for producing a scalar LQ - comparing the NWA to the full non-factorisable process (CTEQ6M). These results include the QCD corrections only. . . . .	56
3.24	NLO results for producing a scalar LQ in the NWA (CTEQ6M). These results include the electroweak corrections only, which are neglected in the full non-factorisable process. . . . .	57
3.25	NLO results for producing a scalar LQ - comparing the NWA to the full non-factorisable process (CTEQ6M). These results include the LQ corrections only. . . . .	58
3.26	Additional NLO results for producing a scalar LQ in the NWA (CTEQ6M). In addition to the QCD and LQ corrections these results include the EW corrections, which are neglected in the full non-factorisable process. . . . .	59
3.27	Total NLO results for producing a scalar LQ in the NWA (CTEQ6M). In addition to the QCD and LQ corrections these results include the EW corrections, which are neglected in the full non-factorisable process. . . . .	60
3.28	Total NLO results for producing a scalar LQ in the NWA comparing the CTEQ6M and CTEQ6L PDF sets. These results include the QCD and LQ corrections as well as the EW corrections. . . . .	61
3.29	Additional NLO results for producing a scalar LQ - comparing the NWA to the full non-factorisable process (CTEQ6M). These results include the QCD and LQ corrections only. . . . .	63
3.30	Total NLO results for producing a scalar LQ - comparing the NWA to the full non-factorisable process (CTEQ6M). These results include the QCD and LQ corrections only. . . . .	64

3.31	A comparison between the LO and NLO contributions for producing a scalar LQ in the NWA (CTEQ6M). These results include the QCD and LQ corrections only. . . . .	65
3.32	The factorisable LO contributions to the LQ production process. . . .	67
3.33	The non-factorisable LO contribution to the LQ production process. . .	67
3.34	An example factorisable NLO contribution to the LQ production process.	68
3.35	Non-factorisable QCD bubble graphs. . . . .	69
3.36	Non-factorisable QCD triangle graphs. . . . .	69
3.37	Non-factorisable QCD box graphs. Note: These graphs illustrate the different topologies, but do not show the in and out states in a consistent way. . . . .	70
3.38	Non-factorisable QCD pentagon graphs. Note: These graphs illustrate the different topologies, but do not show the in and out states in a consistent way. . . . .	71
3.39	Non-factorisable LQ bubble graphs. . . . .	71
3.40	Non-factorisable QCD bremsstrahlung graphs. . . . .	72
3.41	The additional LO process: $u + \bar{u} \rightarrow e^+ + e^- + g$ . . . . .	74
3.42	Additional LO results for producing a scalar LQ in the full non-factorisable process (CTEQ6M). . . . .	76
3.43	A comparison between the LO and NLO contributions for producing a scalar LQ in the non-factorisable process (CTEQ6M). . . . .	77
3.44	Total NLO results for producing a scalar LQ in the full non-factorisable process - comparing the CTEQ6M and CTEQ6L PDF sets. . . . .	78
3.45	The unstable contributions from graphs $NFBX_3$ and $NFP_3$ . . . . .	80
4.1	The modified $B_1$ topology for a vector LQ. . . . .	82
4.2	QCD, Goldstone and Faddeev-Popov ghost corrections to the LQ propagator. . . . .	83
4.3	The modified $T_5$ and $T_6$ topologies for a vector LQ. . . . .	83
4.4	QCD, Goldstone and Faddeev-Popov ghost corrections to the gluon-LQ triple-point vertex. . . . .	84
4.5	The modified $BX_2$ topology for a vector LQ. . . . .	85

4.6	LO results for producing a vector LQ - comparing the NWA to the full non-factorisable process (CTEQ6M). . . . .	87
4.7	NLO results for producing a vector LQ - comparing the NWA to the full non-factorisable process (CTEQ6M). . . . .	87
4.8	Additional NLO results for producing a vector LQ - comparing the NWA to the full non-factorisable process (CTEQ6M). . . . .	88
4.9	Total NLO results for producing a vector LQ - comparing the NWA to the full non-factorisable process (CTEQ6M). . . . .	89
4.10	A comparison between the LO and NLO contributions for producing a vector LQ in the NWA (CTEQ6M). . . . .	89
4.11	Total NLO results for producing a vector LQ in the NWA comparing the CTEQ6M and CTEQ6L PDF sets. . . . .	90
4.12	Additional LO results for producing a vector LQ in the full non-factorisable process (CTEQ6M). . . . .	93
4.13	A comparison between the LO and NLO contributions for producing a vector LQ in the non-factorisable process (CTEQ6M). . . . .	94
4.14	Total NLO results for producing a vector LQ in the full non-factorisable process - comparing the CTEQ6M and CTEQ6L PDF sets. . . . .	95
D.1	External leg corrections to the outgoing positron and electron. . . . .	123
D.2	External leg corrections to the incoming gluon. . . . .	124
D.3	External leg corrections to the leptoquark. . . . .	126
D.4	The external leg corrections to the gluon including the Goldstone boson and Faddeev-Popov ghost contributions. . . . .	128

# Declaration of Authorship

I, Jason Hammett, declare that this thesis, entitled ‘Leptoquark Production at Next-to-Leading Order’ and the work presented in it are my own. I confirm that

- This work was done wholly or mainly while in candidature for a research degree at this university.
- Where any part of this thesis has previously been submitted for a degree or any other qualification at this university or any other institution, this has been clearly stated.
- Where I have consulted the published work of others, this is always clearly attributed.
- Where I have quoted the work of others, the source is always given. With the exception of such quotations, this thesis is entirely my own work.
- I have acknowledged all main sources of help.
- Where the thesis is based on work done by myself jointly with others, I have made clear exactly what was done by others and what I have contributed myself.

*Note: At the time writing this thesis a paper giving the main results contain herein is in preparation.*

Signed:

Date:

# Acknowledgements

Firstly and most importantly I would like to thank my parents, without their continued support and encouragement I would never have been able to achieve the things I have done.

I would also like to thank my supervisor Doug Ross for supporting me throughout my PhD and helping me through the difficult periods of the project. Without his guidance and incredible scientific insight this thesis would not have been possible.

To all the friends I have made over the last few years, thank you for making Southampton a wonderful experience. I would especially like to thank my friends and colleagues in office 4005 - Marc Thomas, Jürgen Dietz, Shane Drury, Daniele Barducci, Miguel Romão and Juri Fiaschi - for making the office an intellectually stimulating environment and a lot of fun too.

And finally to Maria, for being there when I really needed a friend. Thank you for helping when I needed it the most.

— J.B.H.

# Chapter 1

## Introduction

With the success of the Glashow-Weinberg-Salam (GWS) model [1–3] - which unifies the electromagnetic and weak nuclear forces into a single electroweak theory - the holy grail of theoretical particle physics has been to develop a grand unified theory (GUT). Such a theory would further combine the electroweak force and the strong nuclear force into a single unifying symmetry: allowing us to describe these forces with a single set of laws.

One of the consequences of developing a GUT, however, is the introduction of additional particles beyond those we see in the standard model. One such additional particle is the leptoquark (LQ) and it is this particle which will be our focus.

The primary aim of this thesis is to study the process of LQ production, with the following key objectives:

- Compare the leading order (LO) and next-to-leading order (NLO) calculations of LQ production within the framework of perturbative quantum field theory.
- Study how effective the narrow-width approximation (NWA) is at approximating LQ production at both LO and NLO.

In this chapter we will start by discussing where LQs come from and then discuss the motivation for studying LQ production along with the importance of including NLO calculations. Finally we will describe the NWA and its use in studying LQ production.



## 1.1 Where do Leptoquarks Come From?

There are a number of different models which predict the existence of LQs, including general supersymmetric models with R-parity violation, extended technicolor models and composite models of quarks and leptons. In addition to these they are also predicted by various GUTs including the  $SU(4)$  Pati-Salam model [4] and the  $SU(5)$  Georgi-Glashow model [5]. Vector LQs would naturally arise as gauge bosons in GUT theories whereas scalar LQs would be found in other models such as supersymmetry with R-parity violation. To see more explicitly how LQs can appear in a model we will consider the  $SU(5)$  model of Georgi and Glashow.

### 1.1.1 The $SU(5)$ Grand Unified Theory

The  $SU(5)$  Georgi-Glashow model is a suitable GUT to use as an example since  $SU(5)$  is the smallest group that contains the standard model symmetry  $SU(3) \otimes SU(2) \otimes U(1)$ . We will give a brief introduction to this model and show how it naturally introduces gauge bosons which mix the quark and leptonic sectors i.e. giving rise to LQs.

The  $SU(5)$  model has one complication, in order to represent all of the matter content (i.e. all of the quarks and leptons), not only do we need to consider the fundamental representation  $\psi^\mu$  - a **5** representation of  $SU(5)$  - but also the antisymmetric tensor representation  $\psi^{\mu\nu}$  - a **10** representation. In the fundamental representation  $\psi^\mu$  is given by

$$\psi = \begin{pmatrix} \bar{d}_i \\ \nu_e \\ e^- \end{pmatrix} \quad (1.1)$$

In this representation  $\bar{d}_i$  is a colour triplet of  $\bar{d}$  quarks with  $i = 1 \dots 3$  representing the colour indices and  $\nu_e$  and  $e^-$  represent the electron neutrino and electron fields respectively.

*Note: The matter content in the  $SU(5)$  model is comprised of both left and right-handed particles and since the  $SU(5)$  gauge transformations do not mix the two*

*it is possible to treat all particles as having the same chirality - without adding any confusion. For notational convenience all of the fields in  $SU(5)$  are treated as left-handed and this is achieved by charge conjugating all of the right-handed fields. It is for this reason the right-handed  $d$ -quark in eq.(1.1) appears as charge-conjugated.*

In group notation eq.(1.1) can be represented by the quantum numbers

$$\psi \equiv (\bar{\mathbf{3}}, \mathbf{1}, 1/3) \oplus (\mathbf{1}, \mathbf{2}, -1/2) \quad (1.2)$$

where the quark is a triplet of  $SU(3)$  and a singlet of  $SU(2)$  with hypercharge  $1/3$  (representing a right-handed  $d$ -quark) and the lepton pair is an  $SU(3)$  singlet and an  $SU(2)$  doublet with hypercharge  $-1/2$  (representing the left-handed electron and electron neutrino).

From the interaction term of the covariant derivative, the gauge bosons of the theory can be represented by a set of twenty-four  $5 \times 5$  matrices. The 9 matrices, which are of the form

$$\begin{pmatrix} G & 0 \\ 0 & 0 \end{pmatrix} \quad (1.3)$$

(where  $G$  are  $3 \times 3$  matrices) represent the gluons and part of the  $U(1)$  gauge boson. In the fundamental representation the quark is an  $SU(3)$  triplet and  $SU(2)$  singlet and so this gives the QCD interaction of the right-handed  $d$ -quark.

The three matrices of the form

$$\begin{pmatrix} 0 & 0 \\ 0 & W \end{pmatrix} \quad (1.4)$$

(where  $W$  are  $2 \times 2$  matrices) represent the electroweak gauge fields. In the fundamental representation the leptons are  $SU(3)$  singlets and  $SU(2)$  doublets and this gives the electroweak interaction of the left-handed electron and electron neutrino.

The remaining fermions - the left and right-handed  $u$ -quarks, the left-handed  $d$ -quark and the right-handed electron - are in the anti-symmetric  $\mathbf{10}$  representation of  $SU(5)$ . The interaction of this representation with the gauge bosons generates

the QCD interactions between quarks of the same flavour and helicity as well as the charged weak interactions between  $u$ -quarks and  $d$ -quarks.

In addition to these twelve matrices there still remain an additional twelve matrices which make up the full  $SU(5)$  adjoint representation. These are the matrices which have the off-diagonal form

$$\begin{pmatrix} 0 & \bar{X} + \bar{Y} \\ X + Y & 0 \end{pmatrix} \quad (1.5)$$

It is these matrices which give a new set of gauge bosons: allowing direct mixing between the quark and leptonic sectors. Within  $SU(5)$  the new  $X$  and  $Y$  bosons (i.e. leptoquarks) provide a direct coupling between leptons and quarks (as shown in figure 1.1).

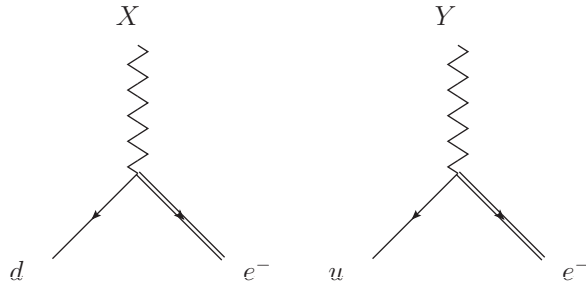


**Figure 1.1:** The leptoquark interactions of the  $X$  and  $Y$  bosons. These give a direct coupling between the quark and leptonic sectors.

### 1.1.2 $SU(5)$ and Proton Decay

The  $X$  and  $Y$  bosons also couple quarks and anti-quarks as shown in figure 1.2, in this case the leptoquarks behave like diquarks. Having both the leptoquark and diquark interactions presents a problem with the  $SU(5)$  model because it provides a channel for proton decay (see figure 1.3). In principle this is not a problem, however experimentally it is known that the lifetime of the proton is  $> 10^{31}$  years [6] and the only way to make  $SU(5)$  consistent with experiment is for the mass of the  $X$  and  $Y$  bosons to be of the order of the GUT scale i.e.  $\sim 10^{16}$  GeV. This restriction on the mass puts the energy far above anything we can probe with current collider

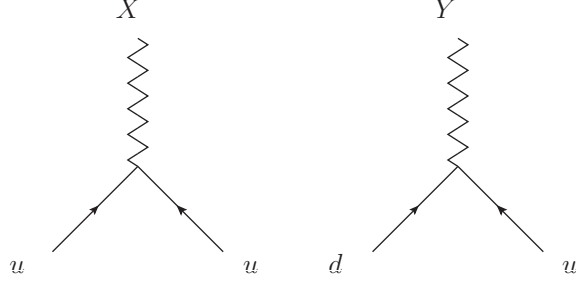


**Figure 1.2:** The diquark interactions of the  $X$  and  $Y$  bosons showing the quark and anti-quark interactions. These interactions allow the transformation of quarks into anti-quarks - violating baryon number. This is indicated by the clashing fermion lines.

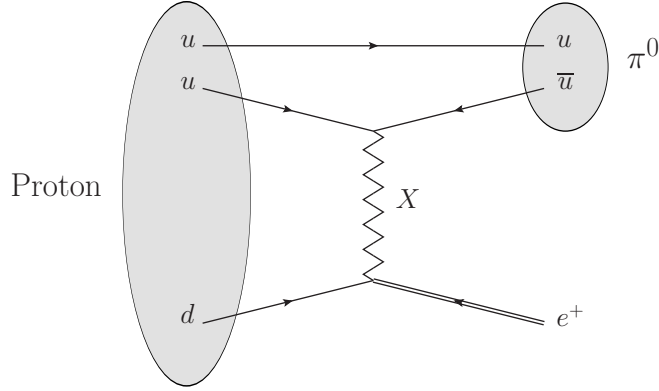


**Figure 1.3:** The  $SU(5)$  model introduces possible decay channels for the proton. In this example  $p \rightarrow \pi^0 + e^+$  via the exchange of an  $X$  boson.

technology. In order to make LQ production a suitable topic for study we need a model which does not restrict the LQ mass to such high energies.

## 1.2 A General Leptoquark Model

The reason the  $SU(5)$  GUT model introduces decay channels for the proton is because the theory does not conserve lepton and baryon number. Thus by considering a LQ model which *does* conserve these numbers the problem of proton decay can be avoided.

One such model - the one we will be using in this thesis - is the model of Buchmüller, Rückl and Wyler (the BRW model) [7]. In this model they consider an effective Lagrangian containing lepton and baryon number conserving LQs which are also consistent with the  $SU(3) \otimes SU(2) \otimes U(1)$  symmetry of the standard model. In

addition to this the model also uses flavour-diagonal LQ couplings, thereby removing the problem of flavour changing neutral currents.

Due to the lepton and baryon number conserving interactions of the LQs one of the main features of the BRW model is that it allows for a relatively light LQ mass without the problem of proton decay. Within the model the conservation of baryon and lepton number is achieved by restricting the type of LQ interactions which can appear. For each type of LQ the effective Lagrangian only allows one type of interaction with a quark and lepton. In terms of the Feynman rules this means that for a given type of LQ there is only one possible type of vertex. This restriction makes the BRW model lepton and baryon number conserving by construction.

Another feature of the BRW model is its bottom-up approach. Instead of considering a specific theory or set of theories which predict the existence of LQs they assume LQs do exist and then propose an effective model which includes all possible baryon and lepton number conserving LQs which are consistent with the standard model.

The BRW model includes both scalar and vector LQs and these fall into two categories: those with fermion number <sup>1</sup>  $|F| = 0$  and those with fermion number  $|F| = 2$ , see table 1.1. In total there are 10 different types of LQs:  $S_1$ ,  $\tilde{S}_1$ ,  $S_3$ ,  $R_2$  and  $\tilde{R}_2$  represent the scalar LQs and  $V_2$ ,  $\tilde{V}_2$ ,  $U_1$ ,  $\tilde{U}_1$  and  $U_3$  represent the vector LQs.

In the BRW model the effective Lagrangian for the interactions of LQs with leptons and quarks is

$$\mathcal{L}_{\text{quark+lepton}} = \mathcal{L}_{|F|=2} + \mathcal{L}_{|F|=0} \quad (1.6)$$

with

$$\begin{aligned} \mathcal{L}_{|F|=2} = & (g_{1L} \bar{q}_L^c i\tau_2 l_L + g_{1R} \bar{u}_R^c e_R) S_1 \\ & + \tilde{g}_{1R} \bar{d}_R^c e_R \tilde{S}_1 + g_{3L} \bar{q}_L^c i\tau_2 \tau l_L S_3 \\ & + (g_{2L} \bar{d}_R^c \gamma^\mu l_L + g_{2R} \bar{q}_L^c \gamma^\mu e_R) V_{2\mu} \\ & + \tilde{g}_{2L} \bar{u}_R^c \gamma^\mu l_L \tilde{V}_{2\mu} + \text{c.c.} \end{aligned} \quad (1.7)$$

---

<sup>1</sup>Fermion number  $F$  is defined as  $F = 3B + L$  where  $B$  and  $L$  are the baryon and lepton numbers respectively

	Spin	$ F $	$SU(3)$	$SU(2)$	$U(1)$	$T_3$	$Q_{\text{em}}$
$S_1$	0	2	$\bar{3}$	1	$+\frac{1}{3}$	0	$+\frac{1}{3}$
$\tilde{S}_1$	0	2	$\bar{3}$	1	$+\frac{4}{3}$	0	$+\frac{4}{3}$
$S_3$	0	2	$\bar{3}$	3	$+\frac{1}{3}$	+1	$+\frac{4}{3}$
						0	$+\frac{1}{3}$
						-1	$-\frac{2}{3}$
$V_2$	1	2	$\bar{3}$	2	$+\frac{5}{6}$	$+\frac{1}{2}$	$+\frac{4}{3}$
						$-\frac{1}{2}$	$+\frac{1}{3}$
$\tilde{V}_2$	1	2	$\bar{3}$	2	$-\frac{1}{6}$	$+\frac{1}{2}$	$+\frac{1}{3}$
						$-\frac{1}{2}$	$-\frac{2}{3}$
$R_2$	0	0	3	2	$+\frac{7}{6}$	$+\frac{1}{2}$	$+\frac{5}{3}$
						$-\frac{1}{2}$	$+\frac{2}{3}$
$\tilde{R}_2$	0	0	3	2	$+\frac{1}{6}$	$+\frac{1}{2}$	$+\frac{2}{3}$
						$-\frac{1}{2}$	$-\frac{1}{3}$
$U_1$	1	0	3	1	$+\frac{2}{3}$	0	$+\frac{2}{3}$
$\tilde{U}_1$	1	0	3	1	$+\frac{5}{3}$	0	$+\frac{5}{3}$
$U_3$	1	0	3	3	$+\frac{2}{3}$	+1	$+\frac{5}{3}$
						0	$+\frac{2}{3}$
						-1	$-\frac{1}{3}$

**Table 1.1:** Taken from [7] this table shows the quantum numbers for the various scalar and vector LQs in the BRW model. For example  $S_1$  is a scalar LQ which is a colour triplet of  $SU(3)$  and an electroweak singlet of  $SU(2)$  with hypercharge  $+1/3$ .

and

$$\begin{aligned}
\mathcal{L}_{|F|=0} = & (h_{2L} \bar{u}_R l_L + h_{2R} \bar{q}_L i\tau_2 e_R) R_2 + \tilde{h}_{2L} \bar{d}_R l_L \tilde{R}_2 \\
& + (h_{1L} \bar{q}_L \gamma^\mu l_L + h_{1R} \bar{d}_R \gamma^\mu e_R) U_{1\mu} \\
& + \tilde{h}_{1R} \bar{u}_R \gamma^\mu e_R \tilde{U}_{1\mu} + h_{3L} \bar{q}_L \tau \gamma^\mu l_L U_{3\mu} + \text{c.c.}
\end{aligned} \tag{1.8}$$

where  $q_L$  and  $l_L$  are the left-handed quark and lepton doublets respectively and  $e_R$ ,  $u_R$ ,  $d_R$  are the right handed charged leptons, u and d-quarks respectively.

For the interaction of scalar and vector LQs with gluons, the effective Lagrangian [8] is given by

$$\mathcal{L}_{\text{gluon}} = \mathcal{L}_S^g + \mathcal{L}_V^g \tag{1.9}$$

with

$$\mathcal{L}_S^g = \sum_{\text{scalars}} \left[ \left( D_{ij}^\mu \Phi^j \right)^\dagger \left( D_\mu^{ik} \Phi_k \right) - M_S^2 \Phi^{i\dagger} \Phi_i \right] \tag{1.10}$$

and

$$\begin{aligned}
\mathcal{L}_V^g = \sum_{\text{vectors}} \left\{ -\frac{1}{2} V_{\mu\nu}^{i\dagger} V_i^{\mu\nu} + M_V^2 \Phi_\mu^{i\dagger} \Phi_i^\mu \right. \\
\left. - ig_s \left[ (1 - \kappa_G) \Phi_\mu^{i\dagger} t_{ij}^a \Phi_\nu^j \mathcal{G}_a^{\mu\nu} + \frac{\lambda_G}{M_V^2} V_{\sigma\mu}^{i\dagger} t_{ij}^a V_\nu^{j\mu} \mathcal{G}_a^{\nu\sigma} \right] \right\}
\end{aligned} \tag{1.11}$$

where  $g_s$  is the strong coupling constant,  $t_a$  are the generators of  $SU(3)$  and  $M_S$  and  $M_V$  are the scalar and vector LQ masses respectively. The parameters  $\kappa_G$  and  $\lambda_G$  are related to the anomalous magnetic and quadrupole moments of the vector LQ and for the purpose of this thesis we set  $\kappa_G = 1$  and  $\lambda_G = 0$ . The scalar and vector LQ fields are  $\Phi$  and  $\Phi^\mu$  respectively and the field strength tensors of the gluon and vector LQ fields are

$$\mathcal{G}_{\mu\nu}^a = \partial_\mu G_\nu^a - \partial_\nu G_\mu^a + g_s f^{abc} G_{\mu b} G_{\nu c} \tag{1.12}$$

and

$$V_{\mu\nu}^i = D_\mu^{ik} \Phi_{\nu k} - D_\nu^{ik} \Phi_{\mu k} \tag{1.13}$$

with the covariant derivative given by

$$D_\mu^{ij} = \partial_\mu \delta^{ij} - ig_s t_a^{ij} G_\mu^a \quad (1.14)$$

### 1.2.1 Leptoquark Single and Pair Production

In the paper by Belyaev et. al. [9] the BRW model is studied: making a comparison between single LQ production and pair production. LQ pair production is a result of quark-antiquark or gluon-gluon interactions (see figure 1.4) whereas single LQ production results from (anti-)quark-gluon interactions (see figure 1.5). In both of these cases the signatures are the same, giving either:

- 2 leptons + jets
- 1 lepton + jets + missing transverse energy
- jets + missing transverse energy

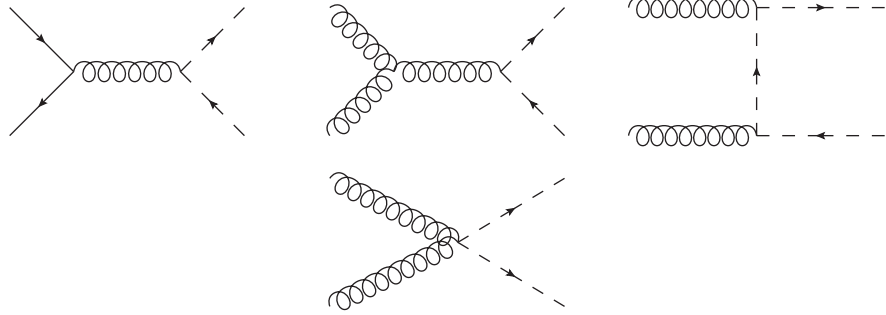


**Figure 1.4:** *Diagrams representing LQ pair production, where the LQs are represented as scalars.*

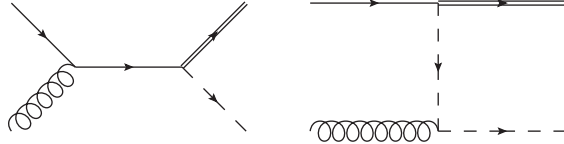


**Figure 1.5:** *Diagrams representing single LQ production, where the lepton is represented as a double fermion line.*

Since the signatures are the same it is not experimentally possible to separate out the two types of processes. However in their study Belyaev et. al. showed that for both scalar and vector LQs pair production dominates for low LQ masses (i.e.  $m_{LQ} \sim 100 \text{ GeV}$ ) and as the mass is increased single production becomes the more



dominant contribution.

### 1.2.2 Single Leptoquark Production and the NWA

One of the key objectives of this thesis is to study the effectiveness of the NWA at NLO. As detailed in section 1.5 the NWA is only valid when a *single* massive particle (with a narrow decay-width) is produced, for this reason the focus of this thesis will be on single LQ production.

Due to the large number of possible LQs (see table 1.1) we will focus our study on only two, choosing a scalar ( $R_2$ ) and a vector ( $U_1$ ) - both of these have fermion number  $|F| = 0$ .

## 1.3 Motivation for Studying Leptoquark Production

As already mentioned there are number of different models which predict the existence of LQs and searching for them will be a good test of beyond the standard model (BSM) physics. Also, with the development of the LHC we are now able to perform particle collisions at higher energies than ever before and are entering the energy region where we may start seeing evidence of LQs.<sup>2</sup>

It should be emphasised that the LHC can only test for BSM particles in the mass range of about 500 - 1000 GeV. This restriction makes the  $SU(5)$  Georgi-Glashow model unsuitable for study, but is ideal for the BRW model which allows a much lower LQ mass.

## 1.4 Including Next-to-Leading Order Corrections

A perturbative quantum field theory calculation can essentially be thought of as a series expansion: with the LO calculations being the lowest order in terms of the coupling constant and the NLO calculations being the next highest order, and so on.

---

<sup>2</sup>The search for LQs is an important consideration for the ATLAS and CMS experiments at the LHC. See for example [10–13].

The squared matrix element for a perturbative calculation will, in general, have the form

$$|\mathcal{A}|^2 = \alpha |\mathcal{A}_{\text{LO}}|^2 + \alpha^2 |\mathcal{A}_{\text{NLO}}|^2 + \dots \quad (1.15)$$

where  $\alpha = \frac{g^2}{4\pi}$  and  $g$  is the coupling. Within perturbation theory the first few terms of the series appear to converge and when considering weakly coupled interactions (where  $\alpha \ll 1$ ) the leading order term will tend to give a good approximation, however for strongly coupled interactions the NLO contributions become more important.

From a theoretical point of view including NLO corrections improves the accuracy of perturbative calculations (especially when considering strongly coupled interactions), but these corrections also become important when making a comparison with experimental results. The reason for this being that experimental particle physics is now being done at a higher precision than ever before and it is important to match this precision in our calculations.

## 1.5 The Narrow-Width Approximation

Performing theoretical calculations can be a time consuming process and theorists often resort to approximations to simplify the job. One particular type of approximation, which we will discuss here, is the narrow-width approximation (NWA).

The NWA is an important approximation to consider when studying the production of a massive particle, such as a LQ, as there is the subsequent decay into lighter particles. The NWA assumes that, in the process of scattering into the decay products of the massive particle, the production of a single intermediate LQ is the dominant state. The reason for this is two-fold:

- The decay-width of the particle is narrow and so the dominant contribution will come from kinematic region where the invariant mass of the intermediate state is close to the mass of the intermediate particle.
- States with more than one intermediate particle will not produce a resonance near this mass and will therefore only add a small contribution.

Under these assumptions the dominant contribution to the process can be factorised into a production amplitude  $\mathcal{A}_{\text{prod}}$  and a decay amplitude  $\mathcal{A}_{\text{decay}}$  - this is shown schematically in figure 1.6. Within the NWA the amplitude for this process can be

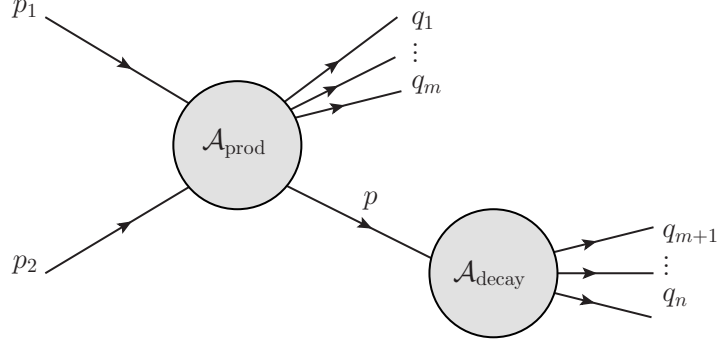


**Figure 1.6:** When a scattering process can be factorised into a production and decay process there will be a large contribution from the resonance of the intermediate massive particle. Any non-factorisable contributions will be non-resonant and therefore only add a small contribution to the process.

written as

$$\begin{aligned} \mathcal{A}(p_1, p_2 \rightarrow q_1 \cdots q_n) = \sum_{\lambda} \frac{1}{\sqrt{Z}} \mathcal{A}_{\text{prod}}(p_1, p_2 \rightarrow q_1 \cdots q_m, p; \lambda) \times \frac{i}{p^2 - m_0^2 + \Sigma(p^2)} \\ \times \frac{1}{\sqrt{Z}} \mathcal{A}_{\text{decay}}(p \rightarrow q_{m+1} \cdots q_n; \lambda) \end{aligned} \quad (1.16)$$

with the momenta  $p_i$  and  $q_i$  as shown in figure 1.6 and where (in general) the internal particle with momentum  $p$  will have helicity  $\lambda$ . The full amplitude  $\mathcal{A}$  is constructed by multiplying the production amplitude  $\mathcal{A}_{\text{prod}}$  and the decay amplitude  $\mathcal{A}_{\text{decay}}$  with the propagator for the intermediate massive particle and summing over the intermediate particle's helicity.

The massive propagator is expressed in terms of the bare mass  $m_0$  and includes loop corrections: contained within the self-energy term  $\Sigma(p^2)$ . Being part of a larger amplitude  $\mathcal{A}$  the internal legs of the production and decay parts would clearly not have external leg corrections (see section 3.2.3), however we want to treat the production and decay amplitudes,  $\mathcal{A}_{\text{prod}}$  and  $\mathcal{A}_{\text{decay}}$ , as complete processes which do include these external leg corrections. To make  $\mathcal{A}_{\text{prod}}$  and  $\mathcal{A}_{\text{decay}}$  consistent with  $\mathcal{A}$  a factor  $\frac{1}{\sqrt{Z}}$  needs to be included for each amplitude (where  $Z$  is the wavefunction renormalisation factor for the massive internal particle).

The propagator connecting the production and decay amplitudes can be written as

$$\frac{1}{p^2 - m_0^2 + \Sigma(p^2)} \approx \frac{Z}{p^2 - m^2 + im\Gamma^{\text{tot}}} \quad (1.17)$$

where  $m$  is the on-shell renormalised mass and  $\Gamma^{\text{tot}}$  is the total decay-width of the particle. Using this, the amplitude in eq.(1.16) can be rewritten as

$$\begin{aligned} \mathcal{A}(p_1, p_2 \rightarrow q_1 \cdots q_n) &\approx \sum_{\lambda} \mathcal{A}_{\text{prod}}(p_1, p_2 \rightarrow q_1 \cdots q_m, p; \lambda) \times \frac{i}{p^2 - m^2 + im\Gamma^{\text{tot}}} \\ &\times \mathcal{A}_{\text{decay}}(p \rightarrow q_{m+1} \cdots q_n; \lambda) \end{aligned} \quad (1.18)$$

and so the cross section (for massless initial state particles) is

$$\sigma = \frac{1}{2s} \int \prod_{i=1}^n \frac{d^4 q_i}{(2\pi)^3} \delta(q_i^2 - m_i^2) (2\pi)^4 \delta^{(4)} \left( p_1 + p_2 - \sum_{i=1}^n q_i \right) \left| \sum_{\lambda} \frac{\mathcal{A}_{\text{prod}} \times \mathcal{A}_{\text{decay}}}{p^2 - m^2 + im\Gamma^{\text{tot}}} \right|^2 \quad (1.19)$$

The first approximation of the NWA is to assume that the interference between  $\mathcal{A}_{\text{prod}}$  and  $\mathcal{A}_{\text{decay}}$  for different  $\lambda$  is negligible. This approximation allows the sum over helicities in eq.(1.19) to be taken outside the entire expression. By doing this and inserting unity in the form

$$1 = \int \frac{d^4 q}{(2\pi)^3} (2\pi)^4 \delta^{(4)}(q - p) \int \frac{dp^2}{(2\pi)} \delta(q^2 - p^2) \quad (1.20)$$

the cross-section can be rewritten as

$$\sigma \approx \sum_{\lambda} \frac{m}{\pi} \int dp^2 \frac{\sigma_{\text{p}}(p_1, p_2 \rightarrow q_1 \cdots q_m, q; \lambda) \times \Gamma(q \rightarrow q_{m+1} \cdots q_n; \lambda)}{(p^2 - m^2)^2 + m^2(\Gamma^{\text{tot}})^2} \quad (1.21)$$

with  $q^2 = p^2$  and where the quantities  $\sigma_{\text{p}}$  and  $\Gamma$  are

$$\begin{aligned} \sigma_{\text{p}}(p_1, p_2 \rightarrow q_1 \cdots q_m, q; \lambda) &= \frac{1}{2s} \int \prod_{i=1}^m \frac{d^4 q_i}{(2\pi)^3} \delta(q_i^2 - m_i^2) \frac{d^4 q}{(2\pi)^3} \delta(q^2 - p^2) \\ &\quad (2\pi)^4 \delta^{(4)} \left( p_1 + p_2 - \sum_{i=1}^m q_i - q \right) \\ &\quad |\mathcal{A}_{\text{prod}}(p_1, p_2 \rightarrow q_1 \cdots q_m, q; \lambda)|^2 \end{aligned} \quad (1.22)$$

and

$$\Gamma(q \rightarrow q_{m+1} \cdots q_n; \lambda) = \frac{1}{2m} \int \prod_{i=(m+1)}^n \frac{d^4 q_i}{(2\pi)^3} \delta(q_i^2 - m_i^2) (2\pi)^4 \delta^{(4)}(q - \sum_{i=(m+1)}^n q_i) |\mathcal{A}_{\text{decay}}(q \rightarrow q_{m+1} \cdots q_n; \lambda)|^2 \quad (1.23)$$

The second approximation of the NWA is to assume that the total decay-width  $\Gamma^{\text{tot}}$  is narrow (i.e.  $\Gamma^{\text{tot}} \ll m$ )<sup>3</sup>. This means the intermediate propagator  $\frac{1}{(p^2 - m^2)^2 + m^2(\Gamma^{\text{tot}})^2}$  can be approximated by a Dirac  $\delta$  function and the production and decay parts of the process can be treated as being on-shell (i.e. with  $q^2 = m^2$ ). In this situation the quantities  $\sigma_{\text{p}}$  and  $\Gamma$  can be considered as a production cross-section and decay-width respectively. Using this approximation the integral over  $p^2$  can be done separately to give

$$\int_0^\infty dp^2 \frac{1}{(p^2 - m^2)^2 + m^2(\Gamma^{\text{tot}})^2} \approx \frac{\pi}{m\Gamma^{\text{tot}}} \quad (1.24)$$

The final result for the cross-section can therefore be approximated by

$$\sigma \approx \sum_{\lambda} \sigma_{\text{p}}(p_1, p_2 \rightarrow q_1 \cdots q_m, q; \lambda) \times \left. \frac{\Gamma(q \rightarrow q_{m+1} \cdots q_n; \lambda)}{\Gamma^{\text{tot}}} \right|_{q^2=m^2} \quad (1.25)$$

and can be thought of as an on-shell production cross-section multiplied by the branching ratio for the massive intermediate particle.

In addition to the above mentioned assumptions, the studies by Kauer et. al. [14–16] identify other factors which need to be considered when using the NWA. These include the effect of non-factorisable contributions and the break-down of the NWA when the decay involves a daughter mass that approaches the mass of the parent particle. The effect of non-factorisable contributions will be an important part of this thesis, however the second consideration does not affect LQ production in the NWA since the LQ decay products are assumed to be massless in the high energy limit.

---

<sup>3</sup>For both scalar and vector LQs the decay-width is  $\sim 5\%$  of the LQ mass - see eq.(3.46) and eq.(4.6). This validates the use of the NWA in studying LQ production

## 1.6 Thesis Plan

Having motivated the study of LQ production at NLO the plan for the rest of this thesis is as follows:

- Chapter 2 will discuss the divergences that are usually encountered with NLO corrections and then detail the numerical tools and techniques used to deal with these.
- Chapters 3 and 4 are the key chapters of the thesis and will respectively discuss a scalar and vector LQ process.
- Chapter 5 will conclude the thesis with an analysis and comparison of the results from chapters 3 and 4.

## Chapter 2

# Perturbative QFT - Higher Order Corrections

The higher order corrections discussed in this chapter refer to next-to-leading order (NLO) corrections, and are comprised of two types: virtual corrections and bremsstrahlung corrections.

The virtual corrections at NLO are the one-loop Feynman diagrams and involve performing an integration over a loop momentum  $k$ . For some loop diagrams, when  $|k| \rightarrow \pm\infty$ , the integration diverges - known as an ultraviolet divergence - which can be removed by implementing a suitable renormalisation scheme.

At the other extreme, when  $|k| \rightarrow 0$ , some of the loop diagrams will experience divergences known as soft divergences. Also when  $k^2 \rightarrow 0$  and the particle runs parallel to a massless external particle some of the diagrams will experience collinear divergences. Collectively these types of divergences are known as infrared divergences and they are not removed by the process of renormalisation. Instead these can be removed by including the bremsstrahlung corrections. The bremsstrahlung corrections also have infrared divergences and when they are combined with the virtual corrections the divergences cancel.

## 2.1 Loop Calculations

We will focus first on the 1-loop virtual corrections and how their ultraviolet and infrared divergences can be regularised (i.e. separated from the finite part of the result) using a numerical approach.

### 2.1.1 Dimensional Regularisation

The simplest way to regularise the divergences in loop integrals is to introduce ultraviolet and infrared cut-offs to the integration limits, however this method has the consequence of breaking gauge invariance. A preferred method, which maintains gauge invariance, is to use dimensional regularisation.

Using Feynman parametrisation any loop integral can be written in the form

$$I = \int \frac{d^4k}{(2\pi)^4} \frac{\mathcal{N}(k)}{(k^2 - \Delta)^n} \quad (2.1)$$

where  $\mathcal{N}(k)$  is the loop numerator, which is polynomial in  $k$ , and  $\Delta$  is a constant term with respect to  $k$ . The denominator is raised to a power  $n$  which depends on the topology of the loop, a loop with a single vertex (a tadpole loop) would have  $n = 1$  and loop with two vertices (a bubble loop) would have  $n = 2$  and so on.

This 4-dimensional integral can be generalised to the  $d$ -dimensional case and in the case where  $\mathcal{N}(k)$  is independent of  $k$  or quadratic in  $k$  the integral can be written as

$$\int \frac{d^d k}{(2\pi)^d} \frac{1}{(k^2 - \Delta)^n} = \frac{(-1)^n i}{(4\pi)^{d/2}} \frac{\Gamma(n - \frac{d}{2})}{\Gamma(n)} \left(\frac{1}{\Delta}\right)^{n - \frac{d}{2}} \quad (2.2)$$

or

$$\int \frac{d^d k}{(2\pi)^d} \frac{k^2}{(k^2 - \Delta)^n} = \frac{(-1)^{n-1} i}{(4\pi)^{d/2}} \frac{d}{2} \frac{\Gamma(n - \frac{d}{2} - 1)}{\Gamma(n)} \left(\frac{1}{\Delta}\right)^{n - \frac{d}{2} - 1} \quad (2.3)$$

respectively. In these examples the left-hand side of eq.(2.2) or eq.(2.3) are only defined in an integer number of dimensions, however the right hand side can be analytically continued to complex  $d$  and the ultraviolet and infrared divergences manifest themselves as poles at  $d = 4$ . By evaluating the integrals in the limit  $d \rightarrow 4$  the divergences in these integrals can be regularised. The usual convention is to set



$d = 4 - 2\epsilon$  and then take the limit  $\epsilon \rightarrow 0$ , which in general gives a result of the form

$$I = \frac{i}{16\pi^2} \left[ \frac{A}{\epsilon^2} + \frac{B}{\epsilon} + C \right] \quad (2.4)$$

The first two terms are divergent quantities in the limit  $\epsilon \rightarrow 0$ . The first term (the double pole) is due to the the infrared divergence and the second term (the single pole) is due to both ultraviolet and infrared divergences. The final term (the finite part) always contains Euler's constant  $\gamma$  and  $\log(4\pi)$ , in the  $\overline{\text{MS}}$ -bar scheme these two terms are eliminated from eq.(2.4) by multiplying by the factor  $\frac{(4\pi)^\epsilon}{\Gamma(1-\epsilon)}$ .

### 2.1.2 Unitary Cuts - A Numerical Approach

Evaluating the integrals in  $d$ -dimensions and then taking the limit  $d \rightarrow 4$  is useful when performing a loop calculation analytically. It is, however, not possible to directly implement this approach numerically because the calculations need to be done in an integer number of dimensions.

A general  $n$ -point scalar integral has the form

$$I^{(n)} = \int \frac{d^d k}{(2\pi)^d} \frac{1}{[k^2 - m_0^2][(k + q_1)^2 - m_1^2] \cdots [(k + q_n)^2 - m_n^2]} \quad (2.5)$$

where  $m_i$  are the masses of the particles in the loop and the momenta  $q_i$  are determined as shown in fig 2.1. Only being a function of the  $q_i$ 's and  $m_i$ 's makes a scalar loop integral a standard function which needs to be calculated once.

It can be shown that, in 4-dimensions, *any*  $n$ -point loop integral (i.e. one with  $n$  external legs) can be reduced to a sum of scalar integrals which are 4-point or less. Thus a general  $n$ -point loop integral can be written as

$$I = \sum_i C_i^{(4)} I_i^{(4)} + \sum_j C_j^{(3)} I_j^{(3)} + \sum_l C_l^{(2)} I_l^{(2)} + \sum_m C_m^{(1)} I_m^{(1)} \quad (2.6)$$

where  $C_i^{(n)}$  is the  $i$ -th coefficient for the scalar  $n$ -point integral and the sum over  $i$  includes all permutations of the original denominators in the scalar integrals.

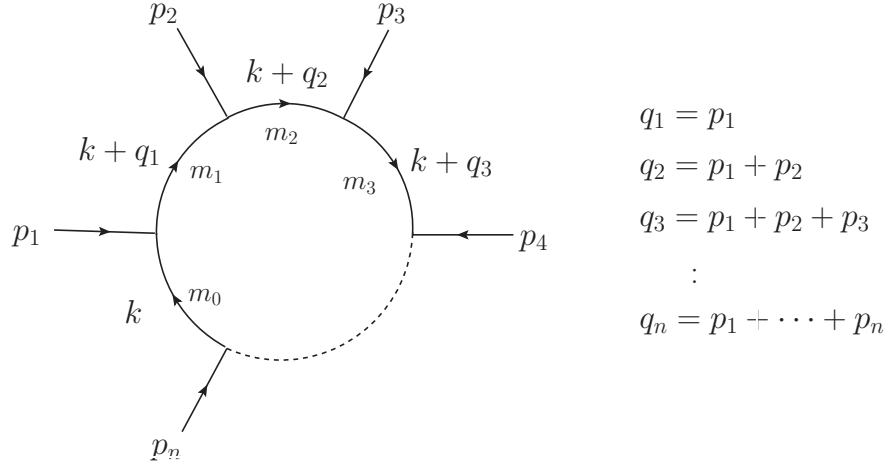


**Figure 2.1:** A general  $n$ -point loop diagram illustrating the momenta flow around the loop.

Once the coefficients  $C_i^{(n)}$  have been determined the results of the  $d$ -dimensional scalar loop integrals can be looked up and the regularised result of the original integral can then be determined.

A common technique for reducing loop calculations to a sum of scalar integrals is Passarino-Veltman reduction [17], however this requires algebraic manipulation of the original loop integral and so is not suitable for a numerical approach. Also, for a large number of external particles this technique generates a large number of terms and would therefore become impractical. In recent years work has been done using the technique of unitary cuts [18, 19] which allows the reduction of loop integrals to be performed numerically. The idea behind the unitary cut technique is quite straightforward and is implemented by putting various combinations of the loop propagators on-shell (the so-called unitary cuts). The complexity of the unitary cut technique becomes apparent when one tries to find suitable parametrisation of the momenta so that the various combinations of cuts can be performed.

## A Simple 2-Dimensional Example

To illustrate the technique a simple 2-dimensional example will be considered. This has the advantage of simplifying the algebra while still illustrating the key concepts.

Consider the following bubble loop in 2-dimensions with external moment  $p$

and loop particles with masses  $m_1$  and  $m_2$ .

$$I = \int \frac{d^2k}{(2\pi)^2} \frac{4(k \cdot p)^2}{[k^2 - m_1^2][(k+p)^2 - m_2^2]} \quad (2.7)$$

In 2-dimensions any loop integral can be reduced to a sum of scalar 2-point integrals and lower, therefore the numerator  $\mathcal{N}(k, p) = 4(k \cdot p)^2$  can be written in the form

$$\mathcal{N}(k, p) = [(k+p)^2 - m_2^2]A_1 + [k^2 - m_1^2]A_2 + B \quad (2.8)$$

resulting in two scalar tadpole loops with coefficients  $A_1$  and  $A_2$  and one scalar bubble loop with coefficient  $B$ . The coefficients  $A_1$ ,  $A_2$  and  $B$  are independent of  $k$  and only depend on  $p$ ,  $m_1$  and  $m_2$ .

It should be mentioned that, in general, the numerator may not be as simple as shown in eq.(2.7) because a general 2-dimensional bubble integral may have been obtained from some higher dimensional loop integral. This would be achieved by “pinching” the  $n$ -point graph in all possible ways to obtain all possible bubble graphs. For example, pinching the  $n$ -point graph as shown in figure 2.2 gives a bubble integral

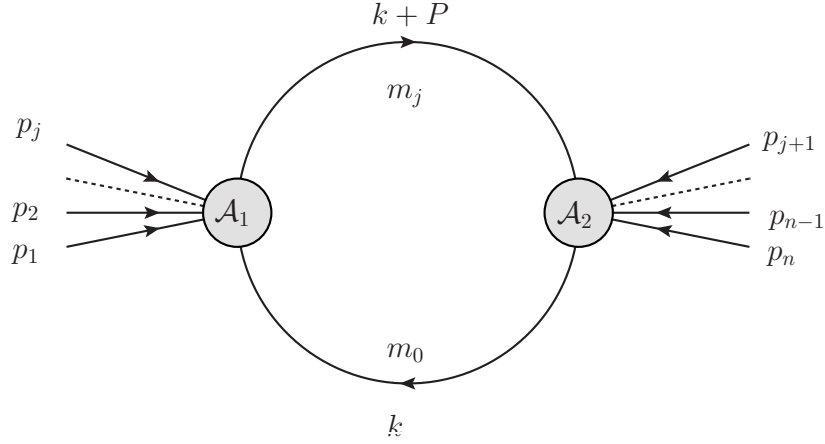


**Figure 2.2:** A general  $n$ -point integral can be “pinched” to give an effective 2-point topology where  $P = p_1 + \dots + p_j$ . By performing the pinch the effective vertices  $\mathcal{A}_1$  and  $\mathcal{A}_2$  will now contain propagator denominators.

of the form

$$I = \int \frac{d^2k}{(2\pi)^2} \frac{\mathcal{A}_1 \mathcal{A}_2}{[k^2 - m_0^2][(k+P)^2 - m_j^2]} \quad (2.9)$$

When the numerator from this is put in the similar form as eq.(2.8) the coefficients  $A_1$ ,

$A_2$  and  $B$  will now be more complicated, containing both propagator denominators and a dependency on the loop momenta  $k$ . These coefficients, however, will be finite for the selected loop momenta used in performing the unitary cuts.

Returning to the simple example of eq.(2.7), the determination of the coefficient  $B$  requires both of the propagators to be cut (i.e. put on-shell) which has the effect of projecting out the two tadpole coefficients i.e.

$$B = \mathcal{N}(k, p) \Big|_{k^2=m_1^2; (k+p)^2=m_2^2} \quad (2.10)$$

In a similar way the tadpole coefficients can be determined by cutting each of the propagators in turn. Using eq.(2.10) this gives

$$A_1 = \frac{\mathcal{N}(p, k) - B}{(k+p)^2 - m_2^2} \Big|_{k^2=m_1^2} \quad (2.11)$$

$$A_2 = \frac{\mathcal{N}(p, k) - B}{k^2 - m_1^2} \Big|_{(k+p)^2=m_2^2} \quad (2.12)$$

Cutting the propagators requires a suitable choice of parametrisation of  $k$  and in 2-dimensions this is best done using light-cone coordinates i.e.

$$p = (p_+, p_-) \quad (2.13)$$

$$k = (\alpha p_+, \beta p_-) \quad (2.14)$$

where  $\alpha$  and  $\beta$  are the parameters to be determined for the various cuts. In light-cone coordinates

$$p^2 = 2p_+p_- \quad (2.15)$$

$$k^2 = 2\alpha\beta p_+p_- = \alpha\beta p^2 \quad (2.16)$$

$$k.p = (\alpha + \beta)p_+p_- = \frac{(\alpha + \beta)}{2}p^2 \quad (2.17)$$

Cutting both propagators requires the following conditions to be satisfied

$$k^2 = m_1^2 \quad \Rightarrow \quad \alpha\beta = \frac{m_1^2}{p^2} \quad (2.18)$$

$$(k+p)^2 = m_2^2 \quad \Rightarrow \quad \alpha + \beta = \frac{m_2^2 - p^2 - m_1^2}{p^2} \quad (2.19)$$

This fixes both  $\alpha$  and  $\beta$ , leading to the following solutions

$$\alpha \equiv \alpha_0 = \frac{1}{2p^2} \left[ m_2^2 - p^2 - m_1^2 \pm \sqrt{\lambda(p^2, m_1^2, m_2^2)} \right] \quad (2.20)$$

$$\beta \equiv \beta_0 = \frac{1}{2p^2} \left[ m_2^2 - p^2 - m_1^2 \mp \sqrt{\lambda(p^2, m_1^2, m_2^2)} \right] \quad (2.21)$$

where  $\lambda(x, y, z) = x^2 + y^2 + z^2 - 2xy - 2xz - 2yz$ . With this choice of parametrisation these solutions are applicable to any 2-dimensional bubble loop where both propagators have been cut. This gives the general solution for  $B$  as

$$\begin{aligned} B &= \mathcal{N}(k, p)|_{k^2=m_1^2; (k+p)^2=m_2^2} \\ &= \mathcal{N}(\alpha_0, \beta_0) \end{aligned} \quad (2.22)$$

For our particular example with  $\mathcal{N}(p, k) = 4(k \cdot p)^2 \equiv (\alpha + \beta)^2 p^4$  the coefficient  $B$  is

$$\begin{aligned} B &= (\alpha_0 + \beta_0)^2 p^4 \\ &= (m_2^2 - p^2 - m_1^2)^2 \end{aligned} \quad (2.23)$$

For the tadpole coefficient  $A_1$  only one of the propagators needs to be cut, in which case the only condition that holds is eq.(2.20). This fixes  $\alpha$  only, giving

$$\alpha \equiv \alpha_0(\beta) = \frac{1}{\beta} \frac{m_1^2}{p^2} \quad (2.24)$$

Using eq.(2.11) and the fact that

$$\begin{aligned} (k+p)^2 - m_2^2|_{k^2=m_1^2} &= k^2 + p^2 + 2k \cdot p - m_2^2|_{k^2=m_1^2} \\ &= p^2 [(\alpha_0(\beta) + \beta) - (\alpha_0 + \beta_0)] \end{aligned} \quad (2.25)$$

the general solution for  $A_1$  is

$$\begin{aligned} A_1 &= \frac{\mathcal{N}(p, k) - B}{(k + p)^2 - m_2^2} \Big|_{k^2=m_1^2} \\ &= \frac{1}{p^2} \frac{\mathcal{N}(\alpha_0(\beta), \beta) - \mathcal{N}(\alpha_0, \beta_0)}{(\alpha_0(\beta) + \beta) - (\alpha_0 + \beta_0)} \end{aligned} \quad (2.26)$$

For a renormalisable theory the numerator  $\mathcal{N}$  is at most quadratic in  $\beta$  therefore the most general form of eq.(2.26) is

$$\frac{1}{p^2} \frac{\mathcal{N}(\alpha_0(\beta), \beta) - \mathcal{N}(\alpha_0, \beta_0)}{(\alpha_0(\beta) + \beta) - (\alpha_0 + \beta_0)} = C_0 + C_1 \alpha_0(\beta) + C_2 \beta \quad (2.27)$$

By selecting three different values of  $\beta$  eq.(2.27) can be thought of as a set of linear equations which can easily be solved using a computer. Thus once a suitable parametrisation of the loop momenta has been determined any tadpole coefficient can be determined numerically. The last two terms on the r.h.s. of eq.(2.27) are effectively linear in the integration variable  $k$  and will give zero after integration, therefore we end up with the general result

$$A_1 = C_0 \quad (2.28)$$

Using eq.(2.26) our example gives<sup>1</sup>

$$\begin{aligned} A_1 &= p^2 \frac{(\alpha_0(\beta) + \beta)^2 - (\alpha_0 - \beta_0)^2}{(\alpha_0(\beta) + \beta) - (\alpha_0 + \beta_0)} \\ &= p^2 [(\alpha_0(\beta) + \beta) + (\alpha_0 + \beta_0)] \end{aligned} \quad (2.29)$$

and comparing this with the r.h.s. of eq.(2.27) we see  $C_0 = p^2(\alpha_0 + \beta_0)$  and so

$$\begin{aligned} A_1 &= p^2(\alpha_0 + \beta_0) \\ &= m_2^2 - p^2 - m_1^2 \end{aligned} \quad (2.30)$$

The simplest way to evaluate the tadpole coefficient  $A_2$  is to bring the tadpole integral

---

<sup>1</sup>The simple example of  $\mathcal{N} = 4(k \cdot p)^2$  is most easily solved directly to find  $C_0$ , however in general this could be done by solving a set of linear equations as described above.

into a standard form by shifting the integration variable  $k \rightarrow k - p$ . This gives

$$A_2 = \left. \frac{\mathcal{N}(p, k - p) - B}{(k - p)^2 - m_1^2} \right|_{k^2 = m_2^2} \quad (2.31)$$

With this shift the on-shell conditions become

$$k^2 = m_2^2 \quad \Rightarrow \quad \alpha\beta = \frac{m_2^2}{p^2} \quad (2.32)$$

$$(k - p)^2 = m_1^2 \quad \Rightarrow \quad \alpha + \beta = -\frac{m_1^2 - p^2 - m_2^2}{p^2} \quad (2.33)$$

and following the same procedure as before, our example with  $\mathcal{N}(p, k - p) = 4(k \cdot p - p^2)^2$  results in

$$A_2 = -\frac{m_1^2 - p^2 - m_2^2}{p^2} \quad (2.34)$$

Combining the coefficients  $A_1, A_2$  and  $B$  gives the final reduced integral as<sup>2</sup>

$$\begin{aligned} \int \frac{d^2k}{(2\pi)^2} \frac{4(k \cdot p)^2}{[k^2 - m_1^2][(k + p)^2 - m_2^2]} = \\ (p^2 + m_1^2 - m_2^2)^2 \int \frac{d^2k}{(2\pi)^2} \frac{1}{[k^2 - m_1^2][(k + p)^2 - m_2^2]} \\ + (m_2^2 - p^2 - m_1^2) \int \frac{d^2k}{(2\pi)^2} \frac{1}{k^2 - m_1^2} \\ + (m_1^2 + 3p^2 - m_2^2) \int \frac{d^2k}{(2\pi)^2} \frac{1}{(k + p)^2 - m_2^2} \end{aligned} \quad (2.35)$$

It should be noted that, in general, there is one complication - the result of the unitary cut should be consistent with dimensional regularisation. For loop integrals which are ultraviolet divergent it is necessary to account for the rational part, which arises when the dimensionality of the loop integral is altered. This is mentioned for completeness, but does not need to be considered for the above example.

### 2.1.3 SAMURAI - A Unitary Cut Tool

The discussion in the previous section illustrates how, with a suitable choice of parametrisation of the loop momenta, a general 2-dimensional  $n$ -loop integral can

---

<sup>2</sup>As a check this integral could also be reduced using Passarino-Veltman reduction which would give the same result as calculated using the unitary cut technique.

be reduced to a sum of scalar bubble and tadpole integrals. For 4-dimensional integrals, the principal is exactly the same, but in practice (and as detailed in [18] and [19]) doing this is rather complicated. The reason for this being the need to calculate the coefficients for scalar box and triangle integrals as well as the bubbles and tadpoles. This makes the algebra more involved and it is preferable to find an existing tool which automates the unitary cut technique in 4-dimensions.

There are several such tools available including CutTools [20], Golem [21] and SAMURAI [22]. For this project the tool of choice is SAMURAI and the main reasons for this choice are that it

- has the versatility to deal with one-loop Feynman integrals in both massless and massive theories.
- automatically calculates the full rational term according to the  $d$ -dimensional approach.

SAMURAI is implemented as a FORTRAN 90 library with the option to use either the OneLOop [23] or QCDDLoop [24] libraries to evaluate the  $d$ -dimensional scalar integrals. Both of these libraries contain the standard scalar box, triangle, bubble and tadpole integrals - which are the only ones needed in 4-dimensions. After comparing the two scalar loop libraries it was decided that QCDDLoop would be the better choice as it produces more stable results and also has the advantage that the extra-dimensional mass scale  $\mu^2$  can be varied without the need to reinitialise SAMURAI.

The process of calculating a one-loop integral in SAMURAI is simple to implement and is detailed in [22], but the key components are:

1. Calculating the numerator for the loop integral in terms of the SAMURAI loop momentum variable  $k$ , with the important substitution that  $k^2 \rightarrow k^2 - \mu^2$ . This is required for  $d$ -dimensional consistency.
2. Getting each of the  $n$  denominators into the form  $[(k - q_i)^2 - m_i^2]$  so that the momenta  $q_i$  and masses  $m_i^2$  can be extracted and passed to SAMURAI.

The output from SAMURAI has a similar form to eq.(2.4) and is given as a complex-valued array comprised of three components, a double pole, a single pole and a finite



part.

## 2.2 Bremsstrahlung Calculations

Having found a suitable approach to numerically calculate divergent  $d$ -dimensional loop integrals we also need to find a numerical approach to evaluate the divergent bremsstrahlung calculations.

The usual way of dealing with divergent bremsstrahlung calculations is to perform the phase-space integral with the kinematics of the radiated bremsstrahlung particle evaluated in  $d$ -dimensions. In a similar approach to the loop calculations, this process regularises the infrared singularities<sup>3</sup> which can then be cancelled off against the corresponding singularities from the loop corrections.

This cancellation is due to the Kinoshita-Lee-Nauenberg (KLN) theorem [25, 26] which states that when *all* initial and final state bremsstrahlung processes are combined with the loop corrections the perturbative calculation will be infrared finite. However, since we are calculating a scattering process - which involves only two initial state particles - it is not possible to include all possible initial radiation states. In this situation the KLN theorem does not apply and there are some remaining divergences associated with radiation from the initial-state particles.

To deal with this situation, these remaining divergences - contained within the Altarelli-Parisi splitting functions [27] - are absorbed into the parton distribution functions (PDFs). Up to a factorisation scale  $\mu_F$  the divergences in the splitting functions cancel the corresponding divergences in the PDFs, making the PDFs infrared finite. The remaining finite portion of the splitting function - above the scale  $\mu_F$  - are then included with the NLO calculations.

As discussed previously, dealing with  $d$ -dimensional integrals is not suitable for numerical implementation as it requires the phase-space integration to be done analytically i.e. in a non-integer number of dimensions. Fortunately there are two

---

<sup>3</sup>In this context infrared singularities encompass both soft and collinear singularities. Soft singularities result when the momenta of the radiated particle approaches zero and collinear singularities occur when the momenta of the radiated particle runs parallel to another massless particle.

different approaches whereby the infrared divergences can be regularised while performing the integrations numerically, these are the method of phase-space slicing [28] and the dipole subtraction method [29].<sup>4</sup> Since the dipole method is the approach we will be using for this project we will describe this further in the next section.

### 2.2.1 The Dipole Subtraction Method

Using a similar notation to [29] the standard procedure for calculating the cross-section  $\sigma$  for a  $2 \rightarrow n$  scattering process at NLO involves a sum of phase-space integrals

$$\sigma = \underbrace{\int_n d\sigma^{\text{tree}}}_{\text{LO}} + \underbrace{\int_n d\sigma^{1\text{-loop}} + \int_{n+1} d\sigma^{\text{brem}}}_{\text{NLO}} \quad (2.36)$$

where  $d\sigma^{\text{tree}}$ ,  $d\sigma^{1\text{-loop}}$  and  $d\sigma^{\text{brem}}$  represent the tree-level, 1-loop and bremsstrahlung differential cross-sections respectively and  $\int_m$  represents the phase-space integral over an  $m$ -body final state.

As previously discussed, the two NLO terms in eq.(2.36) are both infrared divergent, however their sum - when carried out in consistent regularisation schemes - will give an infrared finite result. With the 1-loop corrections calculated with SAMURAI the first two terms in eq.(2.36) can be integrated numerically, however the bremsstrahlung term needs to be integrated analytically in  $d$ -dimensions so that the infrared divergences can be regularised in a consistent way with SAMURAI.

By introducing an auxiliary cross-section  $d\sigma^{\text{A}}$ , which has the same divergent structure as  $d\sigma^{\text{brem}}$ , the dipole subtraction method allows all of the phase-space integrals to be evaluated numerically (i.e. in 4-dimensions). Using this method the NLO contribution to the cross-section can be rewritten as

$$\sigma^{\text{NLO}} = \int_n \left[ d\sigma^{1\text{-loop}} + \int_1 d\sigma^{\text{A}} \right]_{d=4} + \int_{n+1} \left[ d\sigma^{\text{brem}} - d\sigma^{\text{A}} \right]_{d=4} \quad (2.37)$$

where both integrals are now finite in 4-dimensions.

The dipole subtraction method makes use of the fact that the infrared diver-

---

<sup>4</sup>For a comparison between these two methods see for example [30]

gences can be factored out into terms known as dipoles. This is possible because, for a given bremsstrahlung process, when the radiated particle becomes soft or collinear then the propagator connecting to the rest of the diagram goes on-shell. This allows the divergent part to effectively be factored out into the dipole terms - separate from the rest of the process.

In practice each of the dipoles are determined for a pair of particles, which are known as the emitter and spectator. By combining the dipole terms  $dV_{\text{dipole}}$  with the tree-level cross section <sup>5</sup> and summing over all dipoles (i.e. all combinations of emitter and spectator particles) the auxiliary cross-section  $d\sigma^A$  is created. This can be written schematically as

$$d\sigma^A = \sum_{\text{dipoles}} d\sigma^{\text{tree}} \otimes dV_{\text{dipole}} \quad (2.38)$$

This construction has the same singular structure as  $d\sigma^{\text{brem}}$  and since the singular nature of the process is factorised into  $dV_{\text{dipole}}$  it is possible to integrate out the momenta of the radiated bremsstrahlung particle separately from the rest of the process. This integral can be done analytically in  $d$ -dimensions allowing the infrared divergences in the dipole terms to be regularised. So from eq.(2.38) we get

$$\begin{aligned} \int_{n+1} d\sigma^A &= \sum_{\text{dipoles}} \int_n d\sigma^{\text{tree}} \otimes \int_1 dV_{\text{dipole}} \\ &= \int_n [d\sigma^{\text{tree}} \otimes I] \end{aligned} \quad (2.39)$$

where

$$I = \sum_{\text{dipoles}} \int_1 dV_{\text{dipole}} \quad (2.40)$$

This will contain a double pole, a single pole and a finite part.

The dipole method provides all of the dipole terms  $dV_{\text{dipole}}$  so that the auxiliary cross-section  $d\sigma^A$  for a specific bremsstrahlung process can be calculated. It also provides the insertion terms  $I$  so that the infrared poles can be cancelled with the

---

<sup>5</sup>The precise details on how the dipole and tree-level cross-section are combined requires (amongst other things) a suitable parametrisation and scaling of the momenta used in  $d\sigma^{\text{tree}}$ . Further details of this procedure are given in [29]

poles arising from the 1-loop calculations.

Schematically the dipole method is implemented as

$$\begin{aligned} \sigma^{\text{NLO}} = & \int_n \left[ d\sigma^{\text{1-loop}} + d\sigma^{\text{tree}} \otimes I \right]_{d=4} \\ & + \int_{n+1} \left[ d\sigma^{\text{brem}} - \left( \sum_{\text{dipoles}} d\sigma^{\text{tree}} \otimes dV_{\text{dipole}} \right) \right]_{d=4} \end{aligned} \quad (2.41)$$

The second term in eq.(2.41) is infrared finite in 4-dimensions because the subtraction term  $\sum_{\text{dipoles}} d\sigma^{\text{tree}} \otimes dV_{\text{dipole}}$  cancels the divergences in  $d\sigma^{\text{brem}}$ . The subtraction term is then reinserted as  $d\sigma^{\text{tree}} \otimes I$  and the pole parts of this expression cancel the infrared poles from  $d\sigma^{\text{1-loop}}$  making the first term in eq.(2.41) finite in 4-dimensions as well.

For completeness it should be mentioned that, in general, eq.(2.41) includes an extra term. The form of eq.(2.41) holds when there are no initial-state singularities, but (as already discussed) the uncanceled initial state singularities - which are dealt with in the PDFs - introduce Altarelli-Parisi splitting functions to the NLO calculations. When including initial state singularities the extra term which needs to be added has the form

$$\int_0^1 dx \int_n d\sigma^{\text{tree}}(xp) \otimes (P + K)(x) \quad (2.42)$$

where there is an extra integration over  $x$  and  $d\sigma^{\text{tree}}(xp)$  represents that the incoming momenta  $p$  for the tree-level cross-section is scaled by  $x$ . The  $P(x)$  and  $K(x)$  terms are the Altarelli-Parisi splitting functions and other functions which are described in [29].

## 2.3 Set-Up for Performing the Perturbative Calculations

To make a comparison with the experimental data from the LHC the perturbative calculations in this thesis need to be set-up accordingly.

Since the LHC is a proton-proton particle collider the parton-level calculations need to be folded with suitable parton distribution functions (PDFs). For this thesis two different PDF sets will be used: CTEQ6M and CTEQ6L [31,32]. The CTEQ6M

PDF set is calculated in the  $\overline{MS}$ -scheme whereas CTEQ6L is calculated at leading order. Further details of the PDF folding process are given in section 3.2.7.

The energy choice used for these calculations will be  $\sqrt{s} = 14 \text{ TeV}$  (i.e. the maximum beam energy of the LHC). The renormalisation and factorisation scales  $\mu$  and  $\mu_F$  will be set to  $\mu = \mu_F = \sqrt{\hat{s}}$ . Where  $\hat{s} = x_1 x_2 s$  and  $x_1$  and  $x_2$  are defined in section 3.2.7 - see eq.(3.43).

As already mentioned the focus of our study will be on the  $R_2$  scalar and  $U_1$  vector LQ. In both of these cases we will use the same value for the LQ mass  $m_{\text{LQ}} = 750 \text{ GeV}$  - consistent with the limits in [6]. In addition to this all of the couplings will be based on the value of  $\alpha_s$  evaluated at  $m_{\text{LQ}}$  i.e.  $\underbrace{h_{1L} = h_{1R}}_{U_1 \text{ couplings}} = \underbrace{h_{2L} = h_{2R}}_{R_2 \text{ couplings}} = 1.07$ .

## Chapter 3

# Scalar Leptoquarks

With regards to calculating NLO corrections, scalar particles are easier to deal with than vector particles. In particular there is no need to consider contributions from Goldstone bosons or Faddeev-Popov ghosts. Being the simpler case it therefore makes sense to consider a scalar LQ process as our starting point.

For the purpose of this chapter we will be looking at the scalar LQ type  $R_2$  as described in [7], this type of LQ forms an  $SU(2)$  doublet with electric charges  $+5/3$  and  $+2/3$ . Initially we will only consider the factorisable process where a  $+5/3$  LQ is produced, and subsequently decays, via the process  $u + g \rightarrow e^- + R_2 \rightarrow e^- + e^+ + u$  (see figure 3.1).

The naming convention being used for the momenta is as follows: the incoming up-quark and gluon have momenta  $p_1$  and  $p_2$  respectively and the outgoing electron, positron and up-quark have momenta  $q_1$ ,  $q_2$  and  $q_3$  respectively. To distinguish between a quark and a lepton in the Feynman diagrams, a fermion line representing a lepton will be double lined. It should be noted that, in the high energy limit, the masses of the first generation quarks and leptons can be assumed to be zero.

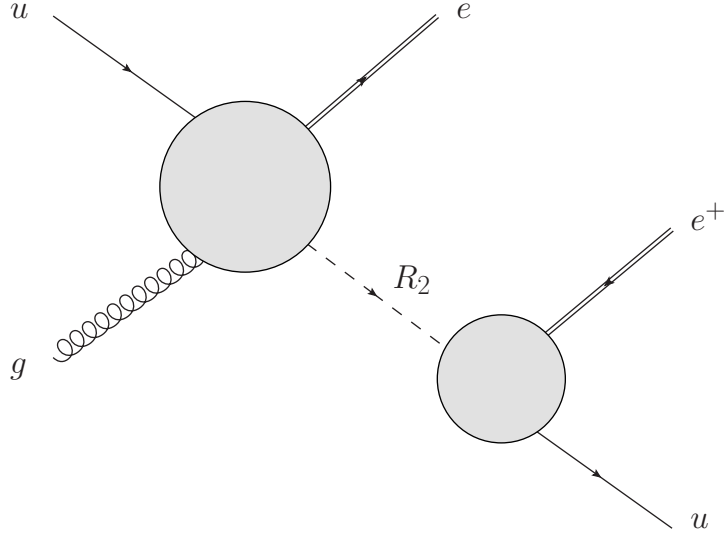


**Figure 3.1:** The factorisable contribution to  $u + g \rightarrow e^- + e^+ + u$  with the production of an intermediate scalar LQ. This process will be useful for calculating NLO corrections in the NWA.

### 3.1 Helicity Projections

Even though scalar LQs present an easier starting point than vector LQs, there is one complication that needs to be dealt with. Since the production and decay of the LQ involves fermions there is the complication of handling spinors and  $\gamma$ -matrices. To make the numerical calculations easier to implement in FORTRAN the spinors and  $\gamma$ -matrices need to be traced out. When squaring amplitudes the tracing out of  $\gamma$ -matrices happens automatically, however our numerical results need to be calculated at the amplitude level. In this situation the tracing can be achieved by doing helicity projections for the incoming and outgoing fermions.

It can be shown (see appendix A) that for scalar LQs, which always involve an even number of  $\gamma$ -matrices, the amplitude for LQ production  $\mathcal{A}_{\text{prod}}$  is given by

$$e^{i\eta} \mathcal{A}_{\text{prod}}(\lambda_1) = \frac{1}{\sqrt{2} p_1 \cdot q_1} \text{Tr} \left[ \not{q}_1 \left( \frac{1 - \lambda_1 \gamma^5}{2} \right) \Gamma_{\text{even}} \not{p}_1 \right] \quad (3.1)$$

where  $\Gamma_{\text{even}}$  is a string of an even number of  $\gamma$ -matrices,  $\lambda_1$  is the helicity of the outgoing electron and  $\eta$  is an arbitrary phase which is introduced as part of doing the helicity projection. Since all production amplitudes will have the same phase factor it can safely be ignored.

Likewise the amplitude for LQ decay  $\mathcal{A}_{\text{decay}}$  is given by

$$e^{i\eta'} \mathcal{A}_{\text{decay}}(\lambda_2) = \frac{1}{\sqrt{2} q_2 \cdot q_3} \text{Tr} \left[ q \not{\beta} \left( \frac{1 - \lambda_2 \gamma^5}{2} \right) \Gamma_{\text{even}} q \not{\beta} \right] \quad (3.2)$$

where  $\lambda_2$  is the helicity of the outgoing positron and  $\eta'$  is the arbitrary phase which is the same for all decay amplitudes so again it can be ignored.

## 3.2 Scalar Leptoquarks in the NWA

Within the NWA the only NLO corrections which need to be considered are those which have a factorisable topology as shown in 3.1. This has the advantage that the NLO corrections to the LQ production process and decay process can be treated separately as discussed in section 1.5.

### 3.2.1 Virtual Corrections to the Production Process

At leading-order the LQ production process is made up of two topologies see (fig 3.2). The virtual corrections to this process are comprised of three types; QCD corrections,

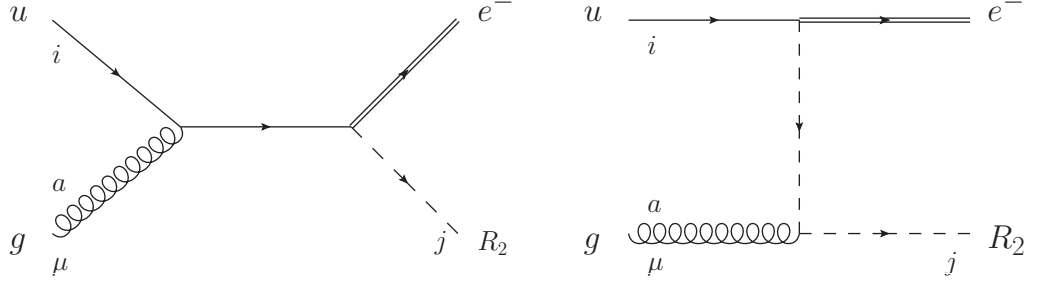


**Figure 3.2:** The leading-order contributions to  $u + g \rightarrow e^- + R_2$  where the  $u$ -quark has colour  $i$ , the LQ has colour  $j$  and the gluon has Lorentz index  $\mu$  and colour  $a$ .

electroweak corrections and LQ corrections. Each of these types can be grouped into three different loop topologies:

- bubble diagrams - consisting of loops with two vertices
- triangle diagrams - having three vertices
- and box diagrams - having four.



Figures 3.3 to 3.5 illustrate all of the virtual QCD corrections to the LQ production process. For completeness figure 3.3 consists of all valid bubble diagrams, however it should be noted that due to the colour algebra the contribution from diagram  $B_3$  is in fact zero.

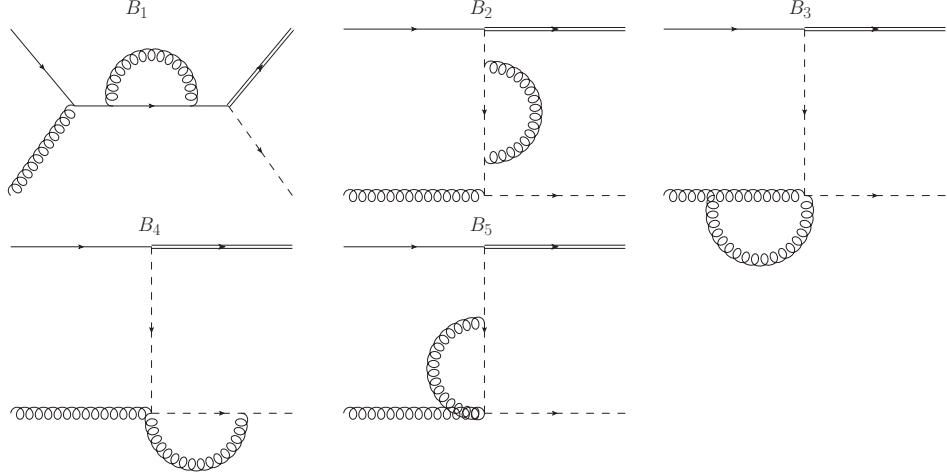


**Figure 3.3:** *QCD bubble graphs for LQ production.*

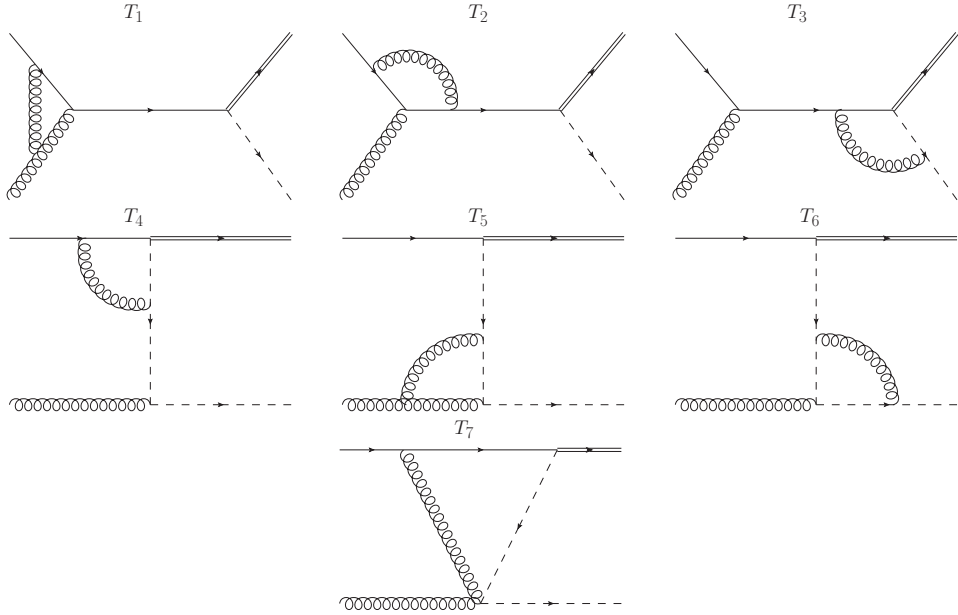


**Figure 3.4:** *QCD triangle graphs for LQ production.*

Figures 3.6 to 3.8 show the virtual electroweak corrections to the LQ production process. The Feynman diagrams for the electroweak corrections show the virtual gauge boson as a photon, however there are two further copies of these diagrams - one with the photon replaced by a Z-boson and another with the photon replaced by

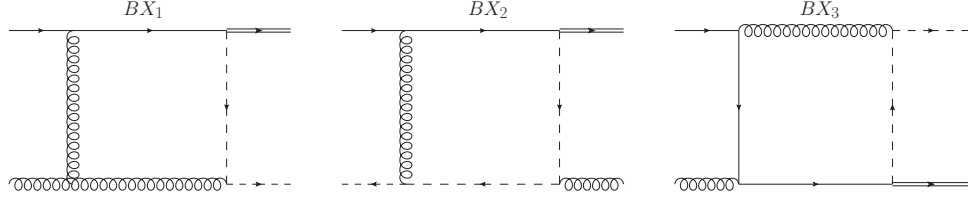


**Figure 3.5:** *QCD box graphs for LQ production.*

*Note: These graphs illustrate the different topologies, but do not show the in and out states in a consistent way.*

a W-boson. Being a charged gauge boson, however, there is no W-boson contribution to diagrams  $EWT_2$ ,  $EWT_5$  and  $EWBX_3$ .

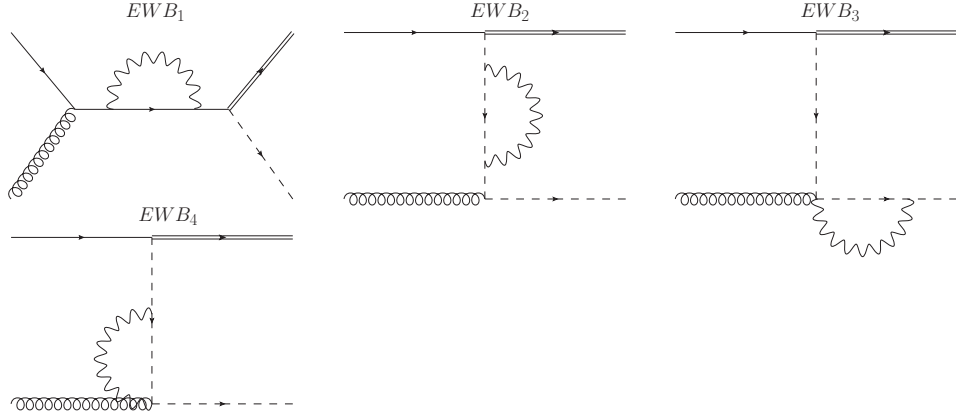


**Figure 3.6:** *Electroweak bubble graphs for LQ production.*

Finally, figures 3.9 and 3.10 show the virtual LQ corrections to the LQ production process.

### 3.2.2 Virtual Corrections to the Decay Process

At leading-order the LQ decay process is a single Feynman diagram (see fig 3.11). The virtual corrections to the decay process, figures 3.12 and 3.13, are comprised of QCD corrections and electroweak corrections and consist only of triangle diagrams. As with the electroweak production graphs there are also three versions of the electroweak decay graphs - containing either a virtual photon, Z or W-boson. Due to charge conservation there is no W-boson contribution to  $EWT_{13}$ .

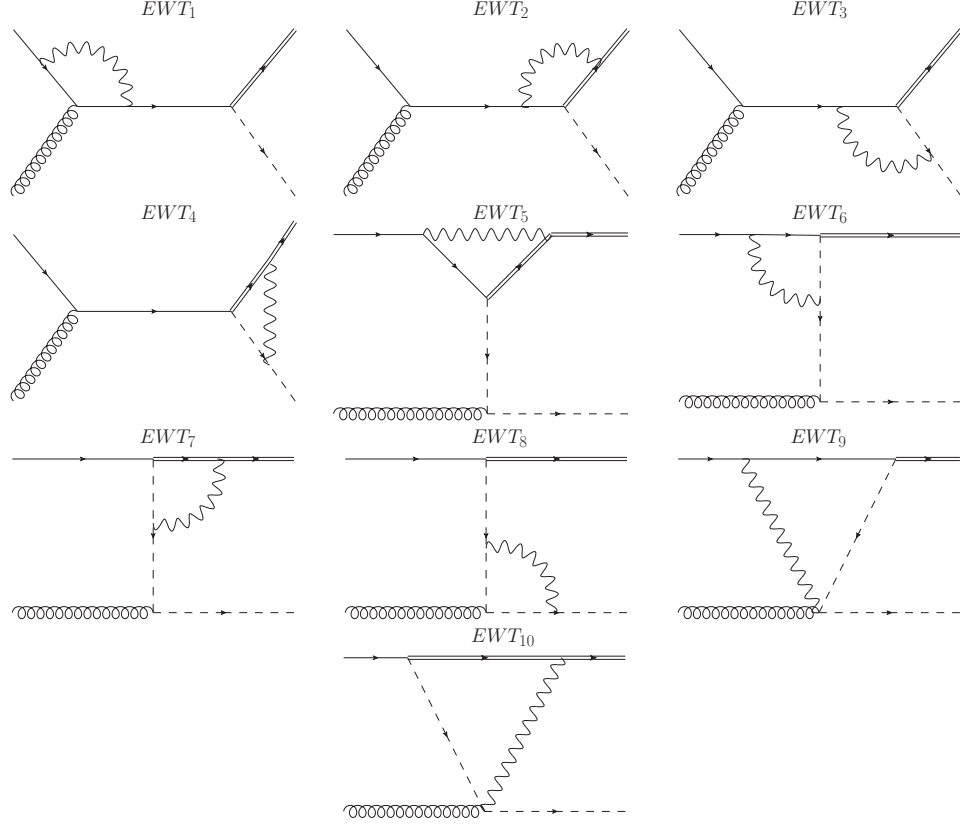


**Figure 3.7:** Electroweak triangle graphs for  $LQ$  production.

### 3.2.3 External Leg Corrections

The virtual corrections described in the previous section are considered to be internal corrections, however the loop corrections for the external legs still need to be determined.

From the LSZ reduction formula [33] the relationship between an S-matrix and the Feynman diagrams takes the form <sup>1</sup>

$$\langle q_1 \cdots q_m | S | p_1 \cdots p_n \rangle = \sqrt{Z_{p_1}} \cdots \sqrt{Z_{q_m}} \text{ (shaded diagram) } \quad (3.3)$$

where the shaded diagram on the right of eq.(3.3) represents the amputated tree-level

<sup>1</sup>This is based on the description of the LSZ reduction formula given in [34]

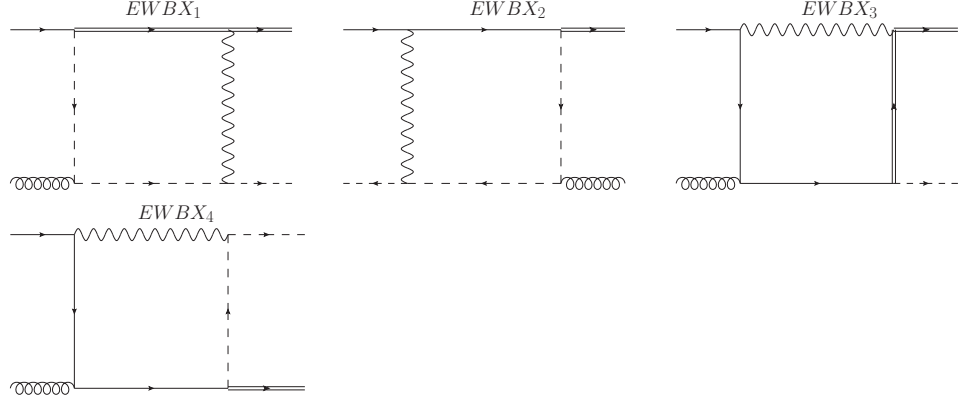


**Figure 3.8:** Electroweak box graphs for  $LQ$  production.  
*Note: These graphs illustrate the different topologies, but do not show the in and out states in a consistent way.*

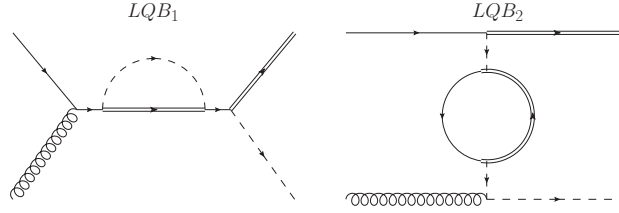


**Figure 3.9:** Leptoquark bubble graphs for  $LQ$  production.

Feynman diagrams i.e. those without external leg corrections.

The  $Z_i$  functions represent the wavefunction renormalisation factors for each incoming and outgoing particle <sup>2</sup> and account for the higher-order corrections to the external legs. By calculating the  $Z$ 's at 1-loop order the external leg corrections can therefore be determined.

### The u-quark

The wavefunction renormalisation factor for the massless u-quark  $Z_u$  can be calculated from

$$Z_u^{-1} = 1 - \left. \frac{d\Sigma}{d\not{p}} \right|_{\not{p}=0} \quad (3.4)$$

where  $-i\Sigma(\not{p})$  represents the 1-loop diagrams as shown in fig 3.14, each of which has the form given in eq.(B.2).

<sup>2</sup>For a decay process the number of incoming particles, labelled  $p_i$ , would be one and for a scattering process it would be two. The number of outgoing particles, labelled  $q_i$ , would typically be between two and four.

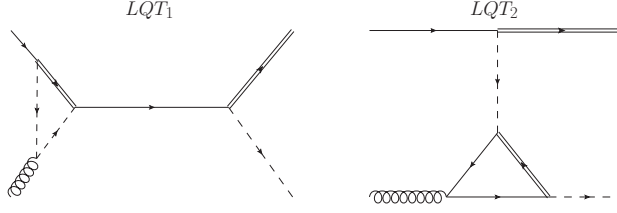


**Figure 3.10:** Leptoquark triangle graphs for LQ production.

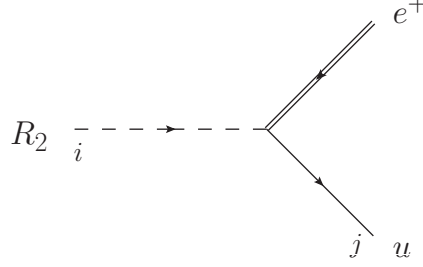


**Figure 3.11:** The leading-order contribution to  $R_2 \rightarrow e^+ + u$  where the LQ has colour  $i$  and the  $u$ -quark has colour  $j$ .

Since  $\left. \frac{d\Sigma}{d\hat{p}} \right|_{\hat{p}=0} \ll 1$  this means that

$$\sqrt{Z_u} \approx 1 + \frac{1}{2} \left. \frac{d\Sigma}{d\hat{p}} \right|_{\hat{p}=0} = 1 + \frac{1}{2} \delta Z_u \quad (\text{from eq.(B.5)}) \quad (3.5)$$

The  $\delta Z_u$  term is determined from the sum of the QCD, electroweak and LQ contributions and since the gluon and photon are massless the only contributions to  $\delta Z_u$  come from the W and Z-bosons and the LQ (see appendix B).

From the Feynman rules given in appendix C and using eq.(B.8) the final result for  $\sqrt{Z_u}$  is

$$\begin{aligned} \sqrt{Z_u} \approx 1 + \frac{1}{16\pi^2} \left[ g_W^2 \left( \frac{2}{\epsilon} - 2 \log \left( \frac{M_W^2}{\mu^2} \right) + 1 \right) + g_{Z(u)}^2 \left( \frac{2}{\epsilon} - 2 \log \left( \frac{M_Z^2}{\mu^2} \right) + 1 \right) \right. \\ \left. + g_{LQ}^2 \left( \frac{1}{\epsilon} - \log \left( \frac{M_{LQ}^2}{\mu^2} \right) + \frac{1}{2} \right) \right] \end{aligned} \quad (3.6)$$

where  $g_W$  and  $g_{LQ}$  are the respective couplings for the W-boson and LQ and  $g_{Z(u)}$  is the coupling of the Z-boson to the  $u$ -quark. In general these couplings are functions of the  $u$ -quark helicity and are defined in appendix C.

Details of the remaining external leg corrections can be found in appendix D.

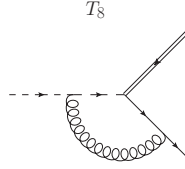


**Figure 3.12:** *QCD triangle graph for LQ decay.*

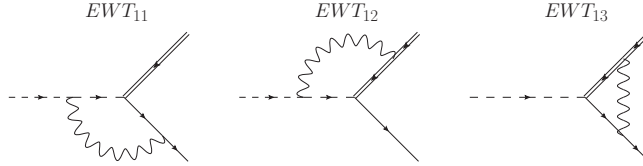


**Figure 3.13:** *Electroweak triangle graphs for LQ decay.*

### 3.2.4 Preparing the Virtual Corrections for SAMURAI

Having calculated the external leg corrections analytically the remaining virtual corrections need to be encoded in FORTRAN so that the loop integrals can be evaluated by SAMURAI. Using the Feynman rules (as given in appendix C) and the helicity projection technique each of the loop topologies can be written as a trace of  $\gamma$ -matrices. Most of these trace expressions contain a string of several  $\gamma$ -matrices and to perform these traces the symbolic manipulation language FORM [35] was used. This tool is ideally suited to performing traces of  $\gamma$ -matrices and has the added advantage that it can output its results directly in FORTRAN format. As discussed in section 2.1.3 SAMURAI evaluates the loop integrals in  $d = 4 - 2\epsilon$  dimensions in the limit that  $\epsilon \rightarrow 0$ , but it should be noted that with the exception of the loop momenta all other quantities, including the external momenta, are assumed to be 4-dimensional. This approach, known as dimensional reduction [36], means that the contractions of the  $\gamma$ -matrices can be done in 4-dimensions - which simplifies the loop expressions.

Using SAMURAI to perform the loop calculations does add one complication. All of the loops are evaluated in the  $\overline{MS}$ -scheme, however we require the LQ mass to be consistent with on-shell mass renormalisation. The only diagrams which are problematic are the ones with a bubble loop correction to an internal LQ. In the NWA these are the t-channel graphs  $B_2$ ,  $EWB_2$  and  $LQB_2$ .

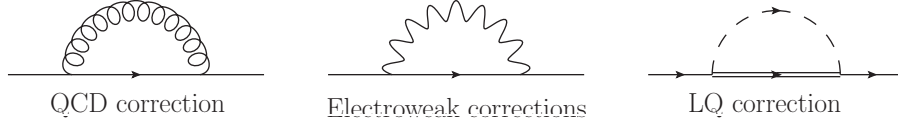


**Figure 3.14:** *External leg corrections to the u-quark*

Schematically the tree-level and 1-loop corrections can be written as

$$\begin{array}{c} \text{---} \rightarrow \text{---} \end{array} + \begin{array}{c} \text{---} \rightarrow \text{---} \\ | \\ \text{---} \text{---} \text{---} \end{array} \sim \frac{1}{t - m_{\text{LQ}}^2} + \frac{\Sigma(t)}{(t - m_{\text{LQ}}^2)(t - m_{\text{LQ}}^2)} \quad (3.7)$$

where  $\Sigma(t)$  represents the 1-loop bubble corrections to the LQ propagator evaluated at  $p^2 = t$ . Expanding  $\Sigma(t)$  as a Taylor series about  $m_{\text{LQ}}^2$

$$\Sigma(t) = \Sigma(m_{\text{LQ}}^2) + (t - m_{\text{LQ}}^2) \left. \frac{d\Sigma}{dt} \right|_{t=m_{\text{LQ}}^2} + \mathcal{O}(t - m_{\text{LQ}}^2)^2 \quad (3.8)$$

and subtracting the term

$$\frac{\Sigma(m_{\text{LQ}}^2)}{(t - m_{\text{LQ}}^2)(t - m_{\text{LQ}}^2)} \quad (3.9)$$

from eq.(3.7) we end up with

$$\begin{aligned} \frac{1}{t - m_{\text{LQ}}^2} + \frac{\Sigma(t)}{(t - m_{\text{LQ}}^2)(t - m_{\text{LQ}}^2)} &\rightarrow \frac{1 + \left. \frac{d\Sigma}{dt} \right|_{t=m_{\text{LQ}}^2}}{t - m_{\text{LQ}}^2} \\ &\sim \frac{Z_{\text{LQ}}}{t - m_{\text{LQ}}^2} \end{aligned} \quad (3.10)$$

which is consistent with on-shell mass renormalisation at this order of perturbation theory. In practice all that is required to make the LQ propagator loops consistent with on-shell mass renormalisation is to subtract the term

$$\frac{\Sigma(m_{\text{LQ}}^2)}{t - m_{\text{LQ}}^2} \times \mathcal{A}_{\text{tree (t-channel)}} \quad (3.11)$$

from the 1-loop LQ production results calculated in SAMURAI, where  $\mathcal{A}_{\text{tree (t-channel)}}$  is the t-channel contribution to the tree-level production amplitude.

### 3.2.5 Bremsstrahlung Corrections to the Production Process

To deal with the infrared singularities encountered in the bremsstrahlung corrections to the LQ production process the dipole subtraction method will be used. The first step in implementing the dipole subtraction method is to identify all pairs of emitters and spectators, of which there are four types of combinations

- Final-state emitter and final-state spectator
- Final-state emitter and initial-state spectator
- Initial-state emitter and final-state spectator
- Initial-state emitter and initial-state spectator

When considering QCD bremsstrahlung corrections (see figure 3.15) there is no gluon emission from the outgoing lepton and so there is no final-state emitter or spectator corresponding to this leg. In comparison, for the QED bremsstrahlung corrections (see figure 3.16) there is no photon emission from the incoming gluon leg and so no corresponding initial-state emitter or spectator.

### QCD corrections

*Note: In the following expressions for the dipole insertions any terms not explicitly defined can be found in [29]*

To illustrate the dipole subtraction method a particular choice of emitter and spectator will be used as an example. Consider the case where the quark is the incoming emitter and the leptoquark is the outgoing spectator - as illustrated in 3.17.

Referring to the relevant section of [29] the dipole subtraction term  $\mathcal{D}_j^{ai}$  for this is

$$\mathcal{D}_j^{ai}(q_1, q_{23}, k; p_1, p_2) = -\frac{1}{2} \frac{1}{p_1 \cdot k} \frac{1}{x_{ij,a}} \langle q_1, \tilde{q}_{23}; \tilde{p}_1, p_2 | \frac{\mathbf{T}_j \cdot \mathbf{T}_{ai}}{\mathbf{T}_{ai}^2} \mathbf{V}_j^{ai} | q_1, \tilde{q}_{23}; \tilde{p}_1, p_2 \rangle \quad (3.12)$$



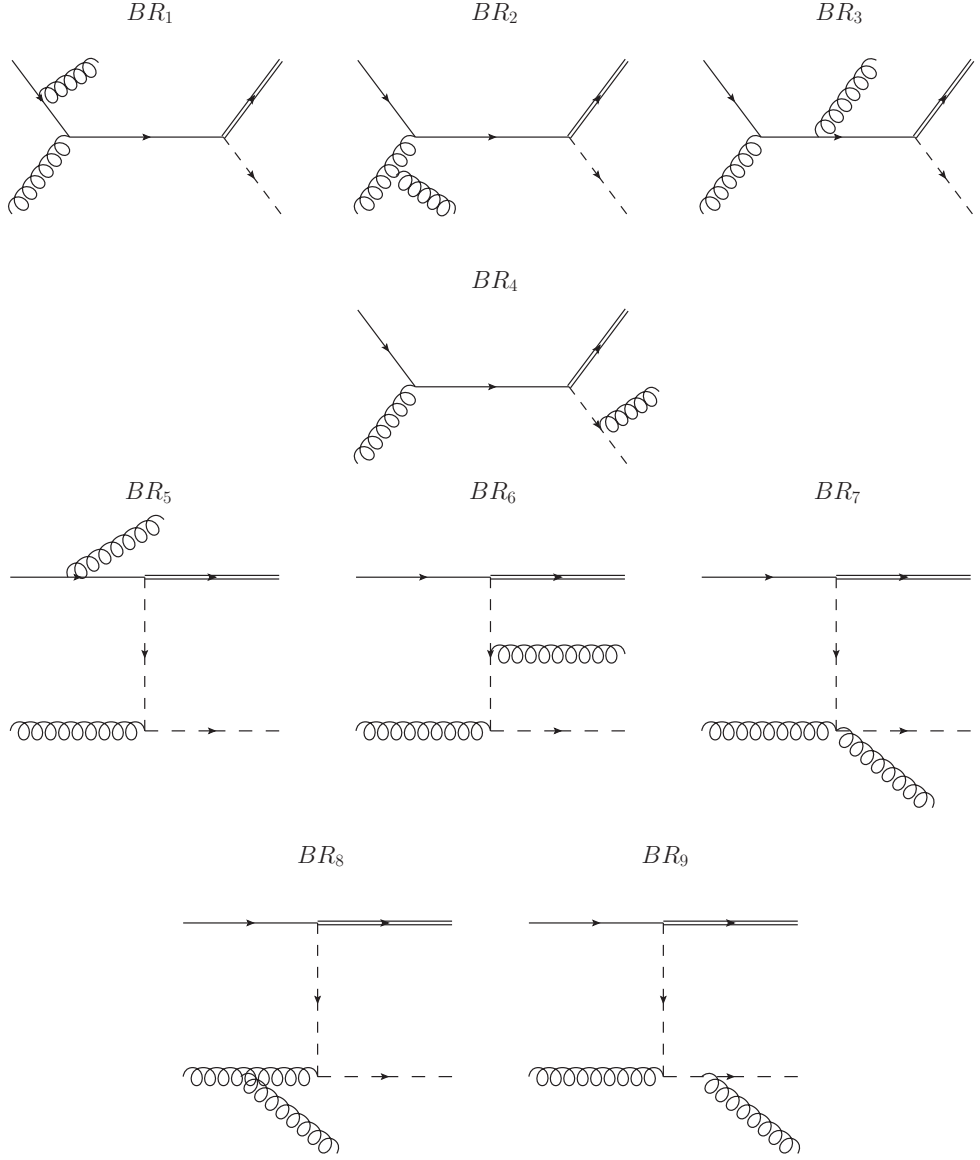


**Figure 3.15:** *QCD bremsstrahlung corrections to the LQ production process.*

where

$$\mathbf{T}_j \cdot \mathbf{T}_{ai} = -(C_F - C_A/2) \quad (3.13)$$

$$\mathbf{T}_{ai}^2 = C_F \quad (3.14)$$

$$\langle \mathbf{V}_j^{ai} \rangle = 8\pi\alpha_s C_F \left\{ \frac{2}{2 - x_{ij,a} - \tilde{z}_j} - 1 - x_{ij,a} \right\} \quad (3.15)$$

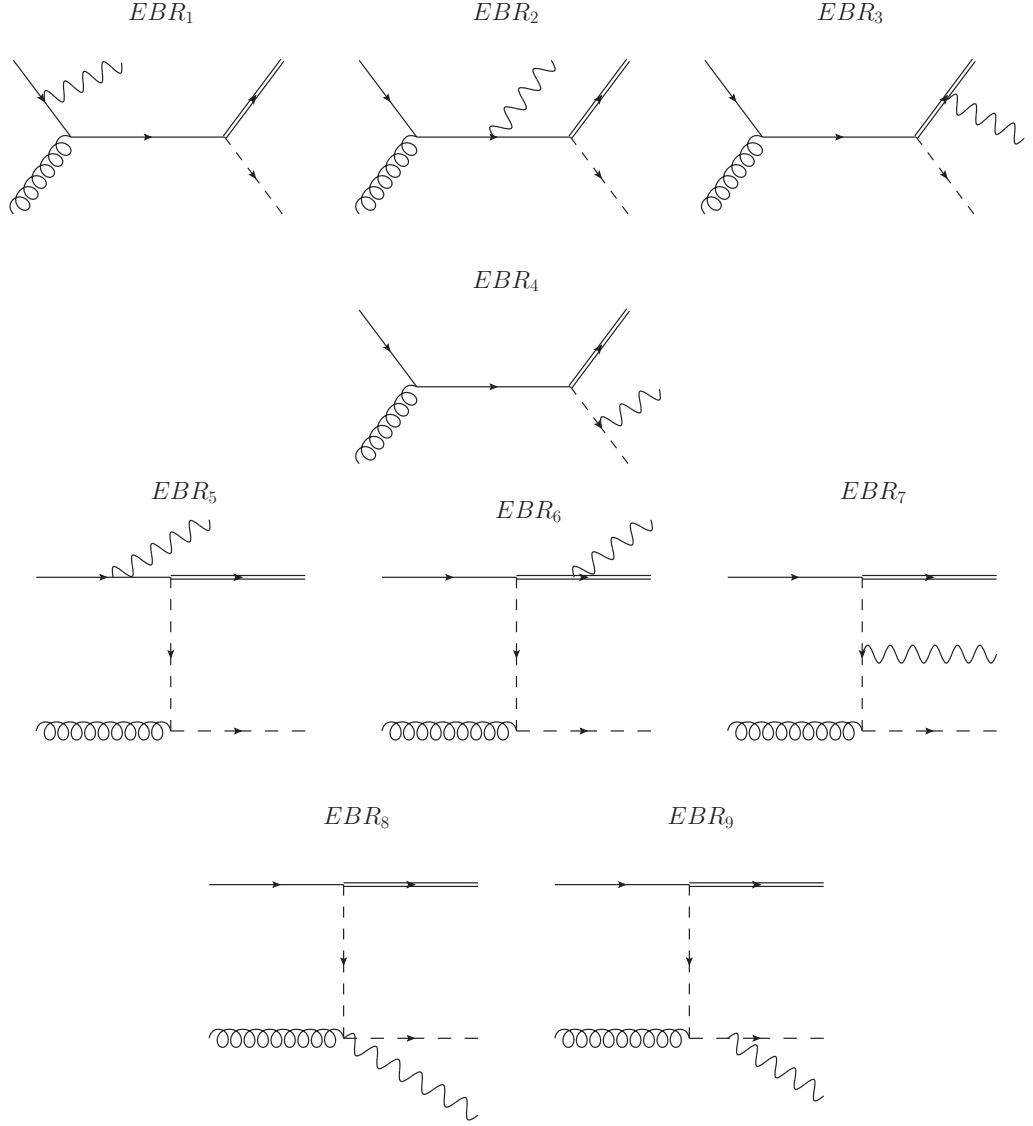


**Figure 3.16:** *QED bremsstrahlung corrections to the LQ production process.*

with

$$x_{ij,a} = \frac{p_1 \cdot q_{23} + p_1 \cdot k - p_1 \cdot q_{23}}{p_1 \cdot q_{23} + p_1 \cdot k} \quad (3.16)$$

$$\tilde{z}_j = \frac{p_1 \cdot q_{23}}{p_1 \cdot q_{23} + p_1 \cdot k} \quad (3.17)$$

The bra-ket component can be equivalently written as

$$\langle q_1, \tilde{q}_{23}; \tilde{p}_1, p_2 | q_1, \tilde{q}_{23}; \tilde{p}_1, p_2 \rangle \equiv |\mathcal{A}_{\text{tree}}|^2 (\tilde{p}_1, p_2; q_1, \tilde{q}_{23}) \quad (3.18)$$

where  $|\mathcal{A}_{\text{tree}}|^2 (\tilde{p}_1, p_2; q_1, \tilde{q}_{23})$  is the matrix element squared for the tree-level produc-

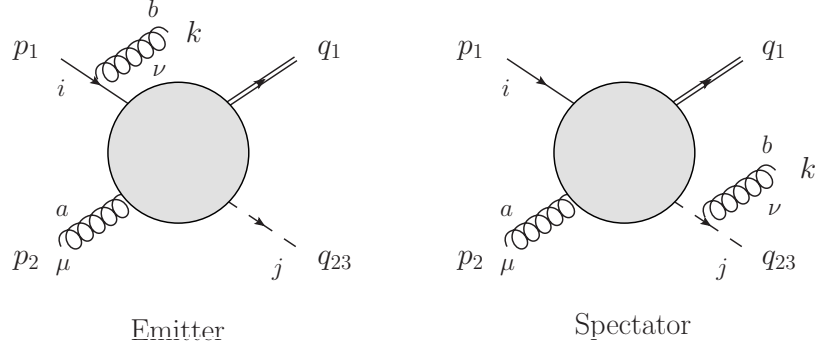


**Figure 3.17:** A diagrammatic representation of the dipole subtraction term for an initial-state emitter and final-state spectator indicating the momenta and colours of the various external particles.

tion process with momenta substitutions  $p_1 \rightarrow \tilde{p}_1$  and  $q_{23} \rightarrow \tilde{q}_{23}$  where

$$\tilde{p}_1^\mu = x_{ij,a} p_1^\mu \quad (3.19)$$

$$\tilde{q}_{23}^\mu = q_1^\mu + q_{23}^\mu - (1 - x_{ij,a}) p_1^\mu \quad (3.20)$$

For the LQ production process there is a second dipole term (with initial quark emitter and initial gluon spectator) which is also proportional to  $(p_1 \cdot k)^{-1}$ . Together these two dipole terms are responsible for cancelling the soft and collinear divergences which arise from a gluon emission from the incoming quark. The remaining four dipole subtraction terms will likewise cancel the soft and collinear divergences for emissions from the incoming gluon and outgoing LQ.<sup>3</sup>

Having calculated the dipole subtraction terms the corresponding insertion term also needs to be determined. In practice the insertions are all calculated together based on the final formulae section given in [29]. For the LQ production process, which has two initial-state partons, the insertion term has the following form

$$\begin{aligned} I(\epsilon, \mu^2; \{q_{23}, m_{\text{LQ}}\}, p_1, p_2) &= I_1(\epsilon, \mu^2; \{q_{23}, m_{\text{LQ}}\}, p_1) + I_2(\epsilon, \mu^2; \{q_{23}, m_{\text{LQ}}\}, p_2) \\ &+ \frac{\alpha_s}{2\pi} \left\{ \frac{1}{2} \frac{C_A}{C_F} \left[ \left( \frac{\mu^2}{s_{12}} \right)^\epsilon \left( \frac{C_F}{\epsilon^2} + \frac{\gamma_q}{\epsilon} \right) - C_F \frac{\pi^2}{3} + \gamma_q + K_q \right] \right. \\ &\left. + \frac{1}{2} \left[ \left( \frac{\mu^2}{s_{21}} \right)^\epsilon \left( \frac{C_A}{\epsilon^2} + \frac{\gamma_g}{\epsilon} \right) - C_A \frac{\pi^2}{3} + \gamma_g + K_g \right] \right\} \quad (3.21) \end{aligned}$$

<sup>3</sup>It should be noted that the scalar LQ is not a standard QCD particle and is treated as a scalar supersymmetric particle - a squark - within the dipole formalism.

with

$$\begin{aligned}
\mathbf{I}_1(\epsilon, \mu^2; \{q_{23}, m_{\text{LQ}}\}, p_1) = & \frac{\alpha_s}{2\pi} \frac{(C_F - C_A/2)}{C_F} \left\{ \right. \\
& \left[ C_F \left( \frac{\mu^2}{s_{31}} \right)^\epsilon \left( \mathcal{V}_{\tilde{q}}(s_{31}, m_{\text{LQ}}, 0, \{\}; \epsilon) - \frac{\pi^2}{3} \right) \right. \\
& \quad \left. + \Gamma_{\tilde{q}}(\mu, m_{\text{LQ}}, \{\}; \epsilon) + \gamma_{\tilde{q}} \ln \frac{\mu^2}{s_{31}} + \gamma_{\tilde{q}} + K_{\tilde{q}} \right] \\
& + \left[ C_F \left( \frac{\mu^2}{s_{13}} \right)^\epsilon \left( \mathcal{V}_q(s_{13}, 0, m_{\text{LQ}}, \{\}; \epsilon, 2/3) - \frac{\pi^2}{3} \right) \right. \\
& \quad \left. + \frac{\gamma_q}{\epsilon} + \gamma_q \ln \frac{\mu^2}{s_{13}} + \gamma_q + K_q \right] \left. \right\} \quad (3.22)
\end{aligned}$$

and

$$\begin{aligned}
\mathbf{I}_2(\epsilon, \mu^2; \{q_{23}, m_{\text{LQ}}\}, p_2) = & \frac{\alpha_s}{2\pi} \left\{ \frac{1}{2} \frac{C_A}{C_F} \left[ C_F \left( \frac{\mu^2}{s_{32}} \right)^\epsilon \left( \mathcal{V}_{\tilde{q}}(s_{32}, m_{\text{LQ}}, 0, \{\}; \epsilon) - \frac{\pi^2}{3} \right) \right. \right. \\
& \quad \left. + \Gamma_{\tilde{q}}(\mu, m_{\text{LQ}}, \{\}; \epsilon) + \gamma_{\tilde{q}} \ln \frac{\mu^2}{s_{32}} + \gamma_{\tilde{q}} + K_{\tilde{q}} \right] \\
& + \frac{1}{2} \left[ C_A \left( \frac{\mu^2}{s_{23}} \right)^\epsilon \left( \mathcal{V}_g(s_{23}, 0, m_{\text{LQ}}, \{\}; \epsilon, 2/3) - \frac{\pi^2}{3} \right) \right. \\
& \quad \left. + \frac{\gamma_g}{\epsilon} + \gamma_g \ln \frac{\mu^2}{s_{23}} + \gamma_g + K_g \right] \left. \right\} \quad (3.23)
\end{aligned}$$

where

$$s_{12} = s_{21} = 2 p_1 \cdot p_2 \quad (3.24)$$

$$s_{13} = s_{31} = 2 p_1 \cdot q_{23} \quad (3.25)$$

$$s_{23} = s_{32} = 2 p_2 \cdot q_{23} \quad (3.26)$$

To match the dipole subtractions the insertion term  $\mathbf{I}(\epsilon, \mu^2; q_1, q_{23}, p_1, p_2)$  has to be multiplied by the tree-level production process  $|\mathcal{A}_{\text{tree}}|^2(p_1, p_2; q_1, q_{23})$ .

Since the LQ production process contains initial state partons there are additional insertion terms which are required. These are essentially the Altarelli-Parisi splitting functions which are required because of uncanceled divergences in the ini-

tial state. To implement these additional terms requires, in turn, the momentum for each emitting incoming particle to be scaled by the longitudinal momentum fraction  $x$ . The final phase-space thus includes an extra integration over  $x$  ranging from 0 to 1.

When the momentum for the incoming quark (with momentum  $p_1$ ) is scaled the additional insertion terms are

$$\mathbf{P}(x; \mu_F^2; q_{23}, xp_1, p_2) = \mathbf{P}_m^{q,q}(x; \mu_F^2; q_{23}, xp_1) - \frac{\alpha_s}{2\pi} P^{qq}(x) \frac{1}{2} \frac{C_A}{C_F} \ln \frac{\mu_F^2}{xs_{12}} \quad (3.27)$$

and

$$\begin{aligned} \mathbf{K}(x; \{q_{23}, m_{\text{LQ}}\}, p_1, p_2) &= \mathbf{K}_m^{q,q}(x; \{q_{23}, m_{\text{LQ}}\}, p_1) \\ &+ \frac{\alpha_s}{2\pi} \frac{C_A}{2} \left\{ \frac{1}{C_F} P_{\text{reg}}^{qq}(x) \ln(1-x) \right. \\ &\left. + \left[ 2 \left( \frac{\ln(1-x)}{1-x} \right)_+ - \frac{\pi^2}{3} \delta(1-x) \right] \right\} \end{aligned} \quad (3.28)$$

These insertion terms need to be multiplied by the tree-level production process  $|\mathcal{A}_{\text{tree}}|^2(xp_1, p_2; q_1, q_{23})$  with  $p_1$  scaled by  $x$ .

When the momentum for the incoming gluon (with momentum  $p_2$ ) is scaled the insertion terms are

$$\mathbf{P}(x; \mu_F^2; q_{23}, p_1, xp_2) = \mathbf{P}_m^{g,g}(x; \mu_F^2; q_{23}, xp_2) - \frac{\alpha_s}{2\pi} P^{gg}(x) \frac{1}{2} \ln \frac{\mu_F^2}{xs_{21}} \quad (3.29)$$

and

$$\begin{aligned} \mathbf{K}(x; \{q_{23}, m_{\text{LQ}}\}, p_1, p_2) &= \mathbf{K}_m^{g,g}(x; \{q_{23}, m_{\text{LQ}}\}, p_2) \\ &+ \frac{\alpha_s}{2\pi} \frac{C_A}{2} \left\{ \frac{1}{C_A} P_{\text{reg}}^{gg}(x) \ln(1-x) \right. \\ &\left. + \left[ 2 \left( \frac{\ln(1-x)}{1-x} \right)_+ - \frac{\pi^2}{3} \delta(1-x) \right] \right\} \end{aligned} \quad (3.30)$$

These insertion terms also need to be multiplied by the tree-level production process, but with  $p_2$  scaled by  $x$ .

## QED corrections

The dipole subtraction method can also be used for the QED bremsstrahlung corrections. The whole approach is exactly the same as for the QCD case with the following two modifications. Firstly, since QED is a colourless Abelian gauge theory the colour factors need to be changed to  $C_F = 1$  and  $C_A = 0$ . Secondly, the strong coupling  $\alpha_s$  needs to be changed to the QED coupling  $\alpha_e$ .

In the QED case the dipole subtraction term (where the quark is the initial-state emitter with charge  $+2/3$  and the LQ is the final-state spectator with charge  $+5/3$ ) will have components

$$\mathbf{T}_j \cdot \mathbf{T}_{ai} = -\frac{10}{9} \quad (3.31)$$

$$\mathbf{T}_{ai}^2 = \frac{4}{9} \quad (3.32)$$

$$\langle \mathbf{V}_j^{ai} \rangle = 8\pi \frac{4}{9} \alpha_e \left\{ \frac{2}{2 - x_{ij,a} - \tilde{z}_j} - 1 - x_{ij,a} \right\} \quad (3.33)$$

with all other quantities as in the QCD case.

The insertion terms would also change accordingly, however they will have a slightly different form than the QCD corrections because for QED there is only one initial state parton to consider (i.e. the quark) because the photon does not couple to the gluon.

When considering QED bremsstrahlung corrections one should ideally use a corresponding PDF set which also includes QED corrections in the parton evolution, however it has been shown that including QED corrections does not have a significant effect on the evolution (see for example [37]). Therefore, to good approximation, we are justified in using the CTEQ6M and CTEQ6L PDF sets, which only include QCD corrections.

### 3.2.6 Bremsstrahlung Corrections to the Decay Process

For the LQ decay process there is no initial state collinear singularity since the initial state is a massive LQ. Also the structure of infrared singularities is sufficiently

straightforward that the cancellations can be carried out analytically without resorting to the dipole subtraction method.

### QCD corrections

The QCD bremsstrahlung corrections involve a gluon emission from the incoming LQ leg and the outgoing quark leg (see figure 3.18). By parametrising the momenta

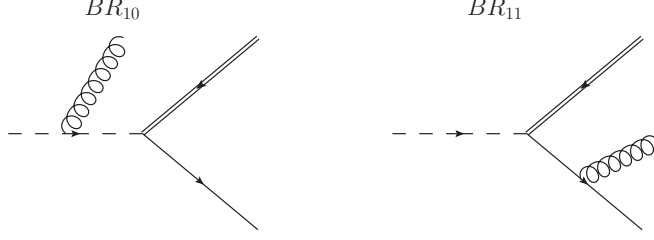


**Figure 3.18:** *QCD bremsstrahlung corrections to the LQ decay process.*

for the decay process, as described in appendix E, the 3-body phase-space (with the bremsstrahlung momentum evaluated in  $d = 4 - 2\epsilon$  dimensions) can be given in terms of the variables  $y$  and  $z$  giving

$$\int d^3_{\text{LIPS}} = \frac{1}{128\pi^3} m_{\text{LQ}}^2 \left( \frac{m_{\text{LQ}}^2}{\mu^2} \right)^{-\epsilon} \int_0^1 dy \int_0^1 dz \frac{1-y}{(1-yz)^2} y^{1-2\epsilon} z^{-\epsilon} (1-z)^{-\epsilon} \quad (3.34)$$

With this parametrisation of the phase-space the decay process  $|\mathcal{A}_{\text{decay brems}}|^2$  becomes a function of  $y$  and  $z$ , and combining this with  $d^3_{\text{LIPS}}$  the bremsstrahlung decay-width is given by

$$\Gamma_{\text{brem}} = \frac{1}{256\pi^3} \left( \frac{m_{\text{LQ}}^2}{\mu^2} \right)^{-\epsilon} \int_0^1 dy \int_0^1 dz \frac{1-y}{(1-yz)^2} y^{1-2\epsilon} z^{-\epsilon} (1-z)^{-\epsilon} |\mathcal{A}_{\text{decay brems}}(y, z)|^2 \quad (3.35)$$

With  $|\mathcal{A}_{\text{decay brems}}|^2$  evaluated in FORM and combined with the integration measure as shown in eq.(3.35) the final result is an expression containing a series of integrals of the form

$$\int_0^1 dy y^\alpha (1-y)^\beta \int_0^1 dz z^\gamma (1-z)^\delta \quad (3.36)$$

or

$$\int_0^1 dy y^\alpha (1-y)^\beta \int_0^1 dz z^\gamma \frac{(1-z)^\delta}{(1-yz)^\eta} \quad (3.37)$$

For some values of the parameters  $\alpha, \beta, \gamma, \delta$  and  $\eta$  these integrals are divergent, but by working in  $d = 4 - 2\epsilon$  these divergences are regularised. Using Mathematica the integrals were evaluated as a series expansion in  $\epsilon$  to give the final result as

$$\Gamma_{\text{brem}} = \frac{1}{256\pi^3} g^2 g_{\text{LQ}}^2 m_{\text{LQ}} C_F \left( \frac{m_{\text{LQ}}^2}{\mu^2} \right)^{-\epsilon} \left[ \frac{4}{\epsilon^2} + \frac{10}{\epsilon} + 23 + \frac{2}{3}\pi^2 \right] \quad (3.38)$$

### QED corrections

The same analytic approach used for the QCD corrections can also be applied to the QED corrections, which are shown in figure 3.19. With the QED corrections there

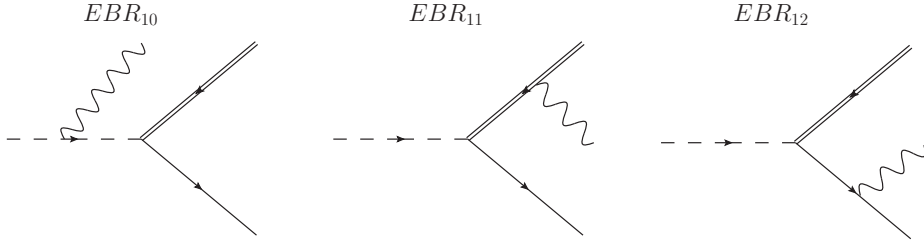


**Figure 3.19:** *QED bremsstrahlung corrections to the LQ decay process.*

is an extra diagram because the photon couples to the lepton, other than this the procedure follows as before giving the final result as

$$\Gamma_{\text{brem}} = \frac{1}{256\pi^3} e^2 g_{\text{LQ}}^2 m_{\text{LQ}} \left( \frac{m_{\text{LQ}}^2}{\mu^2} \right)^{-\epsilon} \frac{1}{9} \left[ \frac{52}{\epsilon^2} + \frac{178}{\epsilon} + 467 + \frac{26}{3}\pi^2 \right] \quad (3.39)$$

### 3.2.7 Combining the Production and Decay Processes

For NLO calculations the amplitudes for the tree level and virtual corrections - having the same initial and final states - are added together to give

$$\mathcal{A}_{\text{tree+virtual}}^P = \mathcal{A}_{\text{tree}}^P + \sum_{\{\text{QCD,EW,LQ}\}} \mathcal{A}_{\text{virtual}}^P \quad (3.40)$$

where the sum in the second term is over the QCD, electroweak and LQ virtual corrections and the  $P$  superscript is to indicate that these are production amplitudes.



At NLO the matrix element squared  $|\mathcal{A}_{\text{tree+virtual}}|^2$  is thus<sup>4</sup>

$$|\mathcal{A}_{\text{tree+virtual}}^P|^2 \rightarrow \underbrace{\mathcal{A}_{\text{tree}}^P (\mathcal{A}_{\text{tree}}^P)^\dagger}_{|\mathcal{A}_{\text{tree}}^P|^2} + \sum_{\{\text{QCD,EW,LQ}\}} \underbrace{\mathcal{A}_{\text{tree}}^P (\mathcal{A}_{\text{virtual}}^P)^\dagger + (\mathcal{A}_{\text{tree}}^P)^\dagger \mathcal{A}_{\text{virtual}}^P}_{|\mathcal{A}_{1\text{-loop}}^P|^2} \quad (3.41)$$

where the remaining terms are dropped because they contribute to the NNLO corrections. At NLO the squared matrix element is a sum of the tree-level and the 1-loop matrix elements,  $|\mathcal{A}_{\text{tree}}^P|^2$  and  $|\mathcal{A}_{1\text{-loop}}^P|^2$ . It should be noted that in this notation  $|\mathcal{A}_{1\text{-loop}}^P|^2$  is not to be mistaken for an amplitude squared, instead it is the interference between the tree and virtual amplitudes giving the NLO corrections to the process.

The bremsstrahlung corrections for the production process - having a three-body final state - are squared on their own to give  $\sum_{\{\text{QCD,QED}\}} |\mathcal{A}_{\text{brem}}^P|^2$  where the sum is over the QCD and QED bremsstrahlung corrections.

Both  $|\mathcal{A}_{1\text{-loop}}^P|^2$  and  $|\mathcal{A}_{\text{brem}}^P|^2$  contain infrared divergences which are dealt with by using the dipole subtraction method. Implementing the dipole subtraction method the total production cross-section at NLO<sup>5</sup> is

$$\begin{aligned} \sigma_{\text{NLO}}^P = & \underbrace{\frac{1}{2s} \int d_{\text{LIPS}}^2 |\mathcal{A}_{\text{tree}}^P|^2}_{\sigma_{\text{tree}}} + \sum_{\{\text{QCD,EW,LQ}\}} \underbrace{\frac{1}{2s} \int d_{\text{LIPS}}^2 |\mathcal{A}_{1\text{-loop}}^P|^2 + I \otimes |\mathcal{A}_{\text{tree}}^P|^2}_{\sigma_{1\text{-loop}}} \\ & + \sum_{\{\text{QCD,QED}\}} \underbrace{\frac{1}{2s} \int d_{\text{LIPS}}^3 |\mathcal{A}_{\text{brem}}^P|^2 - D \otimes |\mathcal{A}_{\text{tree}}^P|^2}_{\sigma_{\text{brem}}} \\ & + \sum_{\{\text{QCD,QED}\}} \underbrace{\frac{1}{2s} \int_0^1 dx \int d_{\text{LIPS}}^2(x) (P + K) \otimes (|\mathcal{A}_{\text{tree}}^P|^2)}_{\sigma_{\text{A-P}}} \end{aligned} \quad (3.42)$$

where  $I \otimes |\mathcal{A}_{\text{tree}}^P|^2$  and  $D \otimes |\mathcal{A}_{\text{tree}}^P|^2$  are the dipole insertions and subtractions respectively and  $\sigma_{\text{A-P}}$  are the Altarelli-Parisi splitting functions due to the initial-state

<sup>4</sup>In calculating all of the squared matrix elements it should be noted that summing over helicities and averaging over incoming helicities and initial colour states has also been included.

<sup>5</sup>After implementing the dipole subtraction method the total production cross-section at NLO still contains ultraviolet divergences. In the  $\overline{\text{MS}}$ -scheme these divergences are removed by subtracting the remaining single pole from the final result.

singularities.

The details of the parametrisation of the 2-body and 3-body Lorentz invariant phase-spaces  $d_{\text{LIPS}}^2$ ,  $d_{\text{LIPS}}^3$  and scaled 2-body phase-space  $d_{\text{LIPS}}^2(x)$  in eq.(3.42) are given in appendix E.

It should be noted that the cross-section shown in eq.(3.42) is at the parton level. To calculate the physical cross-section each of the terms in eq.(3.42) must be folded with  $f_u$  and  $f_g$  - the PDFs for the u-quark and gluon respectively. To illustrate the folding process,  $\sigma_{\text{tree}}$  has been used as an example:

$$\sigma_{\text{tree}} \rightarrow \int_0^1 dx_1 \int_0^1 dx_2 [f_u(x_1, \mu_F) f_g(x_2, \mu_F) + f_u(x_2, \mu_F) f_g(x_1, \mu_F)] \sigma_{\text{tree}}(x_1 x_2 s) \quad (3.43)$$

with the folding of the remaining terms in eq.(3.42) done in the same way. The integration variables  $x_1$  and  $x_2$  represent the proportion of the energy taking part in the parton level collision. It should be noted that the expression in eq.(3.43) is symmetric in  $x_1$  and  $x_2$  and accounts for the fact that u-quark and gluon could come from *either* proton in the collision.

*Note: To keep the notation compact it is to be understood that  $\sigma_{\text{NLO}}^P$ ,  $\sigma_{\text{tree}}$  etc. now represent the folded cross-sections.*

The procedure for calculating the total decay-width follows in a similar way to the production cross-section. The final expression for the total-decay width is

$$\Gamma_{\text{NLO}} = \underbrace{\frac{1}{2m_{\text{LQ}}} \int d_{\text{LIPS}}^2 |\mathcal{A}_{\text{tree}}^D|^2}_{\Gamma_{\text{tree}}} + \sum_{\{\text{QCD,EW,LQ}\}} \underbrace{\frac{1}{2m_{\text{LQ}}} \int d_{\text{LIPS}}^2 |\mathcal{A}_{1\text{-loop}}^D|^2}_{\Gamma_{1\text{-loop}}} + \sum_{\{\text{QCD,QED}\}} \underbrace{\frac{1}{2m_{\text{LQ}}} \int d_{\text{LIPS}}^3 |\mathcal{A}_{\text{brem}}^D|^2}_{\Gamma_{\text{brem}}} \quad (3.44)$$

where the  $D$  superscript is to indicate that these are the decay amplitudes. Since the infrared divergences in  $\Gamma_{\text{brem}}$  have been regularised in  $d$ -dimensions the total decay-width is infrared finite.

Combining eq.(3.42) and eq.(3.44) the NWA gives the total cross-section at

NLO as

$$\begin{aligned}
\sigma_{\text{NLO}} \approx & \frac{m_{\text{LQ}}}{\pi} \int_0^s dp^2 \frac{1}{(p^2 - m_{\text{LQ}}^2)^2 + m_{\text{LQ}}^2 (\Gamma^{\text{tot}})^2} \left[ \sigma_{\text{tree}} \times \Gamma_{\text{tree}} \right. \\
& + \sum_{\{\text{QCD,EW,LQ}\}} (\sigma_{\text{tree}} \times \Gamma_{1\text{-loop}} + \sigma_{1\text{-loop}} \times \Gamma_{\text{tree}}) \\
& \left. + \sum_{\{\text{QCD,QED}\}} (\sigma_{\text{tree}} \times \Gamma_{\text{brem}} + \sigma_{\text{brem}} \times \Gamma_{\text{tree}} + \sigma_{\text{A-P}} \times \Gamma_{\text{tree}}) \right] \quad (3.45)
\end{aligned}$$

This expression does not include all terms from the product  $\sigma_{\text{NLO}}^P \times \Gamma_{\text{NLO}}$  because some of the terms are part of the NNLO calculations. Also being a scalar there is no sum over the LQ helicity and since the  $R_2$  scalar LQ has only one decay channel  $\Gamma^{\text{tot}} = \Gamma_{\text{tree}}$ .

The expression for the total decay-width  $\Gamma^{\text{tot}}$  is

$$\Gamma^{\text{tot}} = \frac{1}{24\pi} [h_{1L}^2 + h_{1R}^2] m_{\text{LQ}} = 22.86 \text{ GeV} \quad (3.46)$$

and since  $m_{\text{LQ}} = 750 \text{ GeV}$  this confirms the validity of the NWA.

### 3.2.8 Additional NLO contributions in the NWA

The physical process we are interested in is the collision between two protons - producing a single intermediate scalar LQ which subsequently decays into an anti-lepton and a jet and the quantity we are interested in is the distribution of the invariant mass of this anti-lepton/jet system. At LO (within the NWA) the only contribution to this process is the one described above (i.e. the u-quark/gluon initial state) <sup>6</sup>, however when going to NLO there are additional partonic initial state contributions which need to be included.

The additional NLO contributions are grouped into three different classes, depending on their initial state (see figure 3.20). These contributions are all tree-level

---

<sup>6</sup>The process with an anti-u-quark and gluon in the initial state produces the same final state (i.e. a lepton, anti-lepton and a jet), however it is not valid to include this within the NWA approximation. The reason for this is because the anti-lepton/jet system is now composed of an anti-lepton from the on-shell production process and the jet from the on-shell decay process which is not a valid distribution within the NWA.

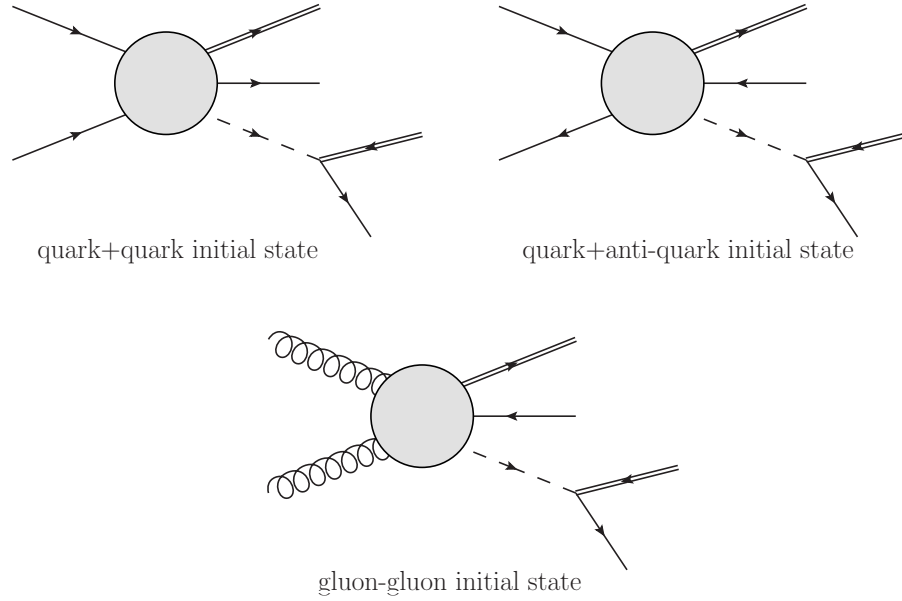


**Figure 3.20:** *The additional factorisable NLO contributions to the  $LQ$  production process.*

graphs, some of which contain initial state singularities (see figure 3.21). In principal

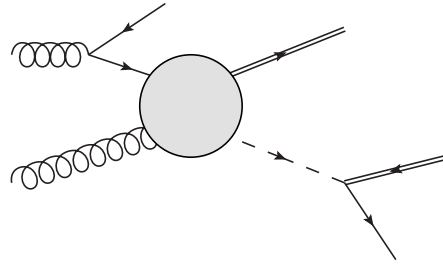


**Figure 3.21:** *An example process with an initial state singularity. In this example the singularity occurs when the radiated anti-quark becomes collinear to the internal quark line.*

these initial state singularities could be regulated by introducing a transverse momentum ( $p_T$ ) cut-off, in which case the calculations could be done using a program such as CalcHEP [38] - a tool which automatically evaluates tree-level Feynman diagrams.

Introducing a  $p_T$  cut-off, however, would be inconsistent with the dipole subtraction method, which is implemented as an inclusive calculation (i.e. without a  $p_T$  cut-off). Therefore, for consistency, the initial state singularities arising from the additional NLO contributions also need to be dealt with using the dipole subtraction method.

Since the additional NLO contributions only involve initial state singularity

ties and there are no corresponding NLO virtual corrections the dipole subtraction method in this instance does not contain any insertion terms. Instead there are only the dipole subtraction terms, which render the additional NLO contributions infrared finite, and the corresponding  $P(x)$  and  $K(x)$  Altarelli-Parisi splitting functions (see eq.(2.42)). These are for the uncanceled initial state singularities, which are dealt with in the PDFs (see section 2.2.1).

### 3.2.9 Validating the Results: The Ward-Takahashi identity

Having calculated all of the contributions to LQ production in the NWA it is important to validate them before producing the final results. There are a large number of Feynman diagrams, particularly with regards to the virtual corrections, and it is important to ensure that all of them have been included and there are no errors in the calculations.

Since most of the Feynman diagrams, with the exception of the tree-level LQ decay process, have at least one external gauge boson the most useful check that can be performed is to confirm the Ward-Takahashi identity. For a process  $\mathcal{A}^\mu$  with an external gauge boson (i.e. a photon or gluon) with Lorentz index  $\mu$  and momentum  $k$  the Ward-Takahashi identity states that

$$k_\mu \mathcal{A}^\mu(k) = 0 \quad (3.47)$$

The Ward-Takahashi identity confirms that the process is gauge invariant and the check is performed by contracting the gauge boson with its own momenta - as shown in eq.(3.47).

For example, the virtual corrections to the LQ production process have one external gauge boson - a gluon with momentum  $p_2$  and Lorentz index  $\mu$ . By contracting  $\mathcal{A}_{\text{virtual}}^P$  with  $p_2^\mu$  and checking the result is zero confirms that all of the contributions have been included and there are no issues with colour factors or sign errors etc.

The Ward-Takahashi identity has been used on all diagrams and has confirmed that all contributions have been included and are correct (i.e. they all form gauge

invariant sets).

### 3.2.10 Results in the NWA

Having validated the calculations with the Ward-Takahashi identity and combined the production and decay processes we can present the results of LQ production in the NWA.

These results show the differential cross-section versus the invariant mass of the jet + anti-lepton system. From eq.(3.45) the invariant mass is defined by the integration variable  $p^2$ , for producing the results the range was taken to be  $0 < p < 2m_{LQ}$ .

Looking first at the CTEQ6M results, figure 3.22 shows the LO contribution. As can be seen from the plot the NWA provides a symmetrical resonance with a peak

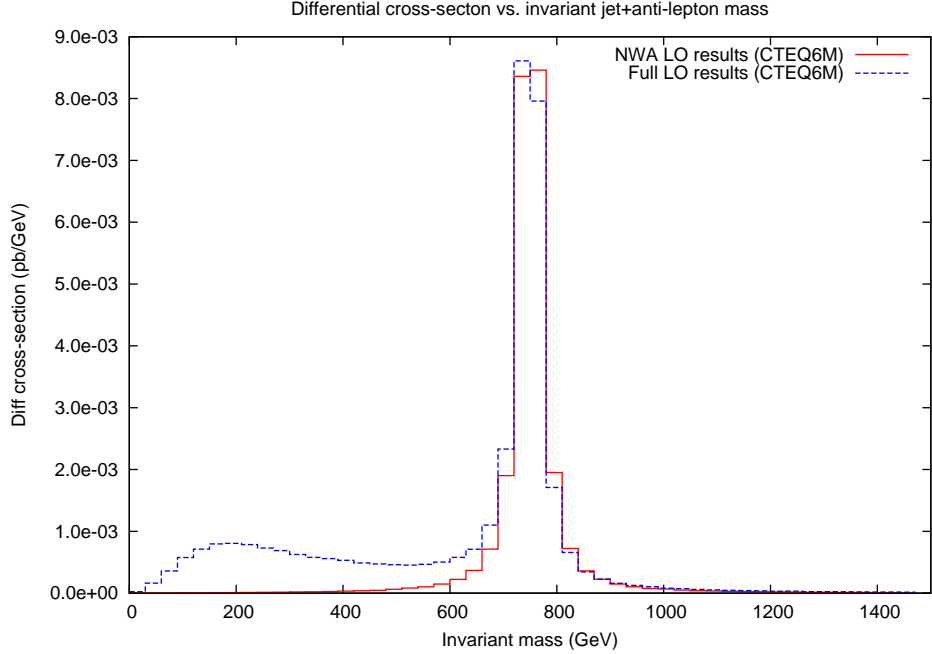


**Figure 3.22:** *LO results for producing a scalar  $LQ$  - comparing the NWA to the full non-factorisable process (CTEQ6M).*

near  $m_{LQ} = 750 \text{ GeV}$  with a height of  $8.46 \times 10^{-3} \text{ pb/GeV}$ . The total cross-section at LO is  $0.74 \text{ pb}$

For easier comparison the results for the NWA and the full non-factorisable process are usually combined into a single plot. As can be seen (for example in figure 3.22) the NWA and non-factorisable results both exhibit the same resonant behaviour which is due to the production of an on-shell LQ. Away from the resonant region there is an enhancement to the full non-factorisable distribution and this is due to the non-factorisable contributions which are ignored in the NWA. These are common features which will be seen throughout - for both scalar and vector LQs.

The NLO calculations can be split into QCD, electroweak, LQ contributions along with the additional NLO calculations. The QCD corrections include the virtual gluon loop corrections along with bremsstrahlung process with a radiated gluon. Referring to figure 3.23 the QCD corrections make a significant contribution to the

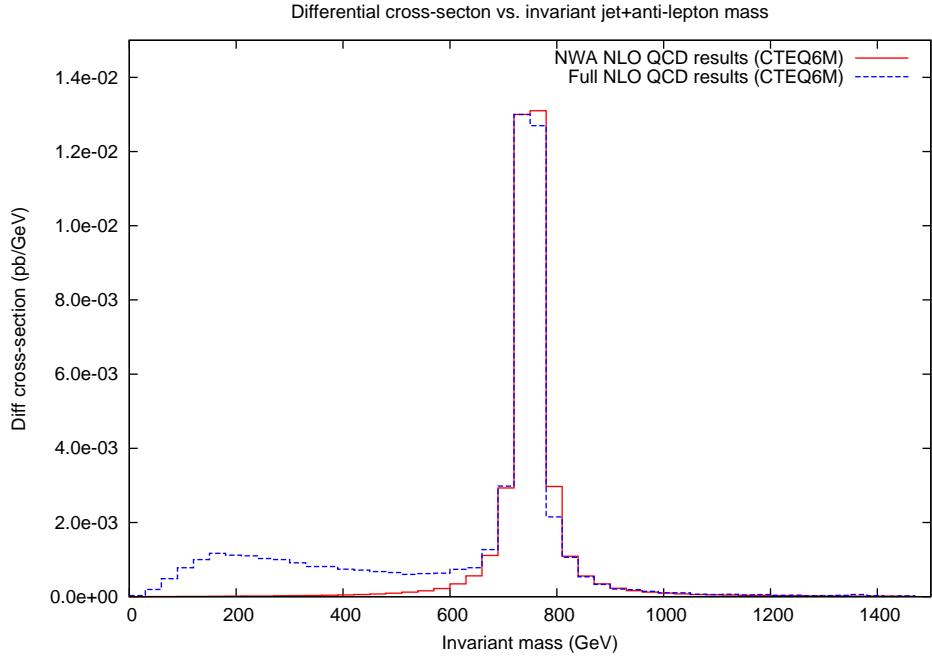


**Figure 3.23:** *NLO results for producing a scalar LQ - comparing the NWA to the full non-factorisable process (CTEQ6M). These results include the QCD corrections only.*

process. There is still a symmetric resonant peak, but now with a height of  $1.31 \times 10^{-2}$  pb/GeV which gives an enhancement of 55% over the LO result. For the QCD corrections the total cross-section is 1.14 pb giving an increase of 54% over the LO

result.

The electroweak corrections include the virtual photon, W and Z-boson loop corrections along with the bremsstrahlung process with a radiated photon. From

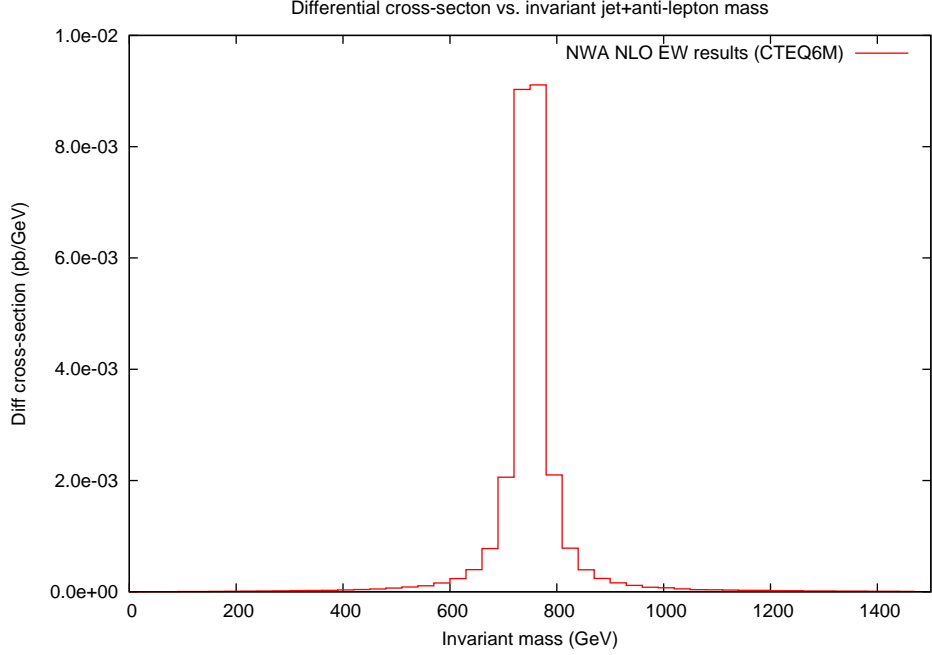


**Figure 3.24:** *NLO results for producing a scalar LQ in the NWA (CTEQ6M). These results include the electroweak corrections only, which are neglected in the full non-factorisable process.*

figure 3.24 it can be seen that, in comparison to the QCD corrections, the electroweak corrections provide only a small enhancement to the LO process. The height of the resonant peak is  $9.11 \times 10^{-3}$  pb/GeV, giving an enhancement of 8% over the LO result. The EW corrections have a total cross-section of 0.80 pb giving an increase of 8% over the LO result.

The LQ corrections include virtual LQ and fermion loop corrections (see for example figure 3.9) and, being infrared finite, do not include bremsstrahlung processes. From figure 3.25 it is clear that the effect of the LQ corrections are opposite to the QCD and electroweak corrections. Instead of enhancing the LO result the LQ corrections decrease it. The height of the resonant peak is decreased to  $6.24 \times 10^{-3}$  pb/GeV giving a reduction over the LO result by 26%. The LQ corrections give a total cross-



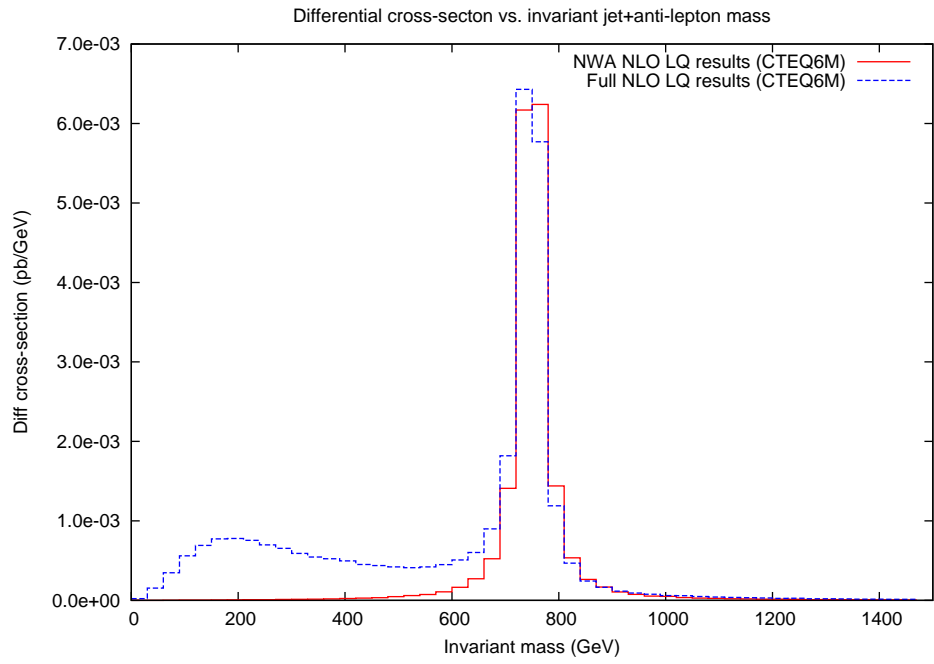


**Figure 3.25:** *NLO results for producing a scalar  $LQ$  - comparing the NWA to the full non-factorisable process (CTEQ6M). These results include the  $LQ$  corrections only.*

section of 0.55 pb which decreases the LO result by 26%.

Finally the additional contributions are shown in figure 3.26. These additional

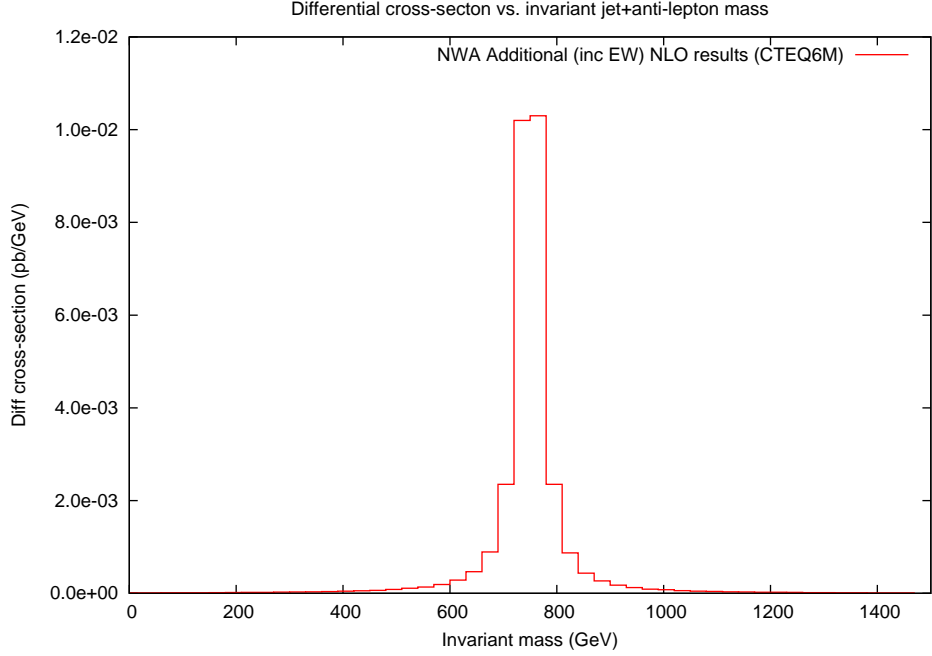


**Figure 3.26:** Additional NLO results for producing a scalar LQ in the NWA (CTEQ6M). In addition to the QCD and LQ corrections these results include the EW corrections, which are neglected in the full non-factorisable process.

contributions also enhance the LO process. The height of the resonant peak is  $1.02 \times 10^{-2}$  pb/GeV giving an enhancement of 21% over the LO result. The total cross-section is 0.91 pb which gives an increase over the LO result of 23%.

The combined results are shown in figure 3.27 and give the total NLO contributions to the LQ production process in the NWA. The total NLO contributions give a resonant peak height of  $1.33 \times 10^{-2}$  adding a sizeable enhancement of 57% to the LO result. The total cross-section at NLO is 1.17 pb which gives a 58% increase over the LO result. These results are summarised in tables 3.1 and 3.2.

The above results were obtained by folding the parton-level results with the CTEQ6M PDF set. To determine the impact of the choice of PDF sets the results were recalculated using the CTEQ6L PDF set. It was found that the choice of PDF

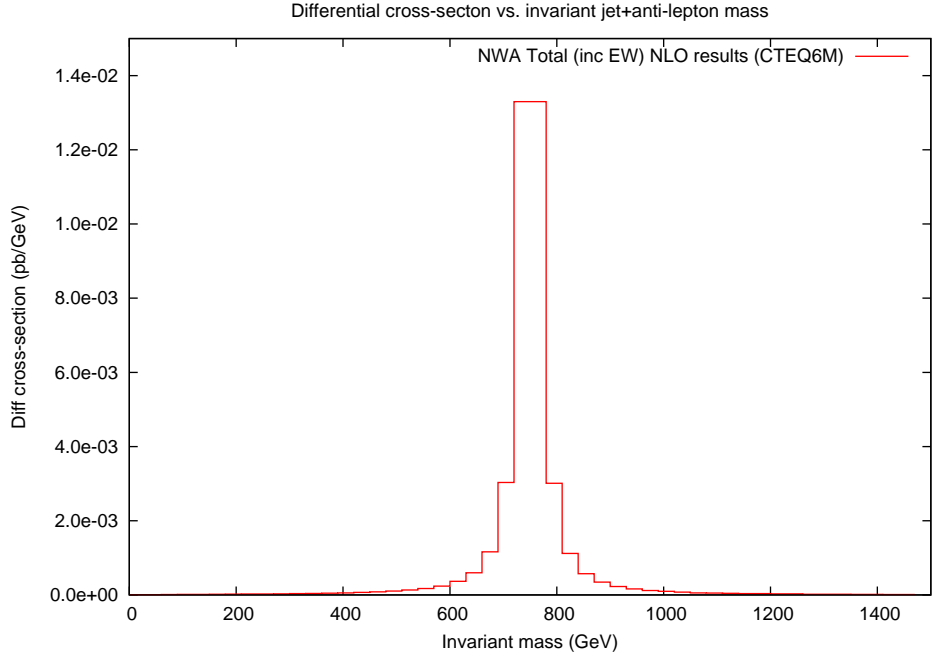


**Figure 3.27:** Total NLO results for producing a scalar LQ in the NWA (CTEQ6M). In addition to the QCD and LQ corrections these results include the EW corrections, which are neglected in the full non-factorisable process.

Correction Type	Peak Height (pb/GeV)	Percentage change on LO
Tree	$8.46 \times 10^{-3}$	-
QCD	$1.31 \times 10^{-2}$	+55%
EW	$9.11 \times 10^{-3}$	+8%
LQ	$6.24 \times 10^{-3}$	-26%
Additional	$1.02 \times 10^{-2}$	+21%
Total	$1.33 \times 10^{-2}$	+57%

**Table 3.1:** Summary of the CTEQ6M scalar results for the NWA.

Correction Type	Total cross-section (pb)	Percentage change on LO
Tree	0.74	-
QCD	1.14	+54%
EW	0.80	+8%
LQ	0.55	-26%
Additional	0.91	+23%
Total	1.17	+58%

**Table 3.2:** Summary of the CTEQ6M scalar results for the NWA.

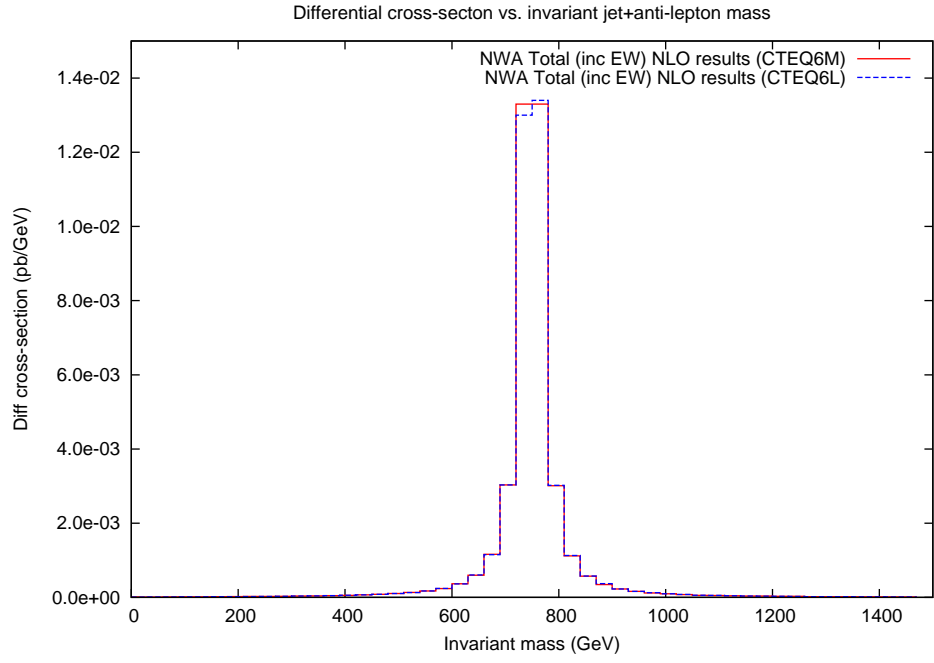


**Figure 3.28:** Total NLO results for producing a scalar  $LQ$  in the NWA comparing the CTEQ6M and CTEQ6L PDF sets. These results include the QCD and  $LQ$  corrections as well as the EW corrections.

set did not make much of a difference to the end result. As can be seen from figure 3.28 the CTEQ6L presents a very similar distribution to CTEQ6M. The full CTEQ6L results are summarised in tables 3.3 and 3.4.

Correction Type	Peak Height (pb/GeV)	Percentage change on LO
Tree	$8.43 \times 10^{-3}$	-
QCD	$1.31 \times 10^{-2}$	+55%
EW	$9.11 \times 10^{-3}$	+8%
LQ	$6.23 \times 10^{-3}$	-26%
Additional	$1.03 \times 10^{-2}$	+22%
Total	$1.34 \times 10^{-2}$	+58%

**Table 3.3:** *Summary of the CTEQ6L scalar results in the NWA.*

Correction Type	Total cross-section (pb)	Percentage change on LO
Tree	0.73	-
QCD	1.13	+55%
EW	0.79	+8%
LQ	0.54	-26%
Additional	0.90	+23%
Total	1.16	+59%

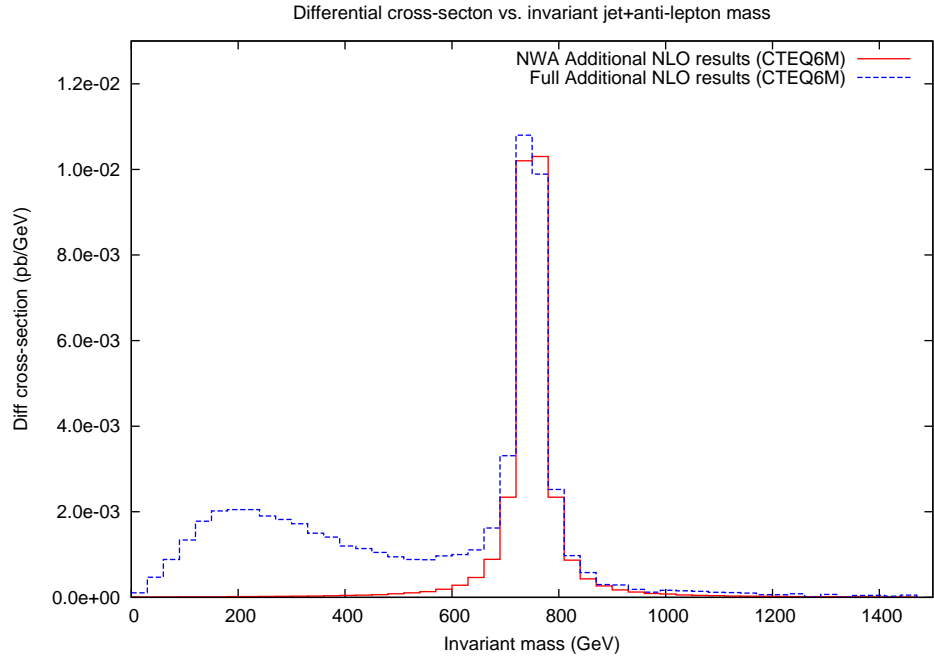
**Table 3.4:** *Summary of the CTEQ6L scalar results in the NWA.*

### QCD and LQ Corrections Only

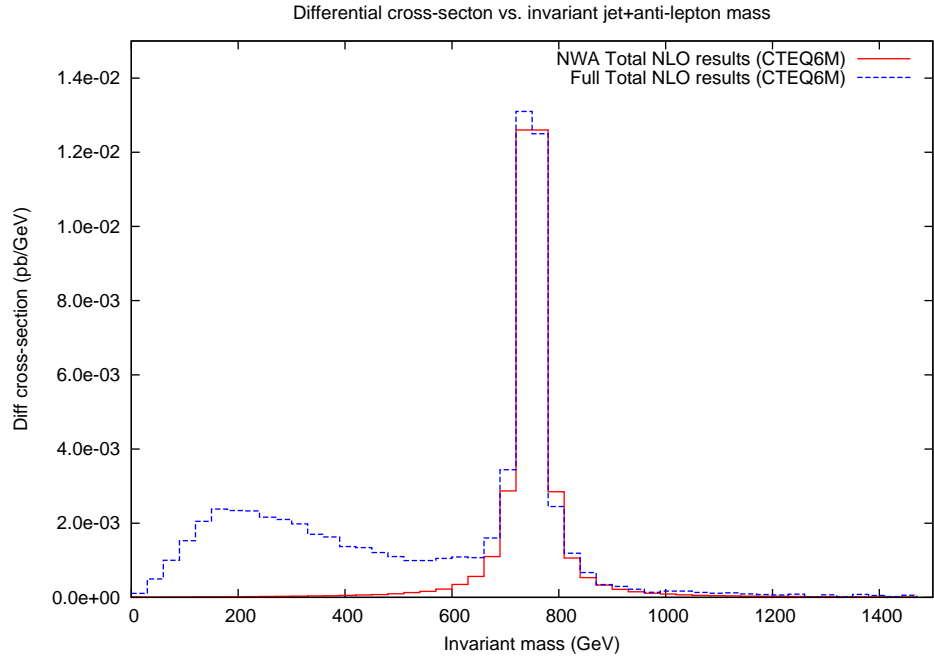
From the above results it is clear that the main contributions come from the QCD and LQ corrections and for this reason the electroweak corrections will be excluded when calculating the non-factorisable process. Therefore, to make a valid comparison between the NWA and the non-factorisable process we must compile a set of NWA results which exclude the EW corrections. Most of the corrections have already been separated into different types, however the additional calculations had to be rerun to exclude the EW contributions (see figure 3.29).

Figure 3.30 shows the total QCD and LQ contributions for the CTE6QM folding. When the electroweak corrections are neglected there is still a large enhancement to the resonant peak of 49% and also a large increase to the total cross-section of 50%.

To make a comparison between the LO and total NLO QCD and LQ contri-



**Figure 3.29:** *Additional NLO results for producing a scalar  $LQ$  - comparing the NWA to the full non-factorisable process (CTEQ6M). These results include the QCD and  $LQ$  corrections only.*



**Figure 3.30:** Total NLO results for producing a scalar  $LQ$  - comparing the NWA to the full non-factorisable process (CTEQ6M). These results include the QCD and  $LQ$  corrections only.

butions these are combined and shown in figure 3.31.

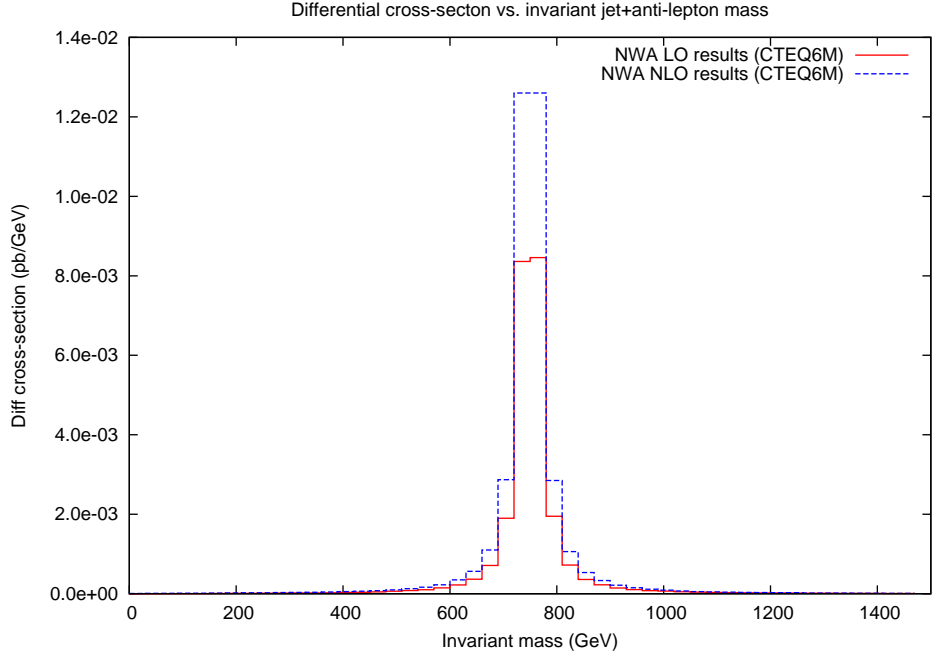


**Figure 3.31:** A comparison between the LO and NLO contributions for producing a scalar LQ in the NWA (CTEQ6M). These results include the QCD and LQ corrections only.

As before, the CTEQ6L folding produced very similar result to the CTEQ6M folding. A summary of the results of the QCD and LQ corrections are shown in tables 3.5 and 3.6 for the CTEQ6M results and tables 3.7 and 3.8 for the CTEQ6L results.

Correction Type	Peak Height (pb/GeV)	Percentage change on LO
Tree	$8.46 \times 10^{-3}$	-
QCD	$1.31 \times 10^{-2}$	+55%
LQ	$6.24 \times 10^{-3}$	-26%
Additional (ex EW)	$1.03 \times 10^{-2}$	+22%
Total	$1.26 \times 10^{-2}$	+49%

**Table 3.5:** Summary of the CTEQ6M scalar results in the NWA including QCD and LQ corrections only.



Correction Type	Total cross-section (pb)	Percentage change on LO
Tree	0.74	-
QCD	1.14	+54%
LQ	0.55	-26%
Additional (ex EW)	0.90	+22%
Total	1.11	+50%

**Table 3.6:** *Summary of the CTEQ6M scalar results in the NWA including QCD and LQ corrections only.*

Correction Type	Peak Height (pb/GeV)	Percentage change on LO
Tree	$8.43 \times 10^{-3}$	-
QCD	$1.31 \times 10^{-2}$	+55%
LQ	$6.23 \times 10^{-3}$	-26%
Additional (ex EW)	$1.02 \times 10^{-2}$	+21%
Total	$1.27 \times 10^{-2}$	+51%

**Table 3.7:** *Summary of the CTEQ6L scalar results in the NWA including QCD and LQ corrections only.*

Correction Type	Total cross-section (pb)	Percentage change on LO
Tree	0.73	-
QCD	1.13	+55%
LQ	0.54	-26%
Additional (ex EW)	0.89	+22%
Total	1.11	+52%

**Table 3.8:** *Summary of the CTEQ6L scalar results in the NWA including QCD and LQ corrections only.*

### 3.3 Scalar Leptoquarks: The Full Non-Factorisable Process

All of the production and decay diagrams discussed within the context of the NWA will be needed when calculating the full non-factorisable process, but now we need to include the additional non-factorising topologies as well.

At LO the factorisable production and decay diagrams (see figures 3.2 and 3.11) can be combined by treating the LQ as an off-shell particle. This gives the two Feynman diagrams shown in figure 3.32. In addition to this we also need to include

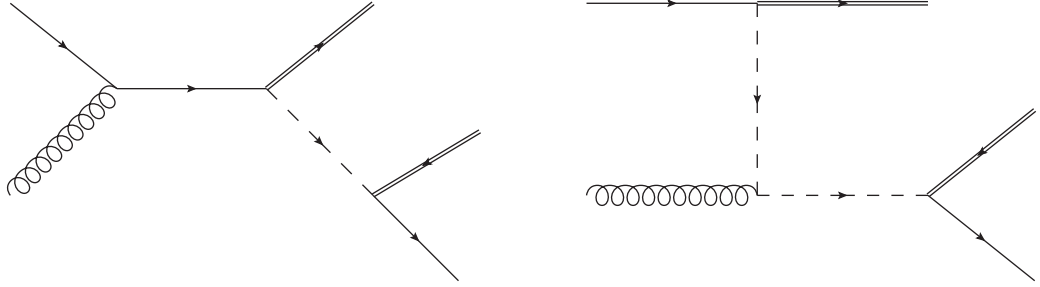


**Figure 3.32:** *The factorisable LO contributions to the LQ production process.*

one non-factorisable LO contribution - as shown in figure 3.33. This additional con-

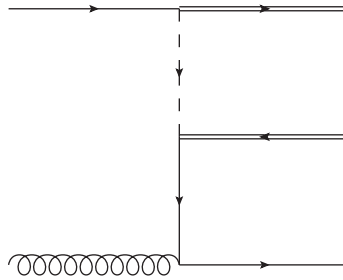


**Figure 3.33:** *The non-factorisable LO contribution to the LQ production process.*

tribution cannot be factorised into a LQ production and decay process and makes a non-resonant contribution to the final result. This non-factorisable diagram also suffers from an initial state singularity - when the outgoing quark becomes collinear with the incoming gluon. As with the additional NLO contributions this infrared divergence is dealt with using the dipole subtraction method implemented in a similar way as discussed in section 3.2.8.

The purpose of calculating the full non-factorisable process at NLO is to make a comparison with the NWA and determine how good the NWA is at approximating the full process at NLO. From the NWA results it is clear that the largest contributions come from the QCD and LQ corrections and so the EW corrections will be neglected when calculating the full non-factorisable process.

To determine the factorisable contributions at NLO the virtual QCD and LQ corrections to the production process need to be combined with the decay tree-level amplitude (treating the LQ as off-shell) and likewise the production tree-level amplitudes need to be combined with the virtual QCD corrections to the decay process.

As an example, combining the virtual QCD production topology  $B_1$  and the decay tree gives the factorisable topology shown in figure 3.34. The remaining factorisable topologies can be combined in the same way.

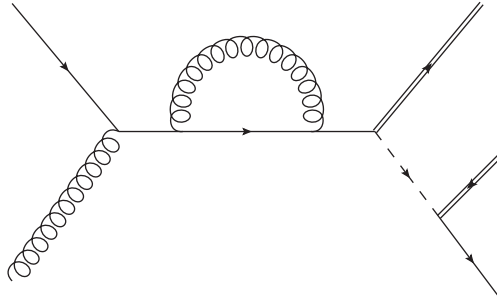


**Figure 3.34:** *An example factorisable NLO contribution to the LQ production process.*

### 3.3.1 Non-Factorisable Virtual Contributions

Having constructed the factorisable contributions the remaining non-factorisable diagrams need to be determined. These non-factorisable virtual corrections can be grouped into four different topologies. These are the familiar bubble, triangle and box diagrams, but now there are also pentagon diagrams (i.e. loops with five vertices). The new topologies for the QCD corrections are shown in figures 3.35 to 3.38 and the new topologies for the LQ corrections are shown in figure 3.39.

These non-factorisable diagrams are also calculated using the helicity projection

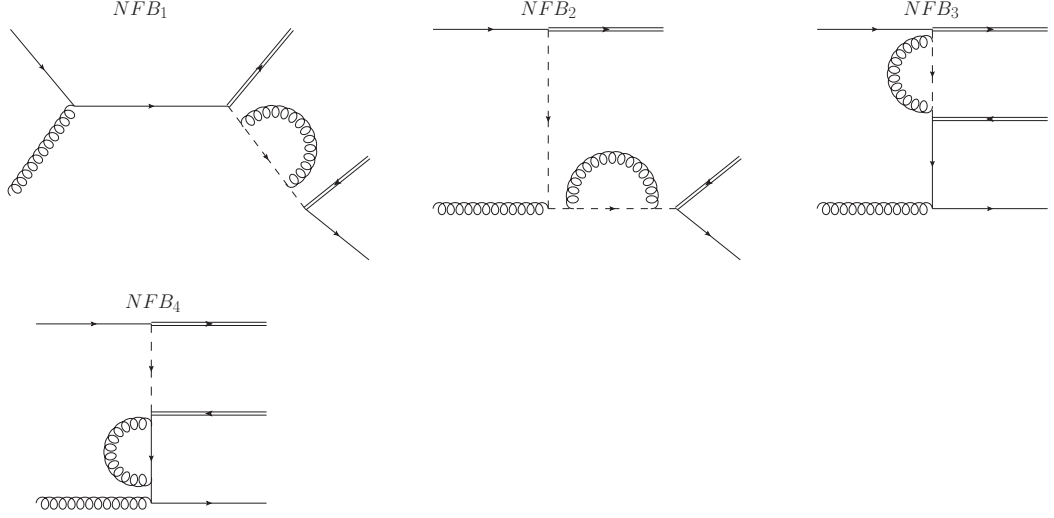


**Figure 3.35:** Non-factorisable QCD bubble graphs.

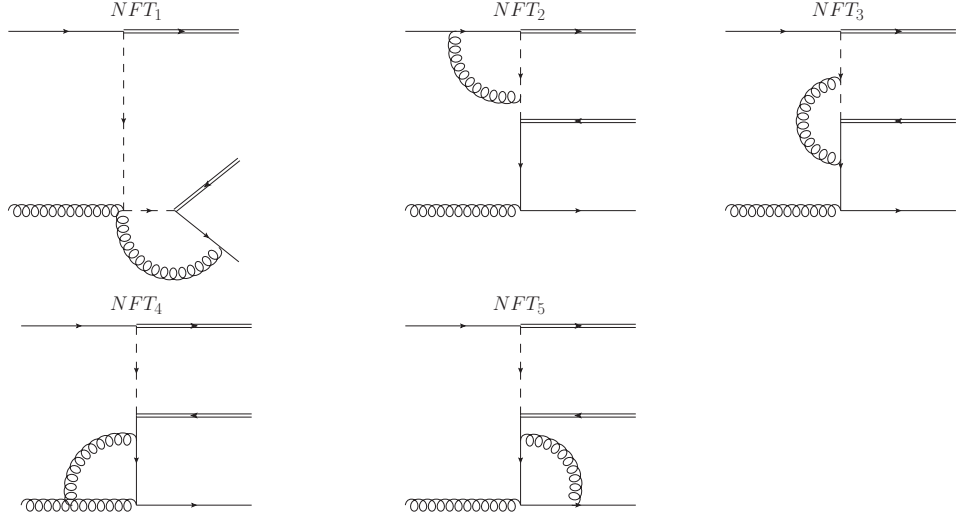


**Figure 3.36:** Non-factorisable QCD triangle graphs.

technique (see appendix A). For the full non-factorisable process the procedure for including the external leg corrections and preparing the calculations for SAMURAI is the same as discussed in section 3.2.

### 3.3.2 Instabilities in the Non-Factorisable Virtual Corrections

It was found that some of the non-factorising graphs suffered from instabilities around the resonant region of phase-space and was caused by two different problems.

The first problem comes from topologies  $NFB_1$  and  $NFB_2$  as well as  $NFLQB_1$  and  $NFLQB_2$ . Labelling the momentum of the outgoing anti-lepton and quark as

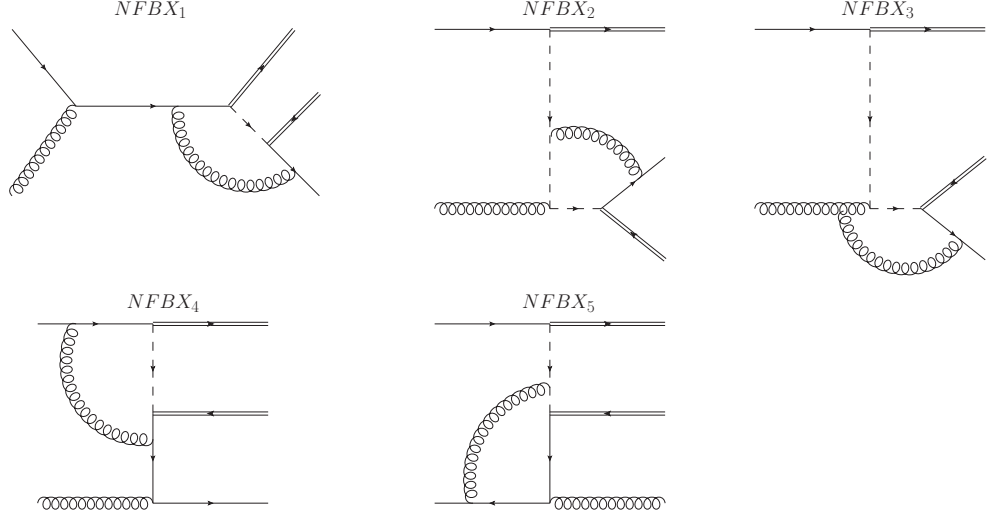


**Figure 3.37:** Non-factorisable QCD box graphs.

*Note: These graphs illustrate the different topologies, but do not show the in and out states in a consistent way.*

$q_2$  and  $q_3$  respectively, these diagrams become divergent when  $(q_2 + q_3)^2 \rightarrow m_{\text{LQ}}^2$ . This is because of the  $\frac{1}{(q_2 + q_3)^2 - m_{\text{LQ}}^2}$  propagator terms in the diagrams. By making the substitution

$$\begin{array}{c} \text{---} \text{---} \text{---} \text{---} \end{array} \xrightarrow{\frac{i}{p^2 - m_{\text{LQ}}^2 - \Sigma_R(p^2) + im_{\text{LQ}}\Gamma}} \quad (3.48)$$

for the 1-loop propagators in  $NFB_1$  and  $NFB_2$  the instability in these two diagrams is removed. In eq.(3.48)  $p^2 = (q_2 + q_3)^2$  and  $\Sigma_R(p^2) = \Sigma(p^2) - \Sigma(m_{\text{LQ}})$  is the mass renormalised 1-loop propagator with

$$-i\Sigma(p^2) = \begin{array}{c} \text{---} \text{---} \text{---} \text{---} \end{array} \quad (3.49)$$

In a similar manner the instabilities in  $NFLQB_1$  and  $NFLQB_2$  are removed by making the following substitution for the 1-loop propagators

$$\begin{array}{c} \text{---} \text{---} \text{---} \end{array} \xrightarrow{\frac{i}{p^2 - m_{\text{LQ}}^2 - \Sigma_R(p^2) + im_{\text{LQ}}\Gamma}} \quad (3.50)$$

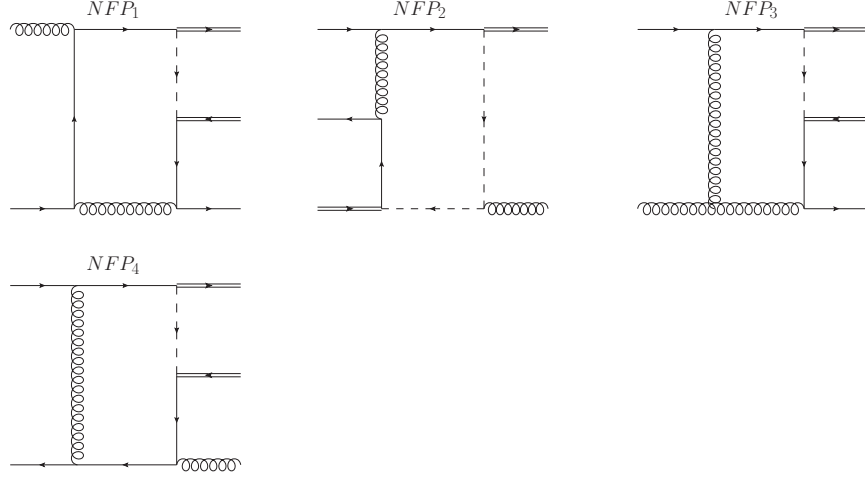


**Figure 3.38:** *Non-factorisable QCD pentagon graphs.*  
*Note: These graphs illustrate the different topologies, but do not show the in and out states in a consistent way.*

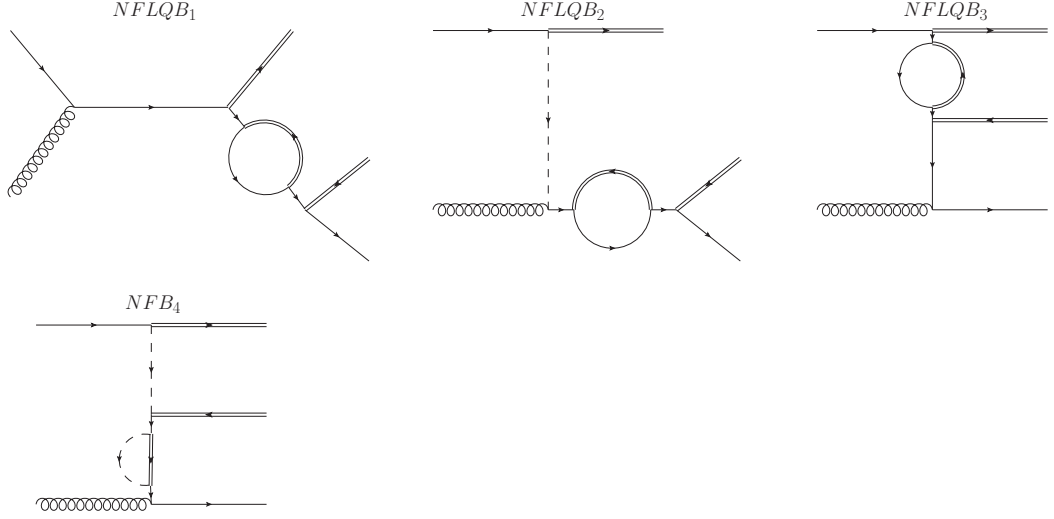


**Figure 3.39:** *Non-factorisable LQ bubble graphs.*

where

$$-i\Sigma(p^2) = \text{diagram of a bubble loop with two external lines} \quad (3.51)$$

Further details about this calculation are given in appendix B.

The second problem comes from topologies  $NFT_1$ ,  $NFBX_1 - NFBX_3$  and  $NFP_1 - NFP_3$ . Within SAMURAI these topologies also become unstable when  $(q_2 + q_3)^2 \rightarrow m_{LQ}^2$  and is because SAMURAI does not include a decay-width in the LQ loop propagators. To remedy this the unstable amplitudes  $\mathcal{A}_{\text{unstable}}$  were changed

to

$$\mathcal{A}_{\text{unstable}} \rightarrow \mathcal{A}_{\text{unstable}} \times \frac{(q_2 + q_3)^2 - m_{\text{LQ}}^2}{(q_2 + q_3)^2 - m_{\text{LQ}}^2 + im_{\text{LQ}}\Gamma} \quad (3.52)$$

Away from the unstable region  $\frac{(q_2+q_3)^2-m_{\text{LQ}}^2}{(q_2+q_3)^2-m_{\text{LQ}}^2+im_{\text{LQ}}\Gamma} \approx 1$  and near the unstable region this “fix” effectively simulates a decay-width for the LQ propagators inside the loops, thereby removing the instability.

Despite implementing the above fixes the graphs  $NFBX_3$  and  $NFP_3$  were still found to be suffering from numerical instabilities. Within FORTRAN the numerical precision of SAMURAI was increased from double to quadruple precision, however this did not resolve the problem. The details and resolution to this problem will be discussed further in section 3.3.6.

### 3.3.3 Non-Factorisable Bremsstrahlung Corrections

As with the factorisable virtual diagrams, the factorisable bremsstrahlung diagrams can be obtained by combining the production bremsstrahlung graphs with the decay tree-level graph and combining the production tree-level graphs with the decay bremsstrahlung graphs. In addition to this there are also non-factorisable interferences which need to be considered, these are shown in figure 3.40.

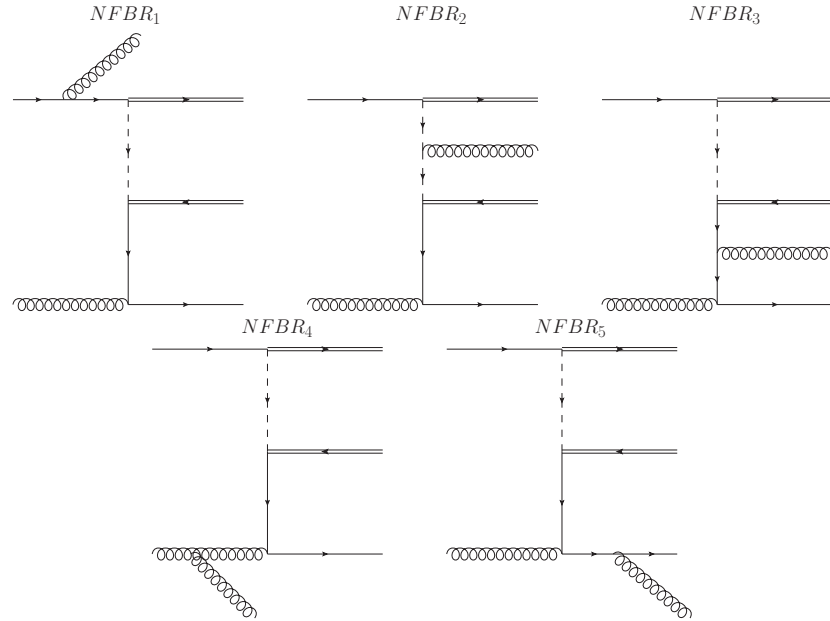


**Figure 3.40:** Non-factorisable QCD bremsstrahlung graphs.

Dealing with the the infrared divergences for the full non-factorisable process is simpler than in the NWA. This is because the production and decay are no longer treated as independent processes which need to have their divergences dealt with separately.

The infrared divergences can be entirely dealt with using the dipole subtraction method and follows the same procedure as discussed in section 3.2.5. For the dipole subtraction terms there are only three emitter-spectator pairs: for the incoming quark & gluon and the outgoing quark. The insertion terms are calculated in a similar way as before - where again there is the need to deal with two partons in the initial state.

### 3.3.4 Calculating the Cross-Section

The expression for the final cross-section is also simpler than in the NWA. Using the same notation as in section 3.2.7 the total cross-section is

$$\begin{aligned}
\sigma_{\text{NLO}} = & \underbrace{\frac{1}{2s} \int d^3_{\text{LIPS}} |\mathcal{A}_{\text{tree}}|^2}_{\sigma_{\text{tree}}} + \sum_{\{\text{QCD,LQ}\}} \underbrace{\frac{1}{2s} \int d^3_{\text{LIPS}} |\mathcal{A}_{1\text{-loop}}|^2 + I \otimes |\mathcal{A}_{\text{tree}}|^2}_{\sigma_{1\text{-loop}}} \\
& + \underbrace{\frac{1}{2s} \int d^4_{\text{LIPS}} |\mathcal{A}_{\text{brem}}|^2 - D \otimes |\mathcal{A}_{\text{tree}}|^2}_{\sigma_{\text{brem}}} \\
& + \underbrace{\frac{1}{2s} \int_0^1 dx \int d^3_{\text{LIPS}}(x) (P + K) \otimes (|\mathcal{A}_{\text{tree}}|^2)}_{\sigma_{\text{A-P}}} \quad (3.53)
\end{aligned}$$

where  $I \otimes |\mathcal{A}_{\text{tree}}|^2$  and  $D \otimes |\mathcal{A}_{\text{tree}}|^2$  are the dipole insertions and subtractions respectively and  $\sigma_{\text{A-P}}$  are the Altarelli-Parisi splitting functions due to the initial-state singularities. The expression shown in eq.(3.53) shows the parton-level cross-section, to get the physical cross-section this expression needs to be folded with the PDFs as described in section 3.2.7.

All of the phase-space integrals in this project are done using a VEGAS Monte-Carlo integrater and, for the full non-factorisable process, the differential cross-section w.r.t to the invariant mass of the anti-lepton/jet system is calculated during this integration routine. For the 3-body final states there is only one jet, however for the



4-body final state there are two jets. In most cases it is not physically possible to distinguish between different jets and so for the 4-body final state the invariant mass of the anti-lepton/jet system is calculated by including both jets.

### 3.3.5 Additional Contributions to the Full Process

As in the NWA, there are additional NLO contributions to be included with the full process. These include the same quark+quark, quark+anti-quark and gluon+gluon initial states discussed in section 3.2.8, but now also include the non-factorisable topologies.

There is also the additional contribution coming from  $\bar{u}$ -quark+gluon initial state. This process has the same topology as the primary  $u$ -quark+gluon process, but with the fermion lines reversed. This means the previous calculations can be reused, but the now the jet/anti-lepton invariant mass distribution will make a non-resonant contribution to the final result.

When considering the non-factorisable process there is also an additional LO contribution which needs to be included - this process is shown in figure 3.41. Being

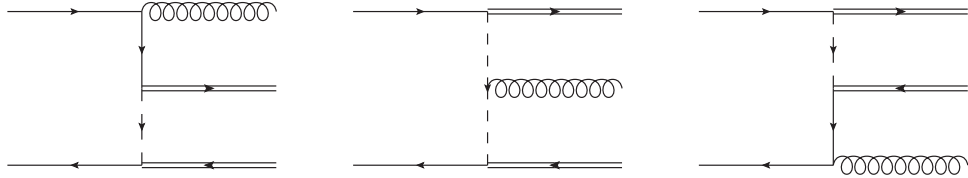


**Figure 3.41:** *The additional LO process:  $u + \bar{u} \rightarrow e^+ + e^- + g$ .*

LO the correct procedure, when studying the full non-factorising process, would be to include the NLO corrections for this additional LO process as well. Since this process is a non-resonant channel for LQ production it only makes a small contribution compared to the resonant LO process (see section 3.3.6). To a good approximation we are safe to only include this process at LO since the NLO corrections would be even smaller.

### 3.3.6 Results for the Full Process

In this section we present the results for the NLO QCD corrections to the full non-factorisable LQ production process. As before these were produced using two different PDF sets: CTEQ6M and CTEQ6L. The range for the invariant mass distribution  $m_{\text{inv}}$  is  $0 < m_{\text{inv}} < 2m_{\text{LQ}}$ .

To ensure the validity of the results these calculations have been checked using the Ward-Takahashi identity (see section 3.2.9) to ensure they are gauge invariant.

Considering first the CTEQ6M results, figure 3.22 shows the LO contribution to the process.<sup>7</sup> In common with the NWA result the main feature in the distribution is the resonance with a peak near  $m_{\text{LQ}} = 750 \text{ GeV}$ . This has a peak height of  $8.61 \times 10^{-3} \text{ pb/GeV}$  which is very close to the NWA result. The key difference between the new result and the NWA result is that the distribution is no longer symmetric around the peak and we see that the non-factorisable contributions give an enhancement to the distribution for values of the invariant mass  $m_{\text{inv}} < m_{\text{LQ}}$ . The total cross-section at LO is 1.08 pb in comparison to the NWA the total cross-section is larger. This is due to the enhancement to the distribution away from the resonance.

The similarities in the results between the NWA and full non-factorisable process are due to the resonant behaviour of both sets of calculations and the reason for the differences come from non-factorisable contributions which are not included in the NWA.

The NLO contributions can be split into QCD and LQ corrections. The results for the QCD corrections are shown in figure 3.23 and give a similar distribution to the LO results, with an enhancement to the resonant peak. The peak height is increased by 51% to  $1.30 \times 10^{-2} \text{ pb/GeV}$  and comparing this with the NWA peak the peaks are again very close. For the QCD corrections the total cross-section is 1.56 pb which again is larger than the cross-section in the NWA and gives an enhancement over the LO cross-section of 44%.

---

<sup>7</sup>Note: The LO contribution does not include the additional LO contribution as shown in figure 3.41. The results for this are shown separately in figure 3.42.

The results for the LQ corrections are shown in figure 3.25 and also give a similar distribution to the LO results, but with a reduction to the resonant peak. The peak height is decreased by 25% to  $6.43 \times 10^{-3}$  pb/GeV and again is very close to the NWA peak height. The total cross-section is 0.87 pb, which is larger than the cross-section in the NWA, and gives a reduction over the LO cross-section of 19%.

The results for the additional LO process (as shown in figure 3.41) are given in figure 3.42. Being a non-resonant process there is no resonant peak and the largest contribution is at low  $m_{\text{inv}}$ . The total cross-section for the additional LO process is 0.41 pb and is much smaller than the cross-section for the resonant LO result. This validates the decision to only include this process at LO.

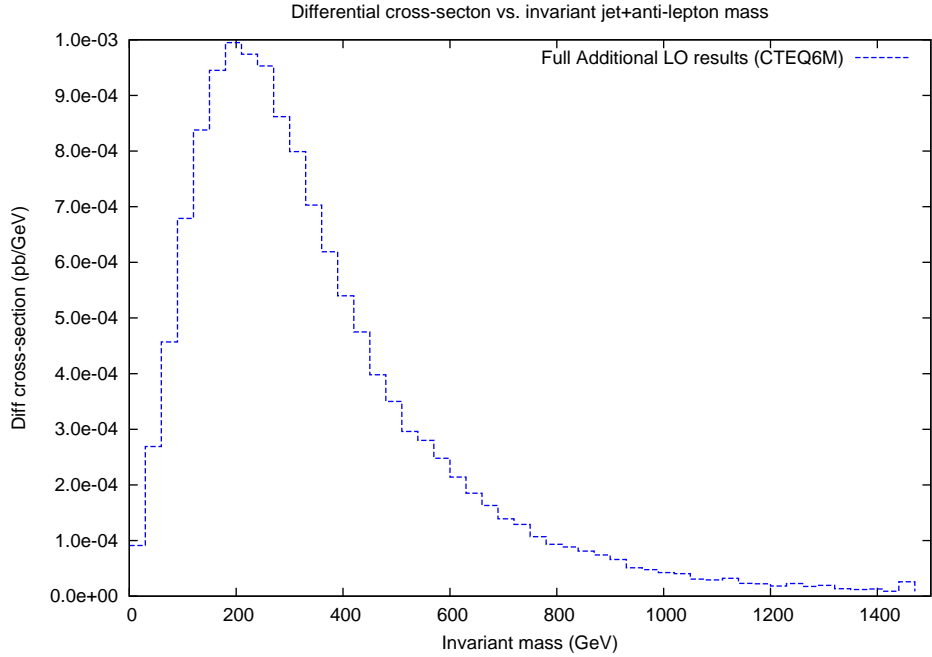


**Figure 3.42:** *Additional LO results for producing a scalar LQ in the full non-factorisable process (CTEQ6M).*

The additional NLO results (which include the contribution from the additional LO process) are shown in figure 3.29. This also gives a similar distribution to the LO result, but in addition to an enhancement to the resonant peak there is also a further enhancement in the region  $m_{\text{inv}} < m_{\text{LQ}}$ . The resonant peak has a height

of  $1.08 \times 10^{-2}$  pb/GeV giving an enhancement over the LO result of 25%. Again comparing the peak height with the peak in the NWA the peak heights are close. The total cross-section with the additional NLO results is 1.80 pb this is a lot larger than the cross-section from NWA and in part is due to the contribution from the additional LO process.

Combining the results gives the total NLO contribution to the non-factorising LQ process and is shown in figure 3.30. The height of the resonant peak is  $1.31 \times 10^{-2}$  which gives an enhancement of 52% compared to the LO peak there is also a further enhancement in the region  $m_{\text{inv}} < m_{\text{LQ}}$  which is primarily due to the additional NLO contributions. The cross-section for the total NLO result is 2.08 pb which is an increase of 93% over the LO result. For comparison, the LO and total NLO contributions are shown in figure 3.43.

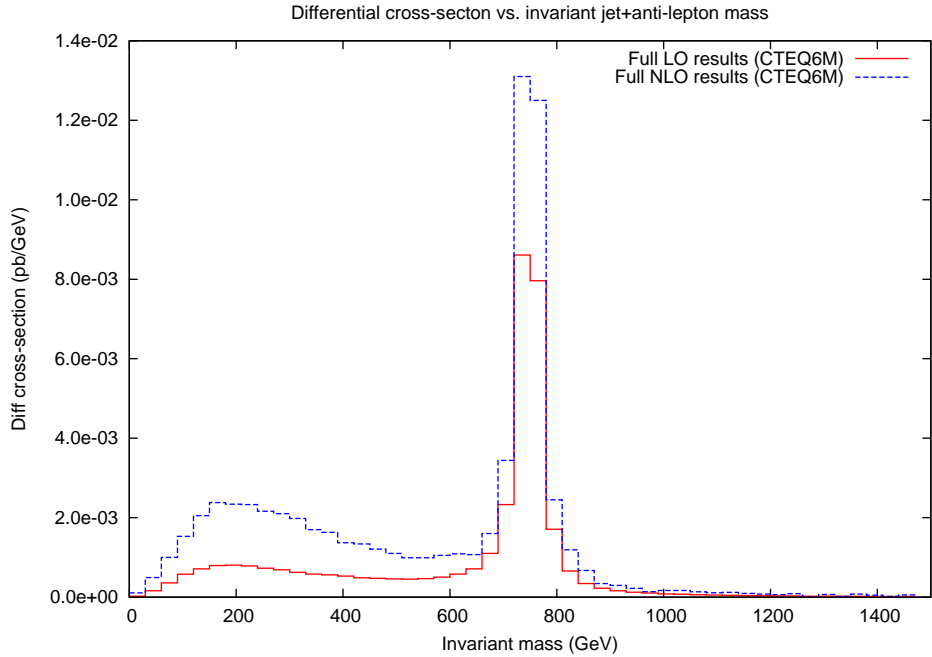


**Figure 3.43:** A comparison between the LO and NLO contributions for producing a scalar LQ in the non-factorisable process (CTEQ6M).

A summary of these results is shown in tables 3.9 and 3.10.

The parton level-results were also folded with the CTEQ6L PDF set giving a

Correction Type	Peak Height (pb/GeV)	Percentage change on LO
Tree	$8.61 \times 10^{-3}$	-
QCD	$1.30 \times 10^{-2}$	+51%
LQ	$6.43 \times 10^{-3}$	-25%
Additional	$1.08 \times 10^{-2}$	+25%
Total	$1.31 \times 10^{-2}$	+52%

**Table 3.9:** Summary of the CTEQ6M scalar results for the non-factorisable process.

Correction Type	Total cross-section (pb)	Percentage change on LO
Tree	1.08	-
QCD	1.56	+44%
LQ	0.87	-19%
Additional	1.80	+67%
Total	2.08	+93%

**Table 3.10:** Summary of the CTEQ6M scalar results for the non-factorisable process.

very similar distributions to the CTEQ6M results (see figure 3.44). The results are summarised in tables 3.11 and 3.12.

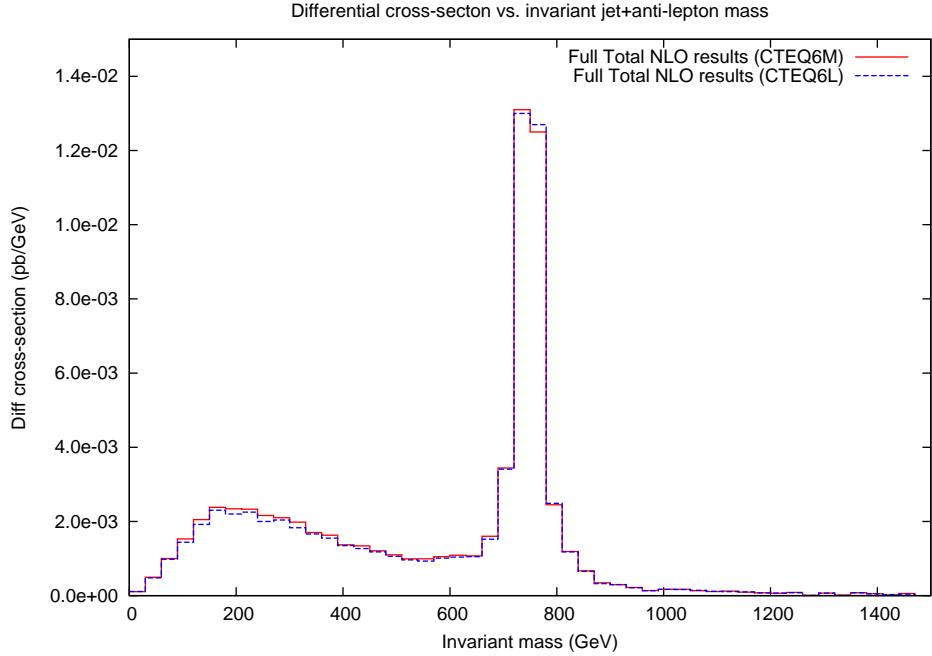


**Figure 3.44:** Total NLO results for producing a scalar LQ in the full non-factorisable process - comparing the CTEQ6M and CTEQ6L PDF sets.

Correction Type	Peak Height (pb/GeV)	Percentage change on LO
Tree	$8.54 \times 10^{-3}$	-
QCD	$1.30 \times 10^{-2}$	+52%
LQ	$6.39 \times 10^{-3}$	-25%
Additional	$1.07 \times 10^{-2}$	+25%
Total	$1.30 \times 10^{-2}$	+52%

**Table 3.11:** *Summary of the CTEQ6L scalar results for the non-factorisable process.*

Correction Type	Total cross-section (pb)	Percentage change on LO
Tree	1.07	-
QCD	1.54	+44%
LQ	0.86	-20%
Additional	1.77	+65%
Total	2.03	+90%

**Table 3.12:** *Summary of the CTEQ6L scalar results for the non-factorisable process.*

### Dealing With the Remaining Instabilities

In producing the above results it was first necessary to fix the remaining instabilities in the SAMURAI calculations. These remaining instabilities were found in graphs  $NFBX_3$  and  $NFP_3$  and manifested as a sign flip at the resonant region in the distribution. When the invariant mass of the anti-lepton/jet system is close to on-shell there are instabilities in the solution which gives the cuts required to determine the coefficients of some of the standard scalar integrals. These coefficients become large but change sign when passing through the resonance. Isolating the contributions from these graphs the instability is shown in figure 3.45. To reduce the effect of this instability on the final distribution the value of the three bins either side of point where the resonance flips sign were averaged together thereby reducing the effect of the instability.

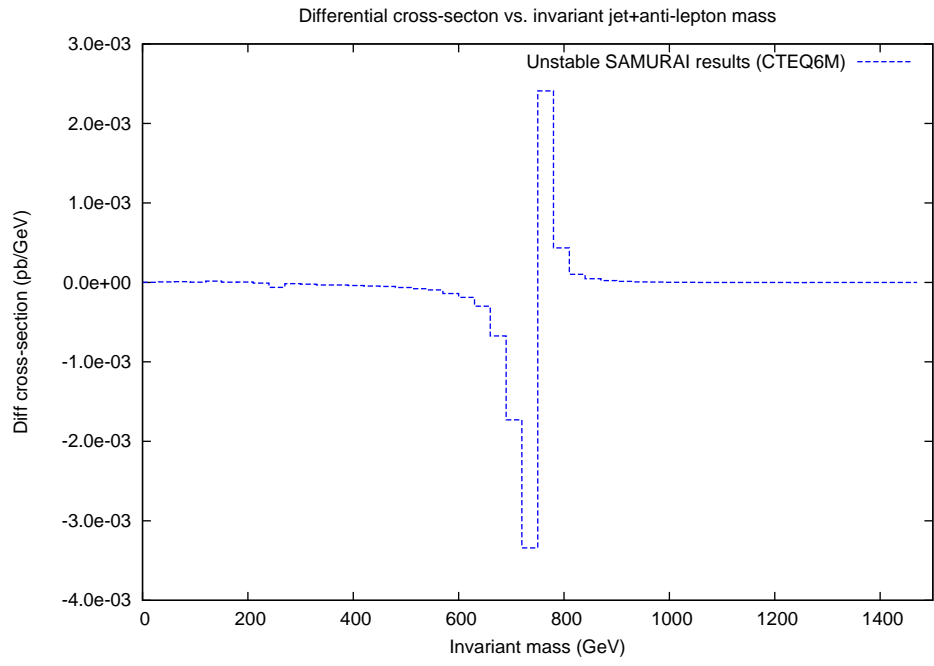


**Figure 3.45:** *The unstable contributions from graphs  $NFBX_3$  and  $NFP_3$ .*

## Chapter 4

# Vector leptoquarks

Having studied the effectiveness of the NWA for a scalar LQ, this chapter will continue the study for the case where the LQ is a vector. For the purpose of this chapter we will be looking at the vector LQ type  $U_1$  as described in [7], this type of LQ is an  $SU(2)$  singlet and has charge  $+2/3$ . The core process we will consider is  $d + g \rightarrow e^- + e^+ + d$  starting with the factorisable process  $d + g \rightarrow e^- + U_1 \rightarrow e^- + e^+ + d$ .

To calculate the results at the amplitude level the helicity projection technique will be used, but in the case of vector LQs the expressions involve an odd number of  $\gamma$  matrices. Details of projecting out an odd number of  $\gamma$  matrices are given in appendix A.

The  $U_1$  LQ couples in the same way as the  $R_2$  does to the other particles, this means that we can carry over wholesale all of the topologies which were used in the discussion on scalar LQs. The only fundamental difference being that the single fermion line now represents a d-quark and the scalar line for the  $R_2$  LQ should be replaced with a zigzag line representing a massive gauge boson. With this understood it is unnecessary to repeat the topologies detailed in chapter 3.

In terms of the Feynman diagrams the vector LQs do add one complication due to our choice of gauge: the Feynman gauge. In this gauge we need to include contributions from Goldstone bosons and Faddeev-Popov ghosts and this adds some complexity to some of the topologies we wish to re-use from chapter 3.



The coupling of the Goldstone bosons to the fermions is proportional to the fermion mass and since we are treating the fermions as massless these couplings can be ignored. This situation reduces the number diagrams which would otherwise need to include Goldstone contributions.

From the previous chapter it is clear that the QCD corrections dominate and so we restrict the analysis of this chapter to QCD corrections only.

## 4.1 Vector Leptoquarks in the NWA

Dealing with vector LQs in the NWA follows the same procedure as with the scalar LQs, the primary difference being that the NWA will now need to include a sum over helicities for the intermediate vector LQ.

### 4.1.1 Virtual Corrections

The topologies for the virtual QCD corrections to the LQ production amplitude (shown in figures 3.3 to 3.5) can be reused for the vector LQ as described above, as can the decay topology (shown in figure 3.12). The only topologies which need to be modified to include contributions from Goldstone bosons and Faddeev-Popov ghosts are  $B_1$ ,  $T_5$ ,  $T_6$  and  $BX_2$ .

The 1-loop QCD corrections to the LQ propagator includes Goldstone boson and Faddeev-Popov ghost corrections and so the topology  $B_1$  is modified as shown in figure 4.1 - where the contributions to the 1-loop propagator are shown in figure 4.2). This means the topology  $B_1$  is actually comprised of four separate diagrams.

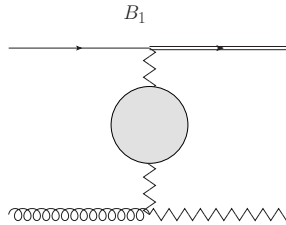


**Figure 4.1:** *The modified  $B_1$  topology for a vector LQ.*

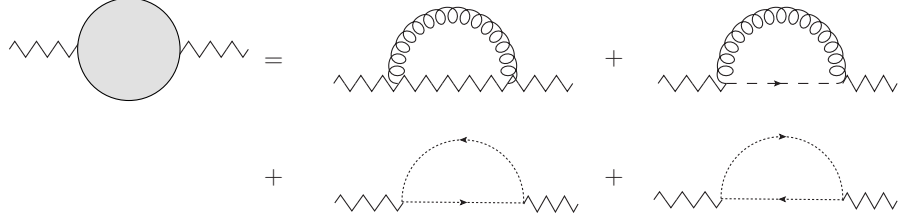


**Figure 4.2:** *QCD, Goldstone and Faddeev-Popov ghost corrections to the LQ propagator.*

Likewise the 1-loop corrections to the gluon-LQ triple-point vertex also contain Goldstone boson and ghost corrections. This also modifies the topologies as shown in figure 4.3 - where the contributions to the vertex corrections are shown in figure 4.4. Each of these topologies are now also comprised of four separate diagrams.

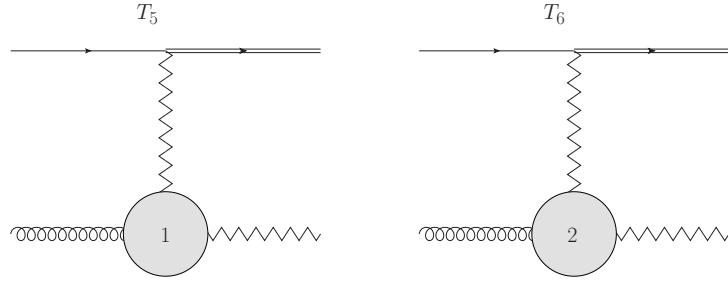


**Figure 4.3:** *The modified  $T_5$  and  $T_6$  topologies for a vector LQ.*

Finally  $BX_2$  has an additional Goldstone contribution and is now comprise of two diagrams (see figure 4.5).

Calculating the external leg corrections and preparing the calculations for SAMURAI follows the same procedure as in the scalar LQ case.

#### 4.1.2 Bremsstrahlung Corrections

The topologies for the bremsstrahlung corrections are the same as described in sections 3.2.5 and 3.2.6. For the production bremsstrahlung process the dipole subtraction method is used and as with the scalar LQ case the outgoing vector LQ is treated as a squark in the dipole formalism.

For the LQ decay process the infrared divergences are again handled analytically (i.e. in  $d = 4 - 2\epsilon$  dimensions), but now this must be done separately for each helicity of the decaying vector LQ. The reason for this is that in the NWA it is

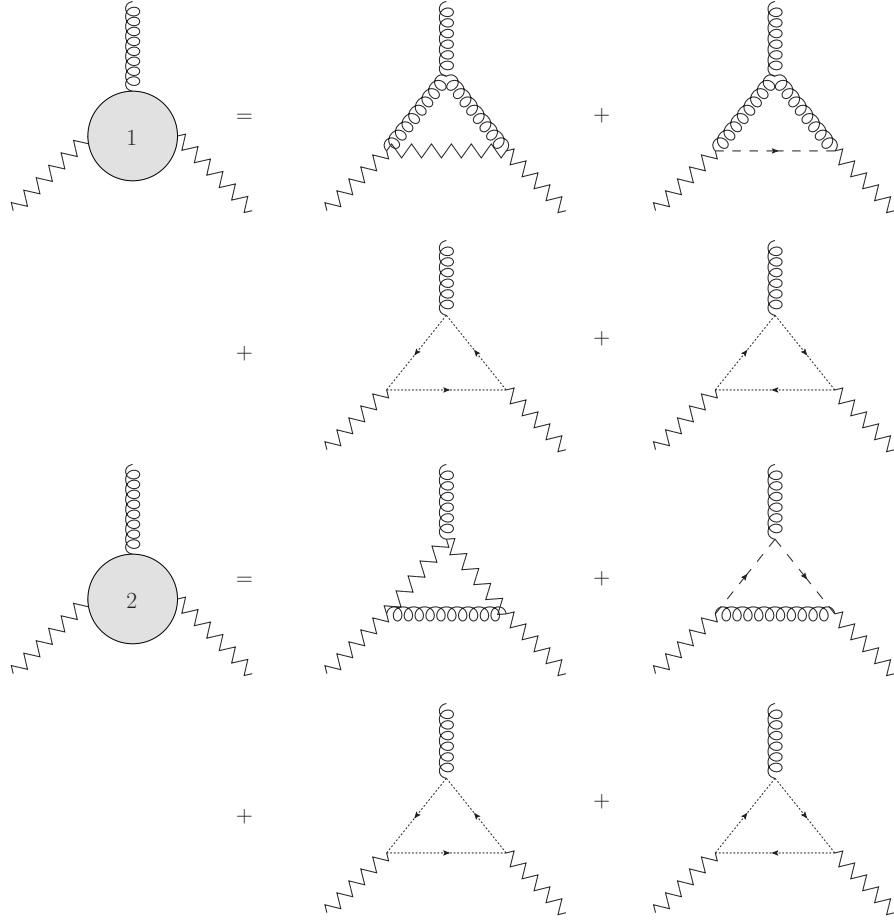


**Figure 4.4:** *QCD, Goldstone and Faddeev-Popov ghost corrections to the gluon-LQ triple-point vertex.*

necessary to sum over the helicities of the intermediate LQ. In the rest frame of the LQ the polarisation vectors for the different helicities are

$$\varepsilon_L = [0, 0, 0, 1]^T \quad (4.1)$$

$$\varepsilon_{\pm} = \frac{1}{\sqrt{2}}[0, 1, \pm i, 0]^T \quad (4.2)$$

where  $\varepsilon_L$  is the longitudinal polarisation state and  $\varepsilon_{\pm}$  are the transverse polarisation states. Using these polarisation states and the same parametrisation for the momenta as in section 3.2.6 the final results for the decay bremsstrahlung are

$$\Gamma_{\text{brem}} = \frac{1}{256\pi^3} g^2 g_{\text{LQ}}^2 m_{\text{LQ}} C_F \left( \frac{m_{\text{LQ}}^2}{\mu^2} \right)^{-\epsilon} \left[ \frac{4}{\epsilon^2} + \frac{14}{\epsilon} + \frac{1}{12} (530 - 8\pi^2) \right] \quad (4.3)$$

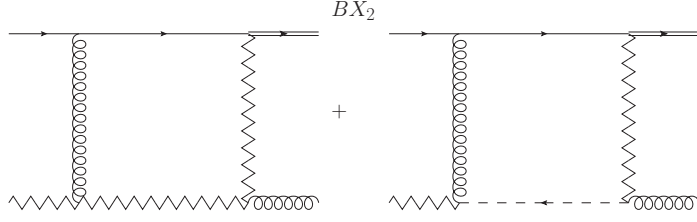


**Figure 4.5:** The modified  $BX_2$  topology for a vector  $LQ$ .

for the transverse polarisation states (i.e.  $\lambda = \pm 1$ ) and

$$\Gamma_{\text{brem}} = \frac{1}{256\pi^3} g^2 g_{LQ}^2 m_{LQ} C_F \left( \frac{m_{LQ}^2}{\mu^2} \right)^{-\epsilon} \left[ -\frac{1}{3\epsilon} + \frac{1}{9} (257 - 24\pi^2) \right] \quad (4.4)$$

for the longitudinal polarisation state (i.e.  $\lambda = 0$ ). As a check on the helicity dependence, when the calculations for the decay bremsstrahlung in eq.(4.3) and eq.(4.4) are combined with the virtual decay corrections and the helicities are summed over (as described in section 4.1.3) it has been confirmed that the infrared poles cancel.

#### 4.1.3 Combining the Production and Decay Process

The production and decay processes are combined as in section 3.2.7, however the production cross-sections and decay-widths are now functions of the LQ helicity  $\lambda$  and in the final result there is a sum over  $\lambda$ . The final result for the vector LQ in the NWA is

$$\begin{aligned} \sigma_{\text{NLO}} \approx \sum_{\lambda=\{-1,0,1\}} \frac{m_{LQ}}{\pi} \int_0^s dp^2 \frac{1}{(p^2 - m_{LQ}^2)^2 + m_{LQ}^2 (\Gamma^{\text{tot}})^2} & \left[ \sigma_{\text{tree}}(\lambda) \times \Gamma_{\text{tree}}(\lambda) \right. \\ & + \sigma_{\text{tree}}(\lambda) \times \Gamma_{1\text{-loop}}(\lambda) + \sigma_{1\text{-loop}}(\lambda) \times \Gamma_{\text{tree}}(\lambda) \\ & \left. + \sigma_{\text{tree}}(\lambda) \times \Gamma_{\text{brem}}(\lambda) + \sigma_{\text{brem}}(\lambda) \times \Gamma_{\text{tree}}(\lambda) + \sigma_{\text{A-P}}(\lambda) \times \Gamma_{\text{tree}}(\lambda) \right] \end{aligned} \quad (4.5)$$

with  $\sigma_{\text{tree}}$ ,  $\sigma_{1\text{-loop}}$  etc. defined as in section 3.2.7, but now as functions of  $\lambda$ .

For the  $U_1$  vector LQ there are two decay channels for the LQ ( $U_1 \rightarrow d + e^+$

and  $U_1 \rightarrow u + \bar{\nu}_e$ ) giving the total decay-width  $\Gamma^{\text{tot}}$  as

$$\Gamma^{\text{tot}} = \frac{1}{24\pi} [2h_{1L}^2 + h_{1R}^2] m_{\text{LQ}} = 34.20 \text{ GeV} \quad (4.6)$$

and since  $m_{\text{LQ}} = 750 \text{ GeV}$  this confirms the validity of the NWA.

#### 4.1.4 Additional NLO Contributions

For the vector LQ the same additional factorisable NLO contributions as shown in figure 3.20 are also needed. As before some of the diagrams will suffer from initial-state singularities and these are also dealt with using the dipole subtraction method as in the case with the scalar LQs.

#### 4.1.5 Results in the NWA

As with the previous results the invariant anti-lepton/jet mass range is  $0 < m_{\text{inv}} < 2m_{\text{LQ}}$ . The results were again folded with two different PDF sets: CTEQ6M and CTEQ6L.

The NWA result for the vector LQ show the same features as were seen with the scalar LQ. The invariant mass distribution is symmetrical with a resonant peak at  $m_{\text{LQ}} = 750 \text{ GeV}$ .

Starting with the CTEQ6M folded results, the LO result (see figure 4.6) has a resonant peak height of  $3.79 \times 10^{-2} \text{ pb/GeV}$  and comparing this with the NLO result (see figure 4.7) the peak height has increased to  $5.52 \times 10^{-2} \text{ pb/GeV}$  giving an enhancement of 46% over the LO result. There is also an increase in the total cross-section from 3.30 pb to 4.73 pb giving an enhancement of 43%.

The additional NLO results (see figure 4.8) also show a large enhancement to the resonant peak. These corrections have a resonant peak height of  $5.71 \times 10^{-2} \text{ pb/GeV}$  giving an enhancement of 51% over the LO result. There is also a large enhancement to the cross-section which is increased by 53% to 5.04 pb.

Combining these corrections, the total NLO result (see figure 4.9) has a peak

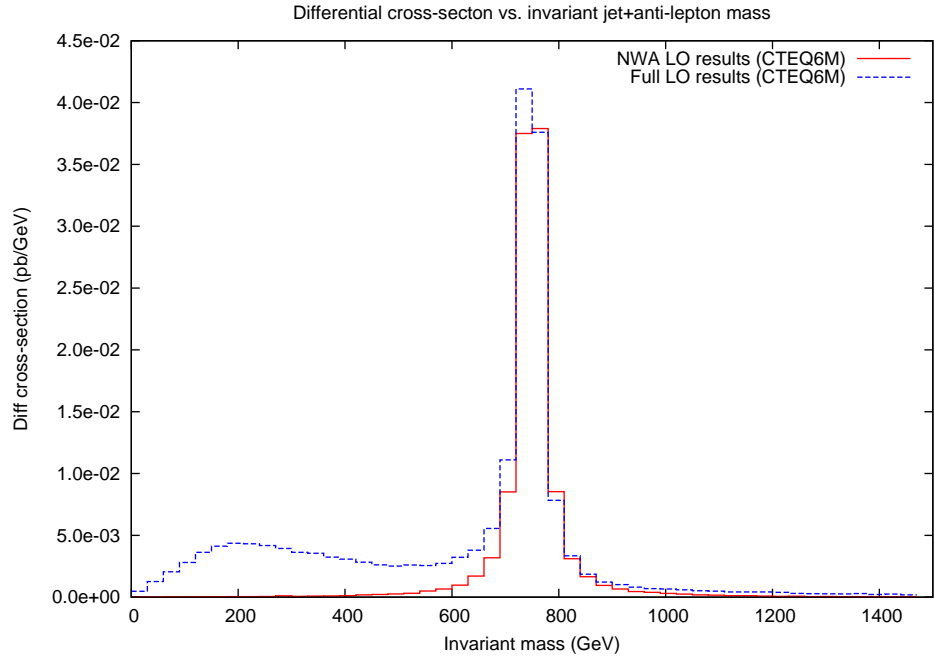


**Figure 4.6:** *LO results for producing a vector  $LQ$  - comparing the NWA to the full non-factorisable process (CTEQ6M).*

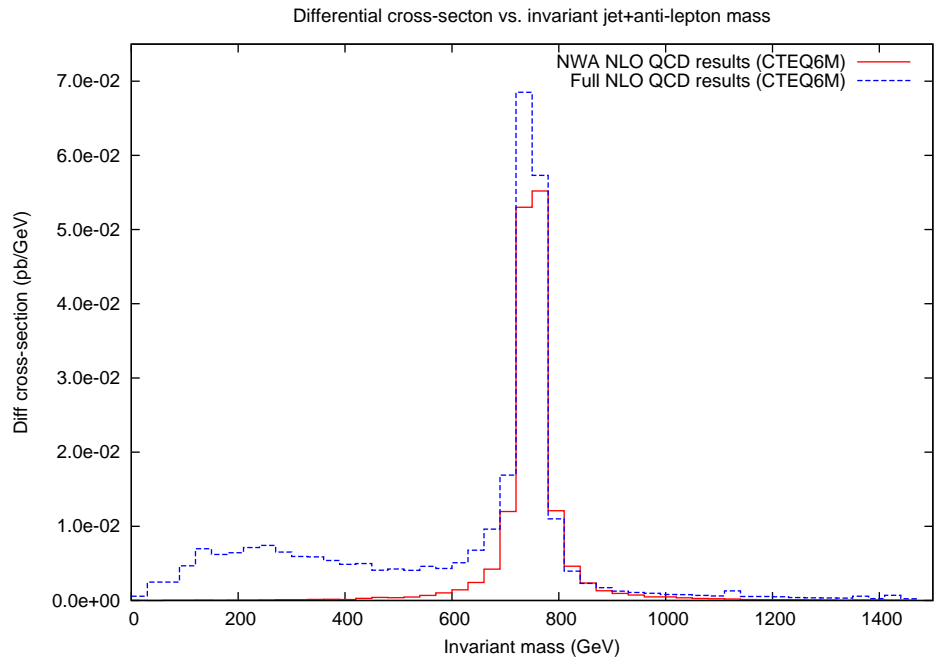


**Figure 4.7:** *NLO results for producing a vector  $LQ$  - comparing the NWA to the full non-factorisable process (CTEQ6M).*

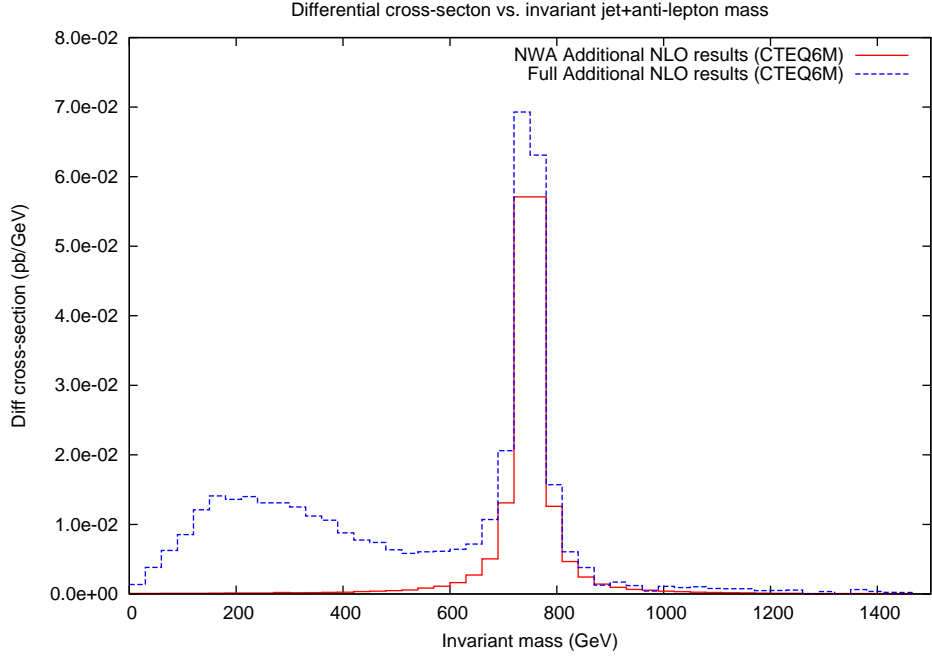


**Figure 4.8:** Additional NLO results for producing a vector  $LQ$  - comparing the NWA to the full non-factorisable process (CTEQ6M).

height of  $7.44 \times 10^{-2}$  pb/GeV giving a large enhancement of 96% over the LO result. The cross-section for total NLO process is increased by 96% to 6.47 pb.

To make a comparison between the LO and total NLO contributions these are combined and shown in figure figure 4.10.

A summary of the results for the CTEQ6M folding are shown in tables 4.1 and 4.2.

Correction Type	Peak Height (pb/GeV)	Percentage change on LO
Tree	$3.79 \times 10^{-2}$	-
QCD	$5.52 \times 10^{-2}$	+46%
Additional	$5.71 \times 10^{-2}$	+51%
Total	$7.44 \times 10^{-2}$	+96%

**Table 4.1:** Summary of the CTEQ6M vector results for the NWA.

The CTEQ6L folding produced comparable results to the CTEQ6M folding and only the total NLO results are shown (see figure 4.11). It is observed, however, that there is a slight decrease in the peak heights and cross-sections when folding with

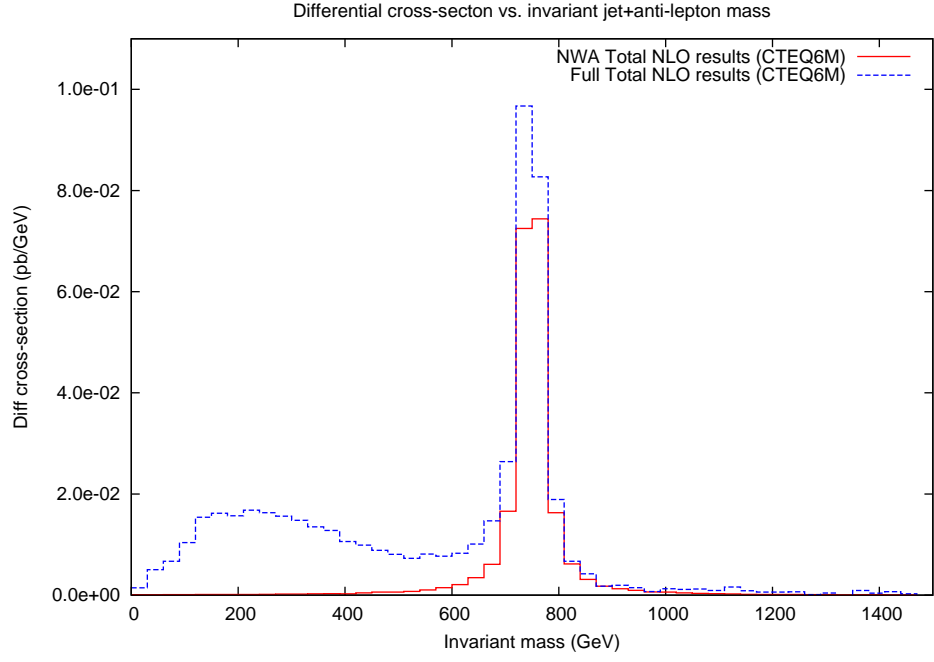


**Figure 4.9:** Total NLO results for producing a vector  $LQ$  - comparing the NWA to the full non-factorisable process (CTEQ6M).

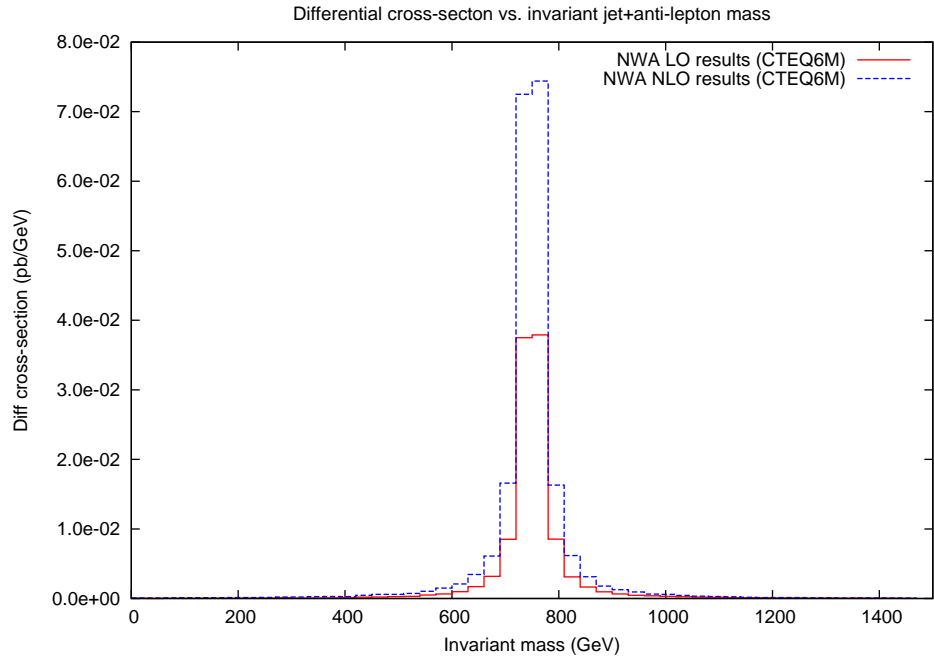


**Figure 4.10:** A comparison between the LO and NLO contributions for producing a vector  $LQ$  in the NWA (CTEQ6M).



Correction Type	Total cross-section (pb)	Percentage change on LO
Tree	3.30	-
QCD	4.73	+43%
Additional	5.04	+53%
Total	6.47	+96%

**Table 4.2:** Summary of the CTEQ6M vector results for the NWA.

CTEQ6L. A summary of the results for the CTEQ6L folding are shown in tables 4.3 and 4.4.

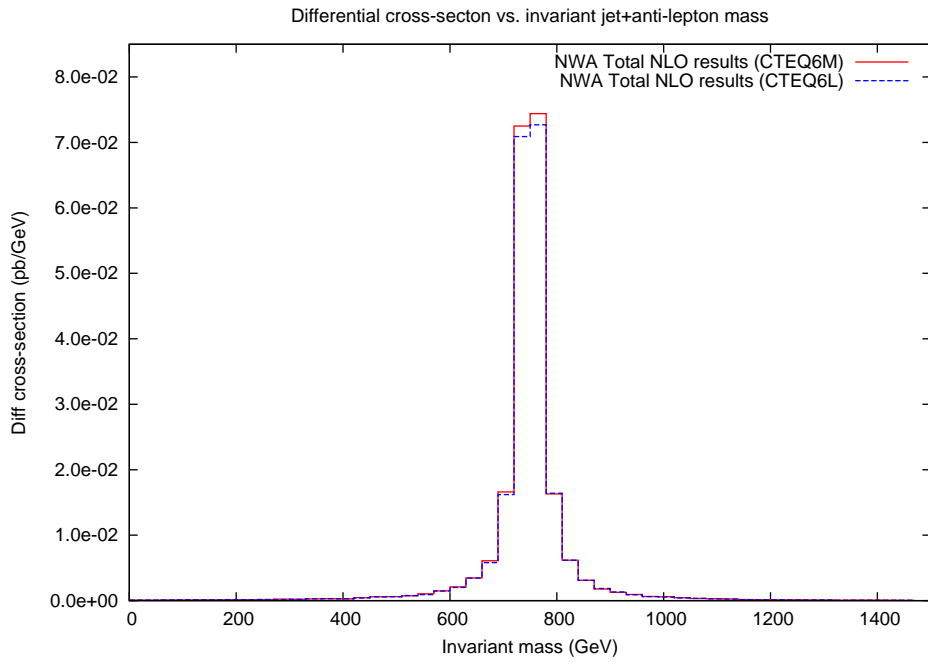


**Figure 4.11:** Total NLO results for producing a vector  $LQ$  in the NWA comparing the CTEQ6M and CTEQ6L PDF sets.

Correction Type	Peak Height (pb/GeV)	Percentage change on LO
Tree	$3.70 \times 10^{-2}$	-
QCD	$5.37 \times 10^{-2}$	+45%
Additional	$5.60 \times 10^{-2}$	+51%
Total	$7.27 \times 10^{-2}$	+96%

**Table 4.3:** Summary of the CTEQ6L vector results for the NWA.

Correction Type	Total cross-section (pb)	Percentage change on LO
Tree	3.23	-
QCD	4.61	+43%
Additional	4.95	+53%
Total	6.34	+96%

**Table 4.4:** *Summary of the CTEQ6L vector results for the NWA.*

## 4.2 Vector Leptoquarks: The Full Non-Factorisable Process

Again the full non-factorisable process for the vector LQs follows the same procedure as for the scalar LQs. All of the production and decay topologies from the NWA can be combined as discussed in section 3.3 and only the non-factorisable contributions need to be determined.

### 4.2.1 Non-Factorisable Contributions

The non factorisable virtual corrections have the same topologies as those shown in figures 3.35 to 3.38. Unlike the factorisable graphs there are no additional contributions with Goldstone bosons and Faddeev-Popov ghost and so the topologies for the scalar LQ can be reused - with the scalar LQ replaced with a vector LQ.

The non-factorisable virtual corrections for the vector LQ also suffered from the same instabilities as discussed in section 3.3.2 and these were dealt with following the same procedures as before.

The same situation follows for the bremsstrahlung contributions, these contributions along with the implementation of the dipole subtraction method are dealt with in the same way as discussed in section 3.3.3.

The final cross-section for the full non-factorisable process has the same form as shown in eq.(3.53).

### 4.2.2 Additional Contributions to the Full Process

As with the scalar case there are three groups of additional contributions to the full process. These are the quark+quark, quark+anti-quark and gluon+gluon initial states. There is also the non-resonant  $\bar{d}$ +gluon initial state which is calculated based on the main non-factorisable diagrams, but with the fermion lines reversed. Finally there is additional LO process  $d + \bar{d} \rightarrow e^- + e^+ + g$  with the same topology as in figure 3.41 and, for the same reasons as discussed in section 3.3.5, is only included at LO.

### 4.2.3 Results for the Full Process

Using the same invariant anti-lepton/jet mass range as before the CTEQ6M and CTEQ6L folded results for the full non-factorisable process are presented here.

Starting with the CTEQ6M results the LO contribution (shown in figure 4.6) shows the same resonant peak at  $m_{LQ} = 750$  GeV as in the NWA, but compared with the scalar LQ results there is now a noticeable difference between the peak heights for the NWA and full process. The NWA has a peak height of  $3.79 \times 10^{-2}$  pb/GeV whereas the full process has a peak height of  $4.11 \times 10^{-2}$  pb/GeV which is an increase of 8%.

As in the scalar case the distribution for the full process is not symmetric and there is an enhancement to the invariant anti-lepton jet invariant mass  $m_{inv}$  for  $m_{inv} < m_{LQ}$ . There is also an increase in the total-cross section, at LO the cross-section for the full non-factorisable process is 5.57 pb. This increase is primarily due to the enhancement in the region  $m_{inv} < m_{LQ}$ .

The NLO corrections (shown in figure 4.7) show a much bigger enhancement over the LO result than occurs in the NWA. For the full process the peak height is  $6.85 \times 10^{-2}$  giving a large enhancement of 67% over the LO result. The total cross-section also has an increase of 59% to 8.85 pb.

The additional LO results (shown in figure 4.12) are non-resonant and don't make a large contribution to the main LO result, the cross-section for this process is

2.90 pb. Again this validates the decision to only include this additional process at LO.

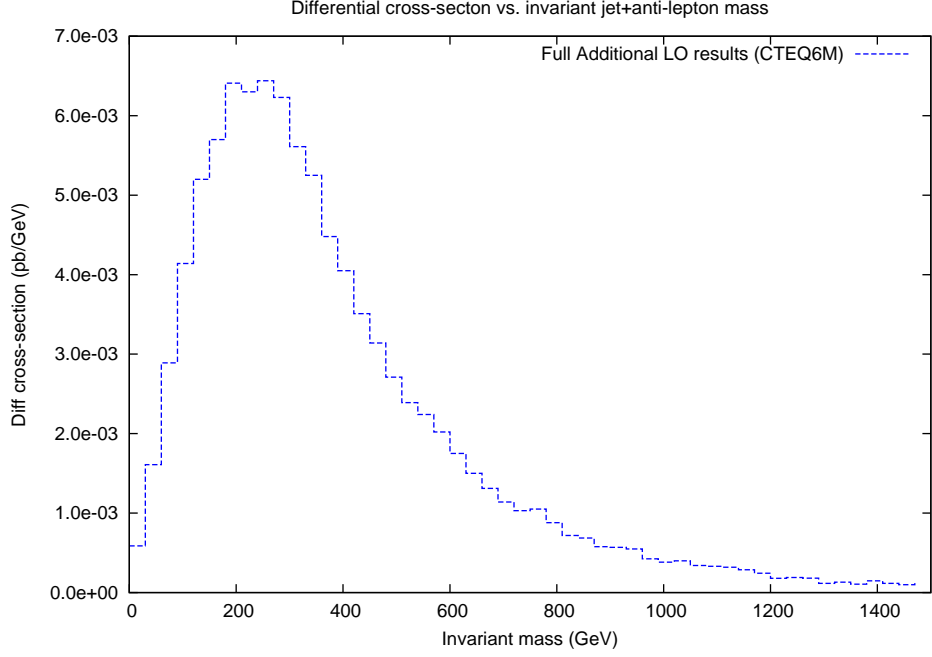


**Figure 4.12:** Additional LO results for producing a vector  $LQ$  in the full non-factorisable process (CTEQ6M).

The additional NLO results (which also include the additional LO contribution) also show a much bigger enhancement over the LO than occurs in the NWA (see figure 4.8). For the full process the peak height is  $6.93 \times 10^{-2}$  pb/GeV giving a large enhancement of 69% over the LO result. The total cross-section also has an enhancement of 115% to 11.96 pb.

Combining all of the contributions the total NLO results (shown in figure 4.9) has a resonant peak with a height of  $9.67 \times 10^{-2}$  pb/GeV giving an enhancement of 135% over the LO result. The cross-section for the total NLO contributions is increased by 173% to 15.23 pb. For comparison, the LO and total NLO contributions are shown in figure 4.13. A summary of the CTEQ6M results are given in tables 4.5 and 4.6.

Comparing the peak heights between the NWA and full process at NLO shows

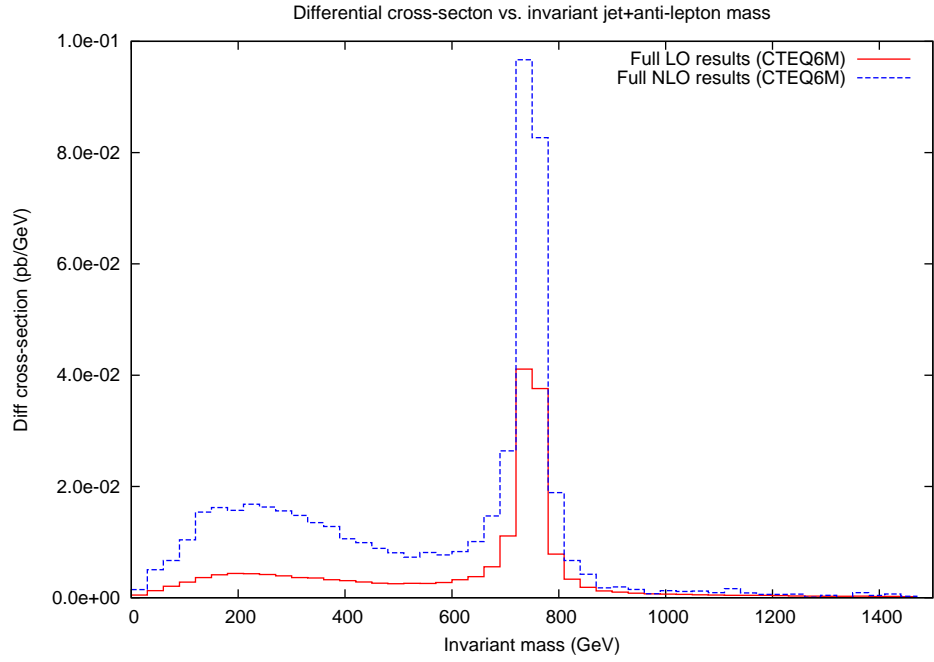


**Figure 4.13:** A comparison between the LO and NLO contributions for producing a vector  $LQ$  in the non-factorisable process (CTEQ6M).

Correction Type	Peak Height (pb/GeV)	Percentage change on LO
Tree	$4.11 \times 10^{-2}$	-
QCD	$6.85 \times 10^{-2}$	+67%
Additional	$6.93 \times 10^{-2}$	+69%
Total	$9.67 \times 10^{-2}$	+135%

**Table 4.5:** Summary of the CTEQ6M vector results for the non-factorisable process.

Correction Type	Total cross-section (pb)	Percentage change on LO
Tree	5.57	-
QCD	8.85	+59%
Additional	11.96	+115%
Total	15.23	+173%

**Table 4.6:** Summary of the CTEQ6M vector results for the non-factorisable process.

an even bigger difference than at LO. In the NWA the resonant peak has a height of  $7.44 \times 10^{-2}$  pb/GeV and in the full process the peak height is  $9.67 \times 10^{-2}$  pb/GeV which is 30% increase over the NWA. In going from LO to NLO the discrepancy of the peak height between the NWA and the full non-factorisable process increases from 8% to 30% - this is illustrated in figures 4.6 and 4.9.

As in the case with the NWA the CTEQ6L folding gives comparable results to the CTEQ6M folding, but again there is a systematic decrease in the peak-heights and cross-sections (see figure 4.14). A summary of the main results is shown in tables 4.7 and 4.8.

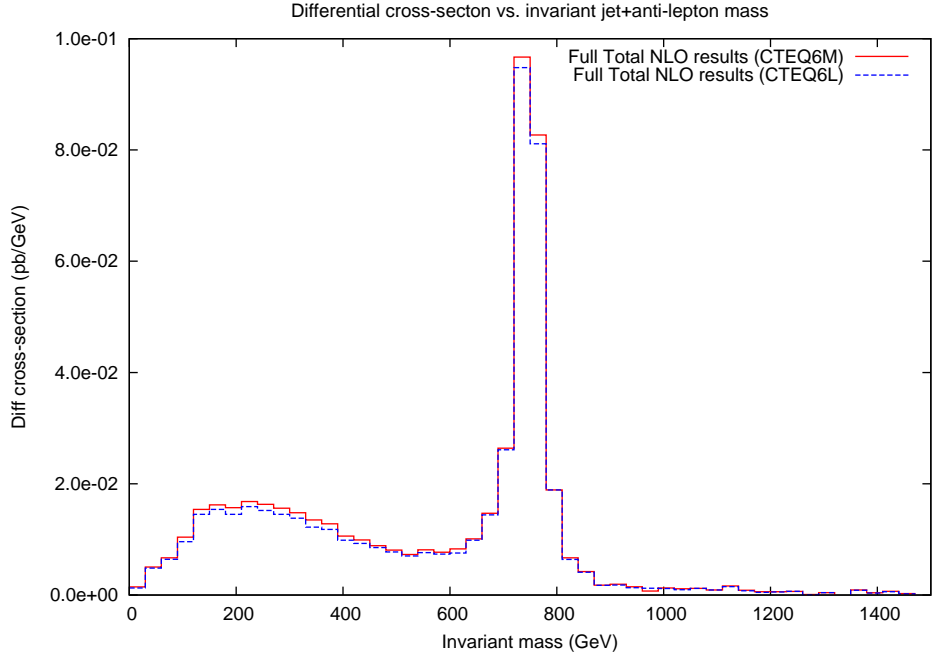


**Figure 4.14:** Total NLO results for producing a vector  $LQ$  in the full non-factorisable process - comparing the CTEQ6M and CTEQ6L PDF sets.

Correction Type	Peak Height (pb/GeV)	Percentage change on LO
Tree	$3.95 \times 10^{-2}$	-
QCD	$6.65 \times 10^{-2}$	+68%
Additional	$6.77 \times 10^{-2}$	+71%
Total	$9.48 \times 10^{-2}$	+140%

**Table 4.7:** Summary of the CTEQ6L vector results for the non-factorisable process.

Correction Type	Total cross-section (pb)	Percentage change on LO
Tree	5.12	-
QCD	8.30	+62%
Additional	11.44	+123%
Total	14.62	+186%

**Table 4.8:** *Summary of the CTEQ6L vector results for the non-factorisable process.*

## Chapter 5

# Conclusions

Having compiled the results for the NWA and the full non-factorisable process for both a scalar ( $R_2$ ) and vector ( $U_1$ ) LQ we will conclude with a discussion and comparison of these results.

### 5.1 Scalar Leptoquarks

In general the NWA involving an intermediate scalar particle should give a good approximation to the full result close to the resonant region. The reason for this is there is no sum over helicities to consider and so the only approximation needed is that the decay-width is narrow and the intermediate propagator can be treated as a Dirac  $\delta$  function.

Comparing the scalar LQ results between the NWA and the full non-factorisable process (see tables 3.5 and 3.9) the effectiveness of the NWA approximating the full non-factorisable process at NLO is confirmed. In particular we see that both sets of results give good agreement between the heights of the resonant peaks - the dominant feature in both sets of distributions.

Away from the resonant peak there are differences in the invariant mass distributions between the NWA and full non-factorisable process. The NWA gives a symmetric distribution around the resonant peak whereas the non-factorisable pro-



cess gives a non-symmetric distribution. In particular there is an enhancement to the distribution for values of the invariant mass  $m_{\text{inv}} < m_{\text{LQ}}$  coming from the non-factorisable contributions to the full process. The enhancement to the distribution away from the resonant peak does make a large contribution to the total cross-section (see tables 3.6 and 3.10) and we see a large difference between the cross-sections calculated in the NWA and full non-factorisable process.

## 5.2 Vector Leptoquarks

Comparing the vector LQ results the NWA does not provide as good an approximation to the full non-factorisable process for vector LQs as it does for scalars. The key reason for this is because in the NWA the interference between the different helicity states of the intermediate LQ are assumed to be negligible and are ignored. Looking at the difference between the resonant peak heights in tables 4.1 and 4.5 the agreement between the two sets of results is not as close as in the scalar case and suggests that the helicity interference terms do make a noticeable contribution.

The anti-lepton/jet invariant mass distribution also shows the same features as in the scalar LQ case. The NWA gives a symmetric distribution around the resonance, but the full non-factorisable process also shows an enhancement to the distribution for values of the invariant mass  $m_{\text{inv}} < m_{\text{LQ}}$ . This enhancement makes a sizeable difference to the total cross-section (see tables 4.2 and 4.6). The total cross-section for the non-factorisable process is significantly larger than in the NWA and this increase is primarily caused by the additional NLO corrections.

In general when looking at both the scalar and vector LQ results there are two important features they have in common:

- The NLO corrections are large compared to the LO results, particularly with regards to the full non-factorisable process, but this is often the case when including QCD corrections (see for example [39]).
- From the non-factorisable results there are substantial corrections below the resonance, particularly with regards to the vector LQs, and it is possible these

could be observed to give an indirect hint of the presence of LQs.

### 5.3 Future Work

The focus of this thesis has been the study of the effectiveness of the NWA at approximating the LQ production process at both LO and NLO, however it should be mentioned that performing the calculations at NLO introduces renormalisation and factorisation scales. In principal the choice of the values of these scales is arbitrary, however due to the nature of perturbative calculations the NLO calculations will have some sensitivity to these scales. Based on the work conducted in this thesis it would be a beneficial to extend the results to determine the sensitivity of the NLO calculations to the renormalisation and factorisation scales.

# Appendices

## Appendix A

# Helicity Projection

The helicity projection technique makes it possible to trace out spinors and  $\gamma$ -matrices at the amplitude level. This is a useful when performing numerical calculations at the amplitude level as it avoids the need to encode spinors and  $\gamma$ -matrices in a computer program.

Since this is a study of high energy physics the masses of the fermions can be assumed to be zero. This assumption simplifies the helicity projection technique.

### A.1 Projecting an Even Number of $\gamma$ -matrices

The technique of helicity projection can best be understood by example. To simplify the example all non-relevant components of the amplitude, such as coupling constants, Lorentz indices etc. are being ignored. In the simplest case consider an amplitude with an even number of  $\gamma$ -matrices with an incoming fermion with momentum  $p$  and helicity  $\lambda'$  and an outgoing fermion with momentum  $q$  and helicity  $\lambda$ . The amplitude can be written as

$$\mathcal{A}(\lambda, \lambda') = \bar{u}(q, \lambda) \Gamma_{\text{even}} u(p, \lambda') \tag{A.1}$$

where  $\Gamma_{\text{even}}$  represents an even number of  $\gamma$ -matrices. If we consider the simple spinor product

$$\mathcal{A}_0(\lambda, \lambda') = \bar{u}(q, \lambda)u(p, \lambda') \quad (\text{A.2})$$

then, up to a phase  $\eta$  the amplitude  $\mathcal{A}$  can be written as

$$e^{i\eta}\mathcal{A} = \frac{\bar{\mathcal{A}}_0\mathcal{A}}{|\mathcal{A}_0|} \quad (\text{A.3})$$

where  $|\mathcal{A}_0| = \sqrt{\sum_{\lambda, \lambda'} |\mathcal{A}_0|^2}$ .

The  $\gamma$ -matrices can now be traced out in eq.(A.3) by introducing helicity projection operators as follows

$$\begin{aligned} \bar{\mathcal{A}}_0\mathcal{A}(\lambda, \lambda') &= \bar{u}(p, \lambda')u(q, \lambda)\bar{u}(q, \lambda)\Gamma_{\text{even}}u(p, \lambda') \\ &= \sum_{\underline{\lambda}, \underline{\lambda}'} \bar{u}(p, \underline{\lambda}')u(q, \underline{\lambda})\bar{u}(q, \underline{\lambda})\left(\frac{1-\lambda\gamma^5}{2}\right)\Gamma_{\text{even}}\left(\frac{1+\lambda'\gamma^5}{2}\right)u(p, \underline{\lambda}') \\ &= \text{Tr}\left[\not{q}\left(\frac{1-\lambda\gamma^5}{2}\right)\Gamma_{\text{even}}\left(\frac{1+\lambda'\gamma^5}{2}\right)\not{p}\right] \\ &= \text{Tr}\left[\not{q}\left(\frac{1-\lambda\gamma^5}{2}\right)\Gamma_{\text{even}}\not{p}\right] \quad (\text{where } \lambda = -\lambda') \end{aligned} \quad (\text{A.4})$$

Combining this result with the fact that  $|\mathcal{A}_0| = \sqrt{2p \cdot q}$  gives the final result as

$$e^{i\eta}\mathcal{A}(\lambda) = \frac{1}{\sqrt{2p \cdot q}}\text{Tr}\left[\not{q}\left(\frac{1-\lambda\gamma^5}{2}\right)\Gamma_{\text{even}}\not{p}\right] \quad (\text{A.5})$$

For the purpose of this example it was assumed that the initial and final states were fermions. In the case of anti-fermions eq.(A.1) would be

$$\mathcal{A}(\lambda, \lambda') = \bar{v}(q, \lambda)\Gamma_{\text{even}}v(p, \lambda') \quad (\text{A.6})$$

and to perform the helicity projection  $\mathcal{A}_0$  would need to be

$$\mathcal{A}_0(\lambda, \lambda') = \bar{v}(q, \lambda)v(p, \lambda') \quad (\text{A.7})$$

which gives the same result as in eq.(A.5).

From the last line of eq.(A.4) it can be seen that a process with an even number

of  $\gamma$ -matrices flips the helicity between the incoming and outgoing fermion/anti-fermion states.

## A.2 Projecting an Odd Number of $\gamma$ -matrices

Dealing with an odd number of  $\gamma$ -matrices is slightly more complicated. If the number of  $\gamma$ -matrices appearing in eq.(A.5) was odd the result of the trace would give zero. Dealing with an odd-number of  $\gamma$ -matrices requires the introduction of an auxiliary momenta  $w$  with the properties that

$$\begin{aligned} w.w &= -1 \\ w.p &= w.q = 0 \end{aligned} \tag{A.8}$$

The procedure follows as before with the exception that  $\mathcal{A}_0$  is replaced with

$$\mathcal{A}_0(\lambda, \lambda') = \bar{u}(q, \lambda) \psi u(p, \lambda') \tag{A.9}$$

where the conditions in eq.(A.8) ensure that  $|\mathcal{A}_0| = \sqrt{2p \cdot q}$  as before. This gives

$$\begin{aligned} \bar{\mathcal{A}}_0 \mathcal{A}(\lambda, \lambda') &= \bar{u}(p, \lambda') \psi u(q, \lambda) \bar{u}(q, \lambda) \Gamma_{\text{odd}} u(p, \lambda') \\ &= \text{Tr} \left[ \psi \not{q} \left( \frac{1 - \lambda \gamma^5}{2} \right) \Gamma_{\text{odd}} \not{p} \right] \quad (\text{where } \lambda = \lambda') \end{aligned} \tag{A.10}$$

which results in

$$e^{in} \mathcal{A}(\lambda) = \frac{1}{\sqrt{2p \cdot q}} \text{Tr} \left[ \psi \not{q} \left( \frac{1 - \lambda \gamma^5}{2} \right) \Gamma_{\text{odd}} \not{p} \right] \tag{A.11}$$

As before the same result would be reached if the initial and final states were anti-fermions. In the case that the process has an odd number of  $\gamma$ -matrices the helicity between the incoming and outgoing fermion/anti-fermion states does not flip.

### A.2.1 Simplifying the Final Expression

In practice the outcome of the traces can result in rather complex expressions, but in the case of an odd number of  $\gamma$ -matrices these expressions can be simplified by introducing another vector  $v(\lambda)$  constructed from  $w$  as

$$v^\mu(\lambda) = \frac{1}{2} \left( w^\mu - i\lambda \frac{1}{p \cdot q} e^{\alpha\beta\gamma\mu} p_\alpha q_\beta w_\gamma \right) \quad (\text{A.12})$$

This allows eq.(A.11) to be rewritten in the simpler form

$$e^{i\eta} \mathcal{A}(\lambda) = \frac{1}{\sqrt{2p \cdot q}} \text{Tr} [\not{v}(\lambda) \not{q} \Gamma_{\text{odd}} \not{p}] \quad (\text{A.13})$$

## A.3 Generalising the Projection

In general an amplitude involving an arbitrary number of fermions and anti-fermions can be written in product form as

$$\begin{aligned} \mathcal{A}(\lambda_i, \lambda'_i) &= \bar{u}(q_1, \lambda_1) \Gamma_1 u(p_i, \lambda'_1) \cdots \bar{v}(q_n, \lambda_n) \Gamma_n v(p_n, \lambda'_n) \cdots \\ &= \prod_i \mathcal{A}_i(\lambda_i, \lambda'_i) \end{aligned} \quad (\text{A.14})$$

and the  $\gamma$ -matrices in each of the  $\mathcal{A}_i$ 's can be traced out using either eq.(A.5) or eq.(A.13) depending on whether the number of  $\gamma$ -matrices in each  $\mathcal{A}_i$  is even or odd.

## Appendix B

# Analytic Loop Calculations

Most of the virtual corrections are evaluated numerically using SAMURAI, however there are specific cases where the corrections are done analytically. This appendix details these calculations, which are evaluated using dimensional regularisation [40] and the  $\overline{\text{MS}}$ -scheme.

### B.1 External Massless Fermions

The virtual corrections for an external massless fermion are determined by calculating the wavefunction renormalisation factor  $Z$  from the 1PI diagrams for the fermion propagator.

At next-to-leading order the 1PI diagrams  $-i\Sigma(\not{p})$  are a sum of each of the  $n$  1-loop corrections to the fermion propagator, that is

$$-i\Sigma(\not{p}) = -i \left( \Sigma_1(\not{p}) + \cdots + \Sigma_n(\not{p}) \right) \quad (\text{B.1})$$

The general form of each of these loops is

$$-i\Sigma_j(\not{p}) = -i\mu^{4-d} \int \frac{d^d k}{(2\pi)^d} \frac{C_j^{(1)} \not{k} + C_j^{(2)} \not{p}}{k^2 [(k-p)^2 - m_j^2]} \quad (\text{B.2})$$

where the coefficients  $C_j^{(i)}$  and the mass  $m_j$  depend on the exact topology of each



loop. Expanding in a series about  $\not{p} = 0$  gives

$$\Sigma_j(\not{p}) \approx \Sigma_j(0) + \left. \frac{d\Sigma_j}{d\not{p}} \right|_{\not{p}=0} \not{p} = \left. \frac{d\Sigma_j}{d\not{p}} \right|_{\not{p}=0} \not{p} \quad \text{since } \Sigma_j(0) = 0 \quad (\text{B.3})$$

The wavefunction renormalisation factor for fermions is defined as

$$Z^{-1} = 1 - \left. \frac{d\Sigma}{d\not{p}} \right|_{\not{p}=0} \quad (\text{B.4})$$

and since  $\left. \frac{d\Sigma}{d\not{p}} \right|_{\not{p}=0} \ll 1$  this can be rewritten as

$$\begin{aligned} \delta Z &\approx \left. \frac{d\Sigma}{d\not{p}} \right|_{\not{p}=0} \Rightarrow \Sigma(\not{p}) \approx \delta Z \not{p} \quad (\text{from eq.(B.3)}) \\ &\Rightarrow \delta Z \approx \text{Tr}\{\Sigma(\not{p})\not{p}\} \Big|_{\not{p}=0} \end{aligned} \quad (\text{B.5})$$

where  $\delta Z = Z - 1$ . Therefore, from eq.(B.1)

$$\begin{aligned} \delta Z &\approx \text{Tr}\{\Sigma_1(\not{p})\not{p}\} \Big|_{\not{p}=0} + \cdots + \text{Tr}\{\Sigma_n(\not{p})\not{p}\} \Big|_{\not{p}=0} \\ &= \delta Z_1 + \cdots + \delta Z_n \end{aligned} \quad (\text{B.6})$$

with

$$\begin{aligned} \delta Z_j &= \frac{\mu^{4-d}}{p^2} \int \frac{d^d k}{(2\pi)^d} \frac{4(C_j^{(1)} k \cdot p + C_j^{(2)} p^2)}{k^2 [(k-p)^2 - m_j^2]} \Big|_{\not{p}=0} \\ &= \mu^{4-d} \int_0^1 d\alpha \int \frac{d^d k}{(2\pi)^d} \frac{4(C_j^{(1)} + C_j^{(2)}) \alpha}{[k^2 - \Delta]^2} \quad \text{where } \Delta = \alpha m_j^2 \end{aligned} \quad (\text{B.7})$$

In the second line Feynman parametrisation has been used to bring the integral to a standard form. From the second line of eq.(B.7) it is clear that  $\delta Z = 0$  when  $m_j^2 = 0$ , therefore the only contribution to the external corrections for a massless fermion come from those diagrams with a massive internal particle.

Performing the integral over  $k$ , setting  $d = 4 - 2\epsilon$  and taking the limit  $\epsilon \rightarrow 0$

gives

$$\begin{aligned}\delta Z_j &= \frac{i}{16\pi^2} \int_0^1 d\alpha \left[ \frac{4\alpha}{\epsilon} - 4\alpha \log \left( \frac{\Delta}{\mu^2} \right) \right] (C_j^{(1)} + C_j^{(2)}) \\ &= \frac{i}{16\pi^2} \left[ \frac{2}{\epsilon} - 2 \log \left( \frac{m_j^2}{\mu^2} \right) + 1 \right] (C_j^{(1)} + C_j^{(2)})\end{aligned}\tag{B.8}$$

in the  $\overline{\text{MS}}$ -scheme. Using this result all the external leg corrections to a massless fermion can be readily determined as only the mass  $m_j$  and coefficients  $C_j^{(1)}$  and  $C_j^{(2)}$  need to be established.

## B.2 External Gluons

As with external fermions the virtual corrections for external gluons are determined by calculating the wavefunction renormalisation factor  $Z$  from the 1PI diagrams for the gluon propagator.

The only corrections to the gluon propagator come from the standard QCD loop corrections with the additional corrections from a massive LQ. The combined set of all  $n$  loop diagrams form a gauge invariant set i.e.

$$\begin{aligned}i\Pi^{\mu\nu}(p^2) &= i(\Pi_1^{\mu\nu}(p^2) + \dots + \Pi_n^{\mu\nu}(p^2)) \\ &= i(g^{\mu\nu}p^2 - p^\mu p^\nu)\Pi(p^2)\end{aligned}\tag{B.9}$$

where  $p$  is the momentum of the gluon and  $\mu$  and  $\nu$  are the Lorentz indices for the gluon propagator. To simplify the notation the colour indices are contained within the  $\Pi$  factors.

The wavefunction renormalisation factor for gluons is defined as

$$Z^{-1} = 1 - \Pi(0)\tag{B.10}$$

and since  $\Pi(0) \ll 1$  this can be rewritten as

$$\delta Z \approx \Pi(0)\tag{B.11}$$

where again  $\delta Z = Z - 1$ .

Each of the  $i\Pi_j^{\mu\nu}(p^2)$  terms can be written as

$$i\Pi_j^{\mu\nu}(p^2) = A_j(p^2)g^{\mu\nu}p^2 - B_j(p^2)p^\mu p^\nu \quad (\text{B.12})$$

with all of the coefficients  $A_j$  and  $B_j$  summing to give the Lorentz structure as shown in eq.(B.9). In order to determine  $\Pi(0)$  it is necessary to calculate the coefficients  $A_j(0)$  and  $B_j(0)$ .

For a bubble diagram the general form of the loop integral is

$$\begin{aligned} i\Pi_j^{\mu\nu}(p^2) = & \mu^{4-d} \int \frac{d^d k}{(2\pi)^d} \frac{1}{[k^2 - m_{j_1}^2][(k-p)^2 - m_{j_2}^2]} \\ & \times \left( \left[ C_j^{(1)}k^2 + C_j^{(2)}k \cdot p + C_j^{(3)}p^2 \right] g^{\mu\nu} + \right. \\ & \left. C_j^{(4)}k^\mu k^\nu + C_j^{(5)}(k^\mu p^\nu + p^\mu k^\nu) + C_j^{(6)}p^\mu p^\nu \right) \end{aligned} \quad (\text{B.13})$$

where the coefficients  $C_j^{(i)}$  and masses  $m_{j_1}$  and  $m_{j_2}$  depend on the exact form of the loop. Using Feynman parametrisation and exploiting the general structure of the integral, as given in eq.(B.12), it can be shown that

$$A_j(0)p^2 = \mu^{4-d} \int_0^1 d\alpha \int \frac{d^d k}{(2\pi)^d} \frac{(C_j^{(1)} + C_j^{(4)})k^2}{[k^2 - \Delta]^2} \quad (\text{B.14})$$

$$B_j(0) = \mu^{4-d} \int_0^1 d\alpha \int \frac{d^d k}{(2\pi)^d} \frac{-(C_j^{(4)}\alpha^2 + C_j^{(5)}\alpha + C_j^{(6)})}{[k^2 - \Delta]^2} \quad (\text{B.15})$$

where  $\Delta = -(\alpha - 1)m_{j_1}^2 + \alpha m_{j_2}^2$ .

For a tadpole diagram the general form of the loop integral is

$$i\Pi_j^{\mu\nu}(p^2) = \mu^{4-d} \int \frac{d^d k}{(2\pi)^d} \frac{C_j g^{\mu\nu}}{[k^2 - m_j^2]} \quad (\text{B.16})$$

giving

$$A_j(0)p^2 = \mu^{4-d} \int_0^1 d\alpha \int \frac{d^d k}{(2\pi)^d} \frac{C_j}{[k^2 - m_j^2]} \quad (\text{B.17})$$

$$B_j(0) = 0 \quad (\text{B.18})$$

From the form of the integrals in eq.(B.14), eq.(B.15) and eq.(B.17) it is clear that these are zero in the massless case (i.e.  $m_{j_1} = m_{j_2} = 0$ ) and since the standard QCD loop corrections to the gluon propagator only involve massless particles the only contribution to  $\delta Z$  comes from loops with an internal massive LQ.

In the case of an internal LQ (where  $m_{j_1} = m_{j_2} = m_{\text{LQ}}$ ) the result of the bubble loop integrals in eq.(B.14) and eq.(B.15) are

$$A_j(0) p^2 = \frac{i}{16\pi^2} \left[ \frac{2}{\epsilon} + 1 - 2 \log \left( \frac{m_{\text{LQ}}^2}{\mu^2} \right) \right] m_{\text{LQ}}^2 (C_j^{(1)} + C_j^{(4)}) \quad (\text{B.19})$$

$$B_j(0) = -\frac{i}{16\pi^2} \left[ \frac{1}{\epsilon} + \log \left( \frac{m_{\text{LQ}}^2}{\mu^2} \right) \right] \left( \frac{C_j^{(4)}}{3} + \frac{C_j^{(5)}}{2} + C_j^{(6)} \right) \quad (\text{B.20})$$

where  $d = 4 - 2\epsilon$  and the integrals are evaluated in the limit  $\epsilon \rightarrow 0$  using the  $\overline{MS}$ -scheme.

Likewise, for the tadpole integral

$$A_j(0) p^2 = \frac{i}{16\pi^2} \left[ \frac{1}{\epsilon} + 1 - \log \left( \frac{m_{\text{LQ}}^2}{\mu^2} \right) \right] m_{\text{LQ}}^2 C_j \quad (\text{B.21})$$

Once the coefficients  $C_j^{(i)}$  for the LQ loops have been found the above integrals can be readily used to calculate the external leg corrections for a gluon.

### B.3 External Scalar Leptoquarks

As with the virtual corrections for external fermions, the corrections for an external scalar LQ is a sum of 1-loop diagrams (see eq.(B.1)) with each of the 1-loop integrals having the form

$$-i\Sigma_j(p^2) = -i\mu^{4-d} \int \frac{d^d k}{(2\pi)^d} \frac{C_j^{(1)} k^2 + C_j^{(2)} k \cdot p + C_j^{(3)} p^2}{[k^2 - m_j^2][(k-p)^2 - m_{\text{LQ}}^2]} \quad (\text{B.22})$$

or

$$-i\Sigma_j(p^2) = -i\mu^{4-d} \int \frac{d^d k}{(2\pi)^d} \frac{C_j^{(1)} k^2 + C_j^{(2)} k \cdot p + C_j^{(3)} p^2}{k^2(k-p)^2} \quad (\text{B.23})$$

As before the coefficients  $C_j^{(i)}$  and mass  $m_j$  depend on the particular loop.

For scalar particles the wavefunction renormalisation factor is

$$Z^{-1} = 1 - \left. \frac{d\Sigma}{dp^2} \right|_{p^2=m_{\text{LQ}}} \quad (\text{B.24})$$

and since  $\left. \frac{d\Sigma}{dp^2} \right|_{p^2=m_{\text{LQ}}} \ll 1$  this can be expanded to give

$$\begin{aligned} \delta Z &\approx \left. \frac{d\Sigma_1}{dp^2} \right|_{p^2=m_{\text{LQ}}} + \cdots + \left. \frac{d\Sigma_n}{dp^2} \right|_{p^2=m_{\text{LQ}}} \\ &= \delta Z_1 + \cdots + \delta Z_n \end{aligned} \quad (\text{B.25})$$

Using Passarino-Veltman reduction [17] it can be shown that each  $\delta Z_j$ , where the loop is of the form given in eq.(B.22), can be written as

$$\delta Z_j = \left( \frac{C_j^{(2)}}{2} + C_j^{(3)} \right) I_1 + \left( C_j^{(1)} m_j^2 + \frac{C_j^{(2)}}{2} m_j^2 + C_j^{(3)} m_{\text{LQ}}^2 \right) I_2 \quad (\text{B.26})$$

where  $I_1$  and  $I_2$  are

$$I_1 = \mu^{4-d} \int \frac{d^d k}{(2\pi)^d} \frac{1}{[k^2 - m_j^2][(k-p)^2 - m_{\text{LQ}}^2]} \Big|_{p^2=m_{\text{LQ}}} \quad (\text{B.27})$$

$$I_2 = \mu^{4-d} \frac{d}{dp^2} \int \frac{d^d k}{(2\pi)^d} \frac{1}{[k^2 - m_j^2][(k-p)^2 - m_{\text{LQ}}^2]} \Big|_{p^2=m_{\text{LQ}}} \quad (\text{B.28})$$

In the  $\overline{\text{MS}}$ -bar scheme the result of these integrals are

$$\begin{aligned} I_1 = \frac{i}{16\pi^2} \left[ \frac{1}{\epsilon} - \log \left( \frac{m_{\text{LQ}}^2}{\mu^2} \right) + 2 - (1 - \alpha_+) \log(1 - \alpha_+) - \alpha_+ \log(-\alpha_+) \right. \\ \left. - (1 - \alpha_-) \log(1 - \alpha_-) - \alpha_- \log(-\alpha_-) \right] \end{aligned} \quad (\text{B.29})$$

$$\begin{aligned} I_2 = -\frac{i}{16\pi^2} \frac{1}{m_{\text{LQ}}^2} \left[ 1 - \alpha_+ \frac{(1 - \alpha_+)}{(\alpha_+ - \alpha_-)} \log \left( 1 - \frac{1}{\alpha_+} \right) \right. \\ \left. - \alpha_- \frac{(1 - \alpha_-)}{(\alpha_- - \alpha_+)} \log \left( 1 - \frac{1}{\alpha_-} \right) \right] \end{aligned} \quad (\text{B.30})$$

where

$$\alpha_{\pm} = \frac{m_j^2}{2m_{\text{LQ}}^2} \pm \sqrt{\frac{m_j^4}{4m_{\text{LQ}}^4} - \frac{m_j^2}{m_{\text{LQ}}^2}} \quad (\text{B.31})$$

In the case when  $m_j = 0$  these integrals simplify to

$$I_1 = \frac{i}{16\pi^2} \left[ \frac{1}{\epsilon} - \log \left( \frac{m_{\text{LQ}}^2}{\mu^2} \right) + 2 \right] \quad (\text{B.32})$$

$$I_2 = -\frac{i}{16\pi^2} \frac{1}{m_{\text{LQ}}^2} \left[ \frac{1}{2\epsilon} + 1 - \frac{1}{2} \log \left( \frac{m_{\text{LQ}}^2}{\mu^2} \right) \right] \quad (\text{B.33})$$

Again using Passarino-Veltman reduction when the loops are of the form given in eq.(B.23) each  $\delta Z_j$  can be written as

$$\delta Z_j = \left( \frac{C_j^{(2)}}{2} + C^{(3)} \right) (I_1 + m_{\text{LQ}}^2 I_2) \quad (\text{B.34})$$

where  $I_1$  and  $I_2$  are

$$I_1 = \mu^{4-d} \int \frac{d^d k}{(2\pi)^d} \frac{1}{k^2(k-p)^2} \Big|_{p^2=m_{\text{LQ}}^2} \quad (\text{B.35})$$

$$I_2 = \mu^{4-d} \frac{d}{dp^2} \int \frac{d^d k}{(2\pi)^d} \frac{1}{k^2(k-p)^2} \Big|_{p^2=m_{\text{LQ}}^2} \quad (\text{B.36})$$

and in the  $\overline{\text{MS}}$ -bar scheme these result in

$$I_1 = \frac{i}{16\pi^2} \left[ \frac{1}{\epsilon} - \log \left( \frac{m_{\text{LQ}}^2}{\mu^2} \right) + 2 - i\pi \right] \quad (\text{B.37})$$

$$I_2 = -\frac{i}{16\pi^2} \frac{1}{m_{\text{LQ}}^2} \quad (\text{B.38})$$

It should be noted that the  $i\pi$  term appearing in eq.(B.37) is a consequence of the LQ being an unstable particle (i.e. there is decay channel for a LQ to decay to two massless particles - a lepton and quark. This imaginary term forms the decay width, which appears in the propagator of an unstable particle, but only the real part of eq.(B.37) is needed for calculating the wavefunction renormalisation factor.

## B.4 External Vector Leptoquarks

For the vector LQ the only loops being considered come from QCD loop corrections. As with the external gluon the combined set of all  $n$  loop diagrams form a gauge

invariant set as shown in eq.(B.9).

Being a massive particle the wavefunction renormalisation for LQs is defined as

$$Z^{-1} = 1 - \Pi(m_{\text{LQ}}^2) \quad (\text{B.39})$$

and since  $\Pi(m_{\text{LQ}}^2) \ll 1$  this can be written as

$$\delta Z \approx \Pi(m_{\text{LQ}}^2) \quad (\text{B.40})$$

Each bubble diagram has the same form as eq.(B.13) with  $m_{j_1} = m_{\text{LQ}}$  and  $m_{j_2} = 0$ . This gives

$$A_j(m_{\text{LQ}}^2) p^2 = \mu^{4-d} \int_0^1 d\alpha \int \frac{d^d k}{(2\pi)^d} \frac{(C_j^{(1)} + C_j^{(4)})k^2}{[k^2 - \Delta]^2} \quad (\text{B.41})$$

$$B_j(m_{\text{LQ}}^2) = \mu^{4-d} \int_0^1 d\alpha \int \frac{d^d k}{(2\pi)^d} \frac{-(C_j^{(4)}\alpha^2 + C_j^{(5)}\alpha + C_j^{(6)})}{[k^2 - \Delta]^2} \quad (\text{B.42})$$

where  $\Delta = (\alpha - 1)^2 m_{\text{LQ}}$ . The result of these loop integrals are

$$A_j(m_{\text{LQ}}^2) p^2 = \frac{i}{16\pi^2} \left[ \frac{2}{3\epsilon} + \frac{7}{9} - \frac{2}{3} \log \left( \frac{m_{\text{LQ}}^2}{\mu^2} \right) \right] m_{\text{LQ}}^2 (C_j^{(1)} + C_j^{(4)}) \quad (\text{B.43})$$

$$B_j(m_{\text{LQ}}^2) = -\frac{i}{16\pi^2} \left\{ \left[ \frac{1}{\epsilon} + \log \left( \frac{m_{\text{LQ}}^2}{\mu^2} \right) \right] \left( \frac{C_j^{(4)}}{3} + \frac{C_j^{(5)}}{2} + C_j^{(6)} \right) + \frac{11}{9} C_j^{(4)} + \frac{3}{2} C_j^{(5)} + 2C_j^{(6)} \right\} \quad (\text{B.44})$$

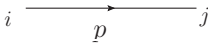
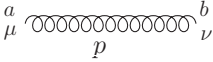
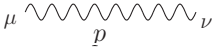
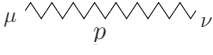
# Appendix C

## Feynman Rules

The relevant Feynman rules given in this appendix are in the Feynman gauge and only those Feynman rules used in this project are included. For the vertices all momenta are defined to be incoming and the colour flow is taken to be from  $i$  to  $j$ .

### C.1 Standard Model

#### Propagators:

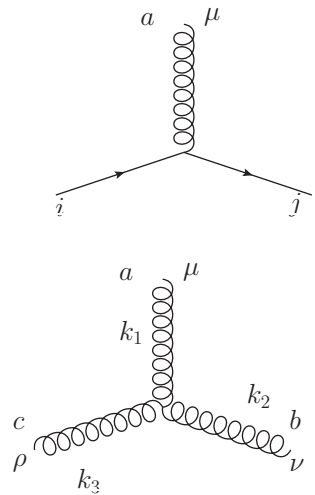
Massless fermion propagator:		$\frac{i\delta_{ij}\not{p}}{p^2}$
Gluon propagator:		$\frac{-i\delta_{ab}g_{\mu\nu}}{p^2}$
Photon propagator:		$\frac{-ig_{\mu\nu}}{p^2}$
W and Z boson propagator:		$\frac{-i(g_{\mu\nu} - p_\mu p_\nu / m^2)}{p^2 - m^2}$

Where  $m = M_W$  or  $M_Z$ .



## Vertices:

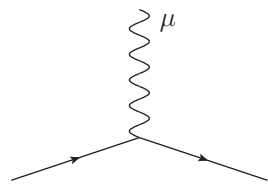
### QCD vertices



$$-igT_{ji}^a\gamma_\mu$$

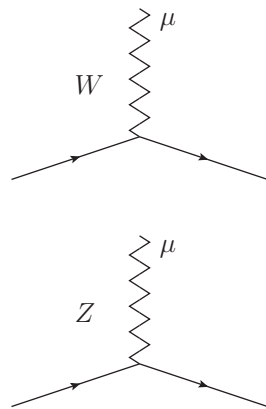
$$-gf^{abc}\left(g_{\mu\nu}(k_1-k_2)_\rho + g_{\nu\rho}(k_2-k_3)_\mu + g_{\rho\mu}(k_3-k_1)_\nu\right)$$

### QED vertices



$$-igA\gamma_\mu$$

### Electroweak vertices



$$-i\frac{g_W}{2\sqrt{2}}\gamma_\mu$$

$$-i\frac{g_Z}{2}\gamma_\mu$$

Here  $g$  is the strong coupling and  $g_A$ ,  $g_W$  and  $g_Z$  are the photon, W and Z boson couplings respectively. For the photon coupling to an electron and u-quark the couplings are

$$\begin{aligned} g_{A(e)} &= e & (e = \sqrt{4\pi\alpha}) \\ g_{A(u)} &= \frac{2}{3}e \end{aligned}$$

For the W boson coupling

$$g_W = \begin{cases} \frac{e}{\sin\theta_W} & (\lambda = -1) \\ 0 & (\lambda = +1) \end{cases}$$

where  $\theta_W$  is the Weinberg angle and  $\lambda$  is the helicity of the fermion. For the Z boson coupling to an electron and u-quark the couplings are

$$\begin{aligned} g_{Z(e)} &= g_Z \times \begin{cases} -1 + 2\sin^2\theta_W & (\lambda = -1) \\ 2\sin^2\theta_W & (\lambda = +1) \end{cases} \\ g_{Z(u)} &= g_Z \times \begin{cases} 1 - \frac{4}{3}\sin^2\theta_W & (\lambda = -1) \\ -\frac{4}{3}\sin^2\theta_W & (\lambda = +1) \end{cases} \end{aligned}$$

where  $g_Z = \frac{g_W}{\cos\theta_W}$ .

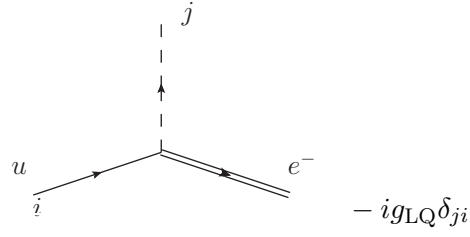
## C.2 Scalar Leptoquark

**Propagators:**

Scalar LQ propagator:  $\begin{array}{c} i \text{ --- } \xrightarrow{\quad p \quad} \text{ --- } j \end{array}$   $\frac{i\delta_{ij}}{p^2 - m_{\text{LQ}}^2}$

## Vertices:

Leptoquark vertex

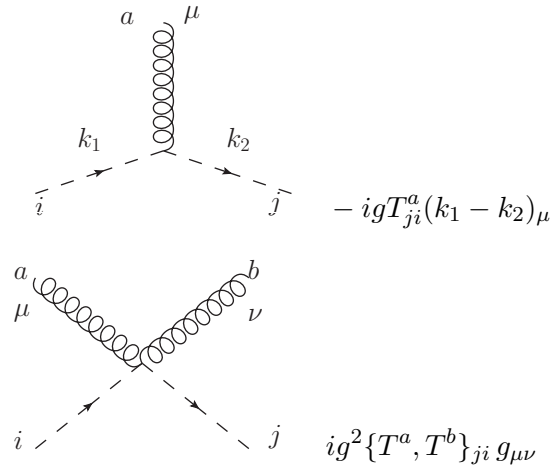


Where

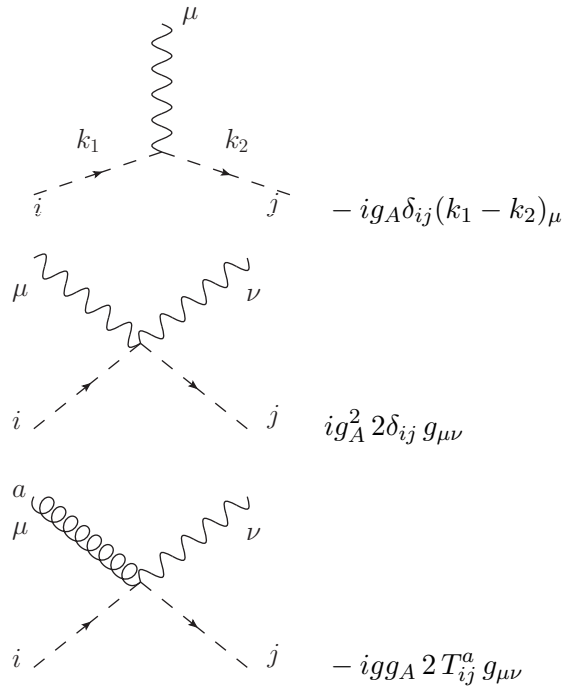
$$g_{LQ} = \begin{cases} h_{2L} & (\lambda = -1) \\ h_{2R} & (\lambda = +1) \end{cases}$$

and  $\lambda$  is the helicity of the electron.

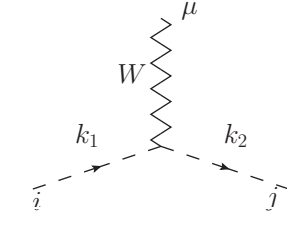
QCD vertices



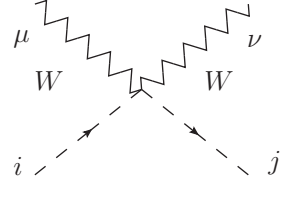
# QED vertices



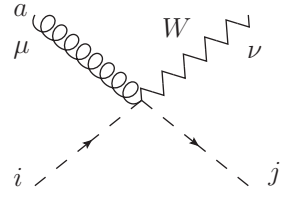
## Electroweak vertices



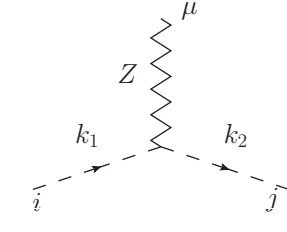
$$-i \frac{g_W}{\sqrt{2}} \delta_{ij} (k_1 - k_2)_\mu$$



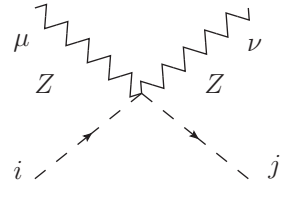
$$i \left( \frac{g_W}{\sqrt{2}} \right)^2 2\delta_{ij} g_{\mu\nu}$$



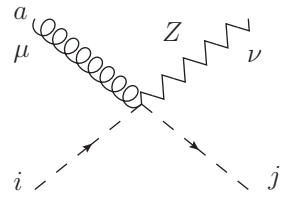
$$-igg_W 2T_{ij}^a g_{\mu\nu}$$



$$-ig_Z \delta_{ij} (k_1 - k_2)_\mu$$



$$ig_Z^2 2\delta_{ij} g_{\mu\nu}$$



$$-igg_Z 2T_{ij}^a g_{\mu\nu}$$

For the photon coupling to the LQ

$$g_{A(\text{LQ})} = \frac{5}{3}e$$

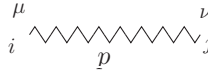
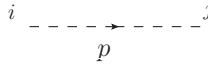
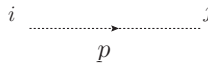
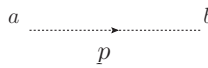
and for the Z boson coupling to the LQ

$$g_{Z(\text{LQ})} = g_Z \left( \frac{1}{2} - \frac{5}{3} \sin^2 \theta_W \right)$$

### C.3 Vector Leptoquark

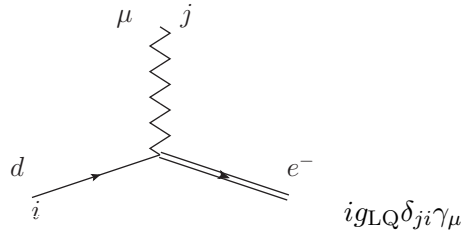
For this set of rules, which only involve QCD particles, the zigzag line will now represent the vector LQ.

**Propagators:**

Vector LQ propagator:		$\frac{-i\delta_{ij} g_{\mu\nu}}{p^2 - m_{\text{LQ}}^2}$
Goldstone boson propagator:		$\frac{i\delta_{ij}}{p^2 - m_{\text{LQ}}^2}$
LQ ghost propagator:		$\frac{i\delta_{ij}}{p^2 - m_{\text{LQ}}^2}$
Gluon ghost propagator:		$\frac{i\delta_{ab}}{p^2}$

**Vertices:**

Leptoquark vertex

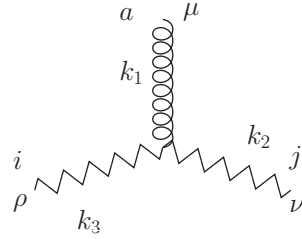


where

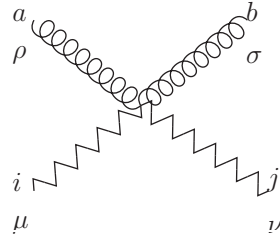
$$g_{\text{LQ}} = \begin{cases} h_{1L} & (\lambda = -1) \\ h_{1R} & (\lambda = +1) \end{cases}$$

and  $\lambda$  is the helicity of the electron.

QCD vertices



$$\begin{aligned}
 & igT_{ji}^a \left( g_{\mu\nu}(k_1 - k_2)_\rho \right. \\
 & \quad + g_{\nu\rho}(k_2 - k_3)_\mu \\
 & \quad \left. + g_{\rho\mu}(k_3 - k_1)_\nu \right)
 \end{aligned}$$



$$\begin{aligned}
 & -ig^2 \left( (T^a T^b)_{ji} (g_{\mu\nu} g_{\rho\sigma} - g_{\mu\rho} g_{\nu\sigma}) \right. \\
 & \quad + (T^b T^a)_{ji} (g_{\mu\nu} g_{\rho\sigma} - g_{\mu\sigma} g_{\nu\rho}) \\
 & \quad \left. + [T^a, T^b]_{ji} (g_{\nu\rho} g_{\mu\sigma} - g_{\mu\rho} g_{\nu\sigma}) \right)
 \end{aligned}$$

## Goldstone vertices

$$igT_{ji}^a(k_1 - k_2)_\mu$$

$$igT_{ji}^a m_{LQ} g_{\mu\nu}$$

$$-ig^2\{T^a, T^b\}_{ji} g_{\mu\nu}$$

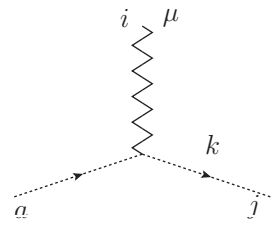
## Ghost vertices

$$gf^{abc} k_\mu$$

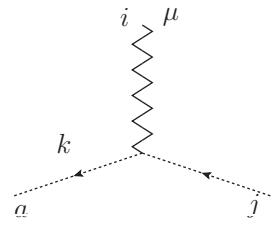
$$-igT_{ji}^a k_\mu$$

$$igT_{ji}^a k_\mu$$

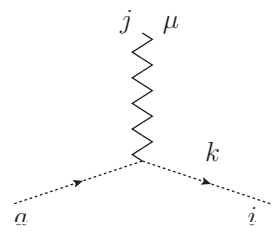




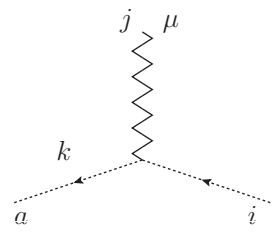
$$igT_{ji}^a k_\mu$$



$$-igT_{ji}^a k_\mu$$



$$-igT_{ji}^a k_\mu$$



$$igT_{ji}^a k_\mu$$

# Appendix D

## External Leg Corrections

The external leg corrections, as discussed in the main text, have been done analytically and are detailed here. The first section details the case where the external leg corrections involve a scalar LQ and the second section details the case for a vector LQ.

### D.1 External Leg Corrections: Scalar Leptoquark

The external leg correction for a massless u-quark is described in the main text (see section 3.2.3) and the corrections for the remaining external leg corrections are described in the following sections.

#### D.1.1 The Electron and Positron

The wavefunction renormalisation factor calculations for the outgoing massless electron and positron  $Z_{e\pm}$  are essentially the same as for the u-quark (see section 3.2.3) with the exception that there are no QCD corrections. The Feynman diagrams for these corrections are shown in fig D.1. The final result for the electron and positron



**Figure D.1:** *External leg corrections to the outgoing positron and electron.*

is

$$\sqrt{Z_{e^\pm}} \approx 1 + \frac{1}{16\pi^2} \left[ g_W^2 \left( \frac{2}{\epsilon} - 2 \log \left( \frac{M_W^2}{\mu^2} \right) + 1 \right) + g_{Z(e)}^2 \left( \frac{2}{\epsilon} - 2 \log \left( \frac{M_Z^2}{\mu^2} \right) + 1 \right) + g_{LQ}^2 \left( \frac{1}{\epsilon} - \log \left( \frac{M_{LQ}^2}{\mu^2} \right) + \frac{1}{2} \right) \right] \quad (\text{D.1})$$

where  $g_W$  and  $g_{LQ}$  are the respective couplings for the W-boson and LQ and  $g_{Z(e)}$  is the coupling of the Z-boson to the electron and positron. In general these couplings are functions of the u-quark helicity and are defined in appendix C.

### D.1.2 The Gluon

The wavefunction renormalisation factor for the gluon leg can be calculated from

$$Z_g^{-1} = 1 - \Pi(0) \quad (\text{D.2})$$

where  $i\Pi(p^2)$  represents the 1-loop diagrams as shown in fig D.2.

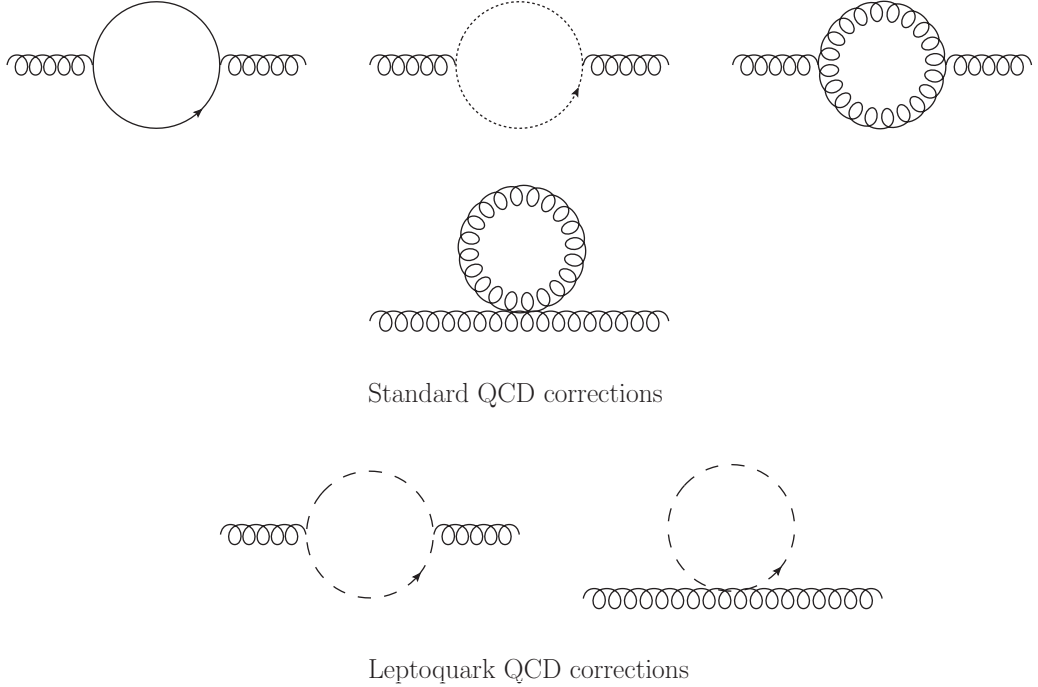


**Figure D.2:** *External leg corrections to the incoming gluon.*

Since  $\Pi(0) \ll 1$  this means eq.(D.2) can be written as

$$\sqrt{Z_g} \approx 1 + \frac{1}{2}\Pi(0) = 1 + \frac{1}{2}\delta Z_g \quad (\text{from eq.(B.11)}) \quad (\text{D.3})$$

The  $\delta Z_g$  term is a sum of the standard QCD corrections with addition of leptoquark QCD corrections. Each of these corrections is either of the form given in eq.(B.13) (for bubble corrections) or of the form given in eq.(B.16) (for tadpoles). Since the standard QCD corrections only involve massless particles it is only the leptoquark QCD corrections which contribute to  $\delta Z_g$ .

From appendix B the final result for  $\sqrt{Z_g}$  is

$$\sqrt{Z_g} \approx 1 + \frac{1}{16\pi^2} \frac{g^2}{6} \left[ \frac{1}{\epsilon} - \log \left( \frac{m_{\text{LQ}}^2}{\mu^2} \right) \right] \quad (\text{D.4})$$

*Note: Since there is a doublet of LQs in  $R_2$  the result in eq.(D.4) has been multiplied by a factor of two to account for the fact that there are two types of LQs in the loops in fig D.2.*

### D.1.3 The Leptoquark

The wavefunction renormalisation factor for a scalar LQ can be calculated from

$$Z_{\text{LQ}}^{-1} = 1 - \left. \frac{d\Sigma}{dp^2} \right|_{p^2=m_{\text{LQ}}^2} \quad (\text{D.5})$$

where  $-i\Sigma$  represent the sum 1-loop corrections shown in figure D.3, each of which has the form shown in eq.(B.22) or eq.(B.23). The QCD tadpole diagram is omitted because its contribution is zero, the only contribution to the electroweak tadpole occurs when there is a massive W or Z-boson in the loop. As in the previous examples we have

$$\sqrt{Z_{\text{LQ}}} \approx 1 + \frac{1}{2} \left. \frac{d\Sigma}{dp^2} \right|_{p^2=m_{\text{LQ}}^2} = 1 + \frac{1}{2}\delta Z_{\text{LQ}} \quad (\text{D.6})$$

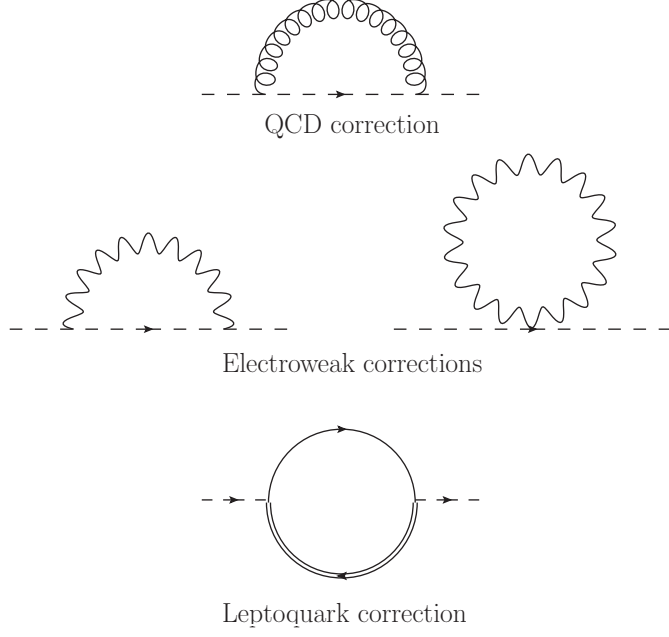


**Figure D.3:** *External leg corrections to the leptoquark.*

From appendix B the final result for  $\sqrt{Z_{\text{LQ}}}$  is

$$\begin{aligned}
\sqrt{Z_{\text{LQ}}} \approx & 1 + \frac{1}{16\pi^2} \left[ g^2 \left( \frac{1}{\epsilon} - \log \left( \frac{m_{\text{LQ}}^2}{\mu^2} \right) + 2 \right) - 2g^2 \left( \frac{1}{2\epsilon} + 1 - \frac{1}{2} \log \left( \frac{m_{\text{LQ}}^2}{\mu^2} \right) \right) \right. \\
& + g_W^2 \left( I_1(\alpha_+, \alpha_-) - 2I_2(\alpha_+, \alpha_-) \right) + g_{Z(\text{LQ})}^2 \left( I_1(\beta_+, \beta_-) - 2I_2(\beta_+, \beta_-) \right) \\
& \left. + g_{A(\text{LQ})}^2 \left( \frac{1}{\epsilon} - \log \left( \frac{m_{\text{LQ}}^2}{\mu^2} \right) + 2 \right) + g_{\text{LQ}}^2 \left( \frac{1}{\epsilon} - \log \left( \frac{m_{\text{LQ}}^2}{\mu^2} \right) + 1 \right) \right] \quad (\text{D.7})
\end{aligned}$$

where  $g_{Z(\text{LQ})}$  and  $g_{A(\text{LQ})}$  are the Z-boson and photon couplings to the LQ as defined in appendix C and where

$$\begin{aligned}
I_1(x_+, x_-) = & \frac{1}{\epsilon} - \log \left( \frac{m_{\text{LQ}}^2}{\mu^2} \right) + 2 - (1 - x_+) \log(1 - x_+) - x_+ \log(-x_+) \\
& - (1 - x_-) \log(1 - x_-) - x_- \log(-x_-) \quad (\text{D.8})
\end{aligned}$$

$$I_2(x_+, x_-) = 1 - x_+ \frac{(1 - x_+)}{(x_+ - x_-)} \log \left( 1 - \frac{1}{x_+} \right) - x_- \frac{(1 - x_-)}{(x_- - x_+)} \log \left( 1 - \frac{1}{x_-} \right) \quad (\text{D.9})$$

with

$$\alpha_{\pm} = \frac{m_W^2}{2m_{\text{LQ}}^2} \pm \sqrt{\frac{m_W^4}{4m_{\text{LQ}}^4} - \frac{m_W^2}{m_{\text{LQ}}^2}} \quad (\text{D.10})$$

$$\beta_{\pm} = \frac{m_Z^2}{2m_{\text{LQ}}^2} \pm \sqrt{\frac{m_Z^4}{4m_{\text{LQ}}^4} - \frac{m_Z^2}{m_{\text{LQ}}^2}} \quad (\text{D.11})$$

## D.2 External Leg Corrections: Vector Leptoquark

For the vector LQ case only QCD corrections are being considered. The analytic results to the various external legs are given in this section.

### D.2.1 The Massless Fermions

For the massless fermions the only QCD corrections are to the d-quark and since the loop diagrams only involve massless particles the external d-quark corrections are zero.

### D.2.2 The Gluon

As with the scalar LQ case the only non-zero corrections to gluon come from the vector LQ bubble and tadpole diagrams. Being a gauge boson the vector LQ loop has additional contributions from Goldstone bosons and Faddeev-Popov ghosts as shown in figure D.4. From appendix B the final result for  $\sqrt{Z_g}$  is

$$\sqrt{Z_g} \approx 1 + \frac{1}{16\pi^2} g^2 \left[ \frac{5}{\epsilon} + \frac{17}{3} - 5 \log \left( \frac{m_{\text{LQ}}^2}{\mu^2} \right) \right] \quad (\text{D.12})$$

### D.2.3 The Leptoquark

The loop corrections to the LQ also involve Goldstone bosons and Faddeev-Popov ghost and have the same topologies as shown in figure 4.2. The wavefunction renormalisation factor for the LQ can be calculated from

$$Z_{\text{LQ}}^{-1} = 1 - \Pi(m_{\text{LQ}}^2) \quad (\text{D.13})$$

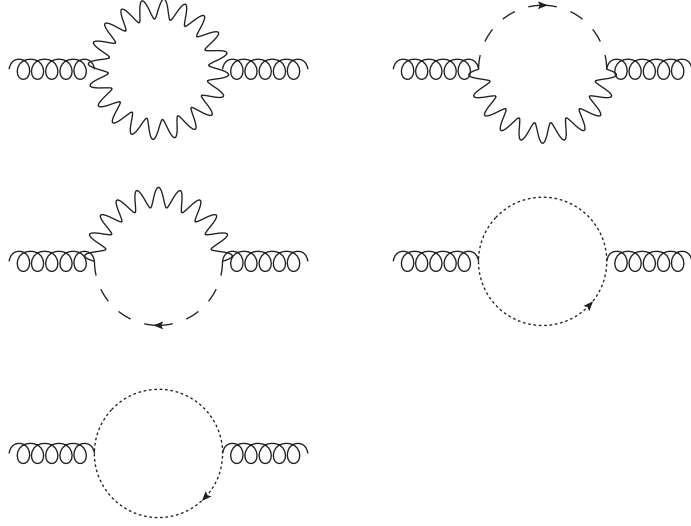


**Figure D.4:** *The external leg corrections to the gluon including the Goldstone boson and Faddeev-Popov ghost contributions.*

where  $i\Pi(p^2)$  represents the 1-loop corrections as shown in figure 4.2.

Since  $\Pi(m_{\text{LQ}}^2) \ll 1$  from eq. (D.13) we have

$$\sqrt{Z_{\text{LQ}}} \approx 1 + \frac{1}{2}\Pi(m_{\text{LQ}}^2) = 1 + \frac{1}{2}\delta Z_{\text{LQ}} \quad (\text{from eq. (B.40)}) \quad (\text{D.14})$$

From appendix B the final result for  $\sqrt{Z_{\text{LQ}}}$  is

$$\sqrt{Z_{\text{LQ}}} \approx 1 + \frac{1}{16\pi^2} \frac{g^2}{9} \left[ \frac{57}{\epsilon} + 101 - 57 \log \left( \frac{m_{\text{LQ}}^2}{\mu^2} \right) \right] \quad (\text{D.15})$$

## Appendix E

# Lorentz Invariant Phase-Spaces

Calculating the various cross-sections and decay-widths requires suitable choices for the parametrisation of the Lorentz invariant phase-spaces. In this appendix we will detail the various phase space parametrisations used in this project.

### E.1 Phase-Spaces for Scattering Processes

Scattering processes have a 2-body initial state and for these processes the initial states with momenta  $p_1$  and  $p_2$  are massless and the outgoing states with momenta  $q_i$  contain at most one massive state.

#### E.1.1 2-Body Phase-Space with a Massive Final State

The incoming momenta  $p_1$  and  $p_2$  are defined in the centre-of-mass (COM) frame as

$$p_1 = \frac{\sqrt{s}}{2} [1, 0, 0, 1]^T \tag{E.1}$$

$$p_2 = \frac{\sqrt{s}}{2} [1, 0, 0, -1]^T \tag{E.2}$$

where  $\sqrt{s}$  is the COM collision energy.



Choosing  $q_1$  to be the massive outgoing state with mass  $m$ , this is defined as

$$q_1 = \left[ \frac{s + m^2}{2\sqrt{s}}, \frac{\sqrt{\lambda(s, m^2, 0)}}{2\sqrt{s}} \hat{\mathbf{n}} \right]^T \quad (\text{E.3})$$

where  $\lambda(x, y, z) = x^2 + y^2 + z^2 - 2xy - 2xz - 2yz$  and  $\hat{\mathbf{n}} = [\sin \theta, 0, \cos \theta]^T$  with  $\theta$  being the azimuthal angle in the COM system. By conservation of momentum the massless outgoing state is  $q_2 = p_1 + p_2 + q_1$ . With this choice of parametrisation the 2-body phase space is

$$\int d^2_{\text{LIPS}} = \frac{1}{2\pi} \frac{(s - m^2)}{8s} \int_{-1}^1 d \cos \theta \quad (\text{E.4})$$

This phase-space measure can also be used for massless final states by setting  $m^2 = 0$ .

For the dipole subtraction method it is necessary to use a scaled 2-body Lorentz invariant phase-space where either  $p_1$  or  $p_2$  is scaled by a variable  $x$  with being in the range  $[0,1]$ . Since the phase-space is Lorentz invariant one can still work in the COM frame by scaling both  $p_1$  and  $p_2$  by  $\sqrt{x}$ . This gives the scale 2-body phase space as

$$\int d^2_{\text{LIPS}}(x) = \frac{1}{2\pi} \frac{(xs - m^2)}{8xs} \int_{-1}^1 d \cos \theta \quad (\text{E.5})$$

### E.1.2 3-Body Phase-Space with a Massive Final State

The incoming momenta  $p_1$  and  $p_2$  are defined as before and the outgoing momenta  $q_1$  and  $q_2$  are chosen to be the massless states with a relative angle  $\theta$  between them. These are then rotated into a general direction by the angles  $\alpha$  and  $\beta$  to give

$$q_1 = Ex \begin{bmatrix} 1 \\ \sin \alpha \cos \theta + \cos \alpha \cos \beta \sin \theta \\ \sin \beta \sin \theta \\ \cos \alpha \cos \theta - \sin \alpha \cos \beta \sin \theta \end{bmatrix} \quad (\text{E.6})$$

$$q_2 = E(1 - x) [1, \sin \alpha, 0, \cos \alpha]^T \quad (\text{E.7})$$

where

$$E = \frac{(s + m_{12}^2 - m^2)}{2\sqrt{s}} \quad (\text{E.8})$$

The quantity  $m_{12}^2$  is the invariant squared mass of the  $q_1$ - $q_2$  system. It is parametrised by the variable  $y$  as

$$m_{12}^2 = (\sqrt{s} - m)^2 y \quad (\text{E.9})$$

The quantity  $x$  defines the ratio of energy shared between  $q_1$  and  $q_2$ . It is parametrised by the variable  $w$  as

$$x = \frac{1 - v}{2} + vw \quad (\text{E.10})$$

where

$$v = \frac{\sqrt{\lambda(s, m_{12}^2, m^2)}}{s + m_{12}^2 - m^2} \quad (\text{E.11})$$

By momentum conservation, and from the above definitions, the massive outgoing state with mass  $m$  is  $q_3 = p_1 + p_2 - q_1 - q_2$ .

With this parametrisation the 3-body phase-space is

$$\int d^3_{\text{LIPS}} = \frac{1}{(2\pi)^4} \int_0^1 dw \int_0^1 dy \int_{-1}^1 d\cos\alpha \int_0^{2\pi} d\beta \frac{(s + m_{12}^2 - m^2)}{32s} \frac{m_{12}^2}{y} v \quad (\text{E.12})$$

As before this phase-space can be used for a massless final state by setting  $m^2 = 0$ .

This choice of parametrisation makes it possible to identify the relevant infrared divergent regions of the phase-space. If we treat  $q_2$  as the radiated bremsstrahlung particle then for example  $p_1 \cdot q_2 \rightarrow 0$  occurs when  $\cos\alpha \rightarrow 1$  and  $p_2 \cdot q_2 \rightarrow 0$  occurs when  $\cos\alpha \rightarrow -1$ .

### E.1.3 4-Body Phase-Space with Massless Final States

For the 4-body phase-space all outgoing particles are massless. For parametrising this phase space the incoming momenta  $p_1$  and  $p_2$  are rotated by angles  $\alpha$  and  $\beta$

giving

$$p_1 = \frac{\sqrt{s}}{2} [1, \sin \alpha \cos \beta, \sin \alpha \sin \beta, \cos \alpha]^T \quad (\text{E.13})$$

$$p_2 = \frac{\sqrt{s}}{2} [1, -\sin \alpha \cos \beta, -\sin \alpha \sin \beta, -\cos \alpha]^T \quad (\text{E.14})$$

In the  $q_1$ - $q_2$  rest-frame the momenta  $q_1$  and  $q_2$  can be defined by the angles  $\theta$  and  $\phi$ .

Boosting to the  $p_1$ - $p_2$  COM frame gives

$$q_1 = \frac{\sqrt{s_{12}}}{2} [\gamma + v\gamma \cos \theta, \cos \theta \sin \phi, \sin \theta \sin \phi, \gamma \cos \theta + v\gamma]^T \quad (\text{E.15})$$

$$q_2 = \frac{\sqrt{s_{12}}}{2} [\gamma - v\gamma \cos \theta, -\cos \theta \sin \phi, -\sin \theta \sin \phi, -\gamma \cos \theta + v\gamma]^T \quad (\text{E.16})$$

$$(\text{E.17})$$

where

$$\gamma = \frac{1}{\sqrt{s_{12}}} \left( \frac{s + s_{12} - s_{34}}{2\sqrt{s}} \right) \quad (\text{E.18})$$

$$v\gamma = \frac{1}{\sqrt{s_{12}}} \frac{\sqrt{\lambda(s, s_{12}, s_{34})}}{2\sqrt{s}} \quad (\text{E.19})$$

with  $s_{12}$  and  $s_{34}$  parametrised by  $x_1$  and  $x_2$  as

$$\sqrt{s_{12}} = \sqrt{s} x_1 (1 - x_2) \quad (\text{E.20})$$

$$\sqrt{s_{34}} = \sqrt{s} x_1 x_2 \quad (\text{E.21})$$

In the  $q_3$ - $q_4$  rest-frame the momenta  $q_3$  and  $q_4$  can be defined by the angle  $\psi$ . Boosting

to the  $p_1$ - $p_2$  COM frame gives

$$q_3 = \frac{\sqrt{s_{34}}}{2} [\gamma - v\gamma \cos \psi, \sin \psi, 0, \gamma \cos \psi - v\gamma]^T \quad (\text{E.22})$$

$$q_4 = \frac{\sqrt{s_{34}}}{2} [\gamma + v\gamma \cos \psi, -\sin \psi, 0, -\gamma \cos \psi - v\gamma]^T \quad (\text{E.23})$$

where

$$\gamma = \frac{1}{\sqrt{s_{34}}} \left( \frac{s + s_{34} - s_{12}}{2\sqrt{s}} \right) \quad (\text{E.24})$$

$$v\gamma = \frac{1}{\sqrt{s_{34}}} \frac{\sqrt{\lambda(s, s_{34}, s_{12})}}{2\sqrt{s}} \quad (\text{E.25})$$

The  $q_3$ - $q_4$  system needs to be rotated so that  $q_4$  is along the  $z$ -axis. This can be achieved by rotating the  $x$  and  $z$  components of  $q_3$  and  $q_4$  so that

$$q_i^{(x)} \rightarrow q_i^{(x)} \cos \eta - q_i^{(z)} \sin \eta \quad (\text{E.26})$$

$$q_i^{(z)} \rightarrow q_i^{(x)} \sin \eta + q_i^{(z)} \cos \eta \quad (i = 3, 4) \quad (\text{E.27})$$

where  $\eta$  is defined by

$$\tan \eta = \frac{\sin \psi}{\gamma \cos \psi + v\gamma} \quad (\text{E.28})$$

With this parametrisation the 4-body phase-space is

$$\begin{aligned} \int d^4_{\text{LIPS}} = \frac{1}{(2\pi)^7} \frac{s}{128} \int_0^1 dx_1 \int_0^1 dx_2 \int_{-1}^1 d\cos \alpha \int_0^{2\pi} d\beta \\ \int_{-1}^1 d\cos \theta \int_0^{2\pi} d\phi \int_{-1}^1 d\cos \psi x_1^3 x_2 (1 - x_2) \sqrt{\lambda(s, s_{12}, s_{34})} \end{aligned} \quad (\text{E.29})$$

This choice of parametrisation makes it possible to identify the relevant infrared divergent regions of the phase-space. If we treat  $q_4$  as the radiated bremsstrahlung particle then for example  $p_1 \cdot q_4 \rightarrow 0$  occurs when  $\cos \alpha \rightarrow 1$  and  $p_2 \cdot q_4 \rightarrow 0$  occurs when  $\cos \alpha \rightarrow -1$ .

## E.2 Phase-Spaces for Decay Processes

In comparison to the production processes the decay processes have a single massive initial state. This section describes the parametrisation of the phase-spaces for such processes. For a decay processes the initial state has momenta  $p$  and mass  $m$  and the outgoing states with momenta  $q_i$  are assumed massless.

### E.2.1 2-Body Phase-Space

In the rest-frame of  $p$  the incoming momentum is

$$p = m [1, 0, 0, 0]^T \quad (\text{E.30})$$

and the outgoing momenta are

$$q_1 = \frac{m}{2} [1, 0, 0, 1]^T \quad (\text{E.31})$$

$$q_2 = \frac{m}{2} [1, 0, 0, -1]^T \quad (\text{E.32})$$

This gives the trivial phase-space integral as

$$\int d_{\text{LIPS}}^2 = \frac{1}{8\pi} \quad (\text{E.33})$$

### E.2.2 3-Body Phase-Space

The 3-body phase-space for the decay process needs to be treated differently to all the other phase-space integrals. As discussed in the main text the infrared divergences coming from bremsstrahlung can be dealt with analytically by performing the integral over the momentum of the bremsstrahlung particle in  $d = 4 - 2\epsilon$  dimensions.

With the incoming momentum described as given in eq.(E.30) the outgoing momenta can be parametrised as

$$q_1 = \frac{x m_{\text{LQ}}}{2} [1, 0, 0, 1]^T \quad (\text{E.34})$$

$$k = \frac{y m_{\text{LQ}}}{2} [1, \sin \theta, 0, \cos \theta]^T \quad (\text{E.35})$$

where  $k$  is the momenta of bremsstrahlung particle and the final outgoing momenta is  $q_2 = p - q_1 - k$ . The angle  $\cos \theta$  is given in terms of the parameter  $z$  as

$$\cos \theta = 1 - 2z \quad (\text{E.36})$$

and constraints on the momenta give

$$x = \frac{(1-y)}{(1-yz)} \quad (\text{E.37})$$

With this choice of parametrisation and the momentum  $k$  evaluated in  $d = 4 - 2\epsilon$  dimensions the 3-body phase-space integral is

$$\begin{aligned} \int d^3_{\text{LIPS}} &= d^2_{\text{LIPS}} \times \frac{1}{16\pi^2} m_{\text{LQ}}^2 \left( \frac{m_{\text{LQ}}^2}{\mu^2} \right)^{-\epsilon} \int_0^1 dy \int_0^1 dz \frac{1-y}{(1-yz)^2} y^{1-2\epsilon} z^{-\epsilon} (1-z)^{-\epsilon} \\ &= \frac{1}{8\pi} \times \frac{1}{16\pi^2} m_{\text{LQ}}^2 \left( \frac{m_{\text{LQ}}^2}{\mu^2} \right)^{-\epsilon} \int_0^1 dy \int_0^1 dz \frac{1-y}{(1-yz)^2} y^{1-2\epsilon} z^{-\epsilon} (1-z)^{-\epsilon} \end{aligned} \quad (\text{E.38})$$

where  $d^2_{\text{LIPS}} = \frac{1}{8\pi}$  is the trivial two-body phase-space.

# Bibliography

- [1] S. L. Glashow, *Partial Symmetries of Weak Interactions*, *Nucl. Phys.* **22** (1961) 579–588.
- [2] S. Weinberg, *A Model of Leptons*, *Phys. Rev. Lett.* **19** (1967) 1264–1266.
- [3] A. Salam, *Weak and Electromagnetic Interactions*, . Originally printed in \*Svartholm: Elementary Particle Theory, Proceedings Of The Nobel Symposium Held 1968 At Lerum, Sweden\*, Stockholm 1968, 367-377.
- [4] J. C. Pati and A. Salam, *Lepton Number as the Fourth Color*, *Phys.Rev.* **D10** (1974) 275–289.
- [5] H. Georgi and S. Glashow, *Unity of All Elementary Particle Forces*, *Phys.Rev.Lett.* **32** (1974) 438–441.
- [6] **Particle Data Group** Collaboration, K. Olive *et al.*, *Review of Particle Physics*, *Chin.Phys.* **C38** (2014) 090001.
- [7] W. Buchmuller, R. Ruckl, and D. Wyler, *Leptoquarks in Lepton - Quark Collisions*, *Phys.Lett.* **B191** (1987) 442–448.
- [8] J. Blumlein, E. Boos, and A. Kryukov, *Leptoquark pair production in hadronic interactions*, *Z.Phys.* **C76** (1997) 137–153, [[hep-ph/9610408](#)].
- [9] A. Belyaev, C. Leroy, R. Mehdiyev, and A. Pukhov, *Leptoquark single and pair production at LHC with CalcHEP/CompHEP in the complete model*, *JHEP* **0509** (2005) 005, [[hep-ph/0502067](#)].

- [10] **CMS Collaboration** Collaboration, V. Khachatryan *et al.*, *Search for pair production of third-generation scalar leptoquarks and top squarks in proton-proton collisions at  $\sqrt{s} = 8$  TeV*, 1408.0806.
- [11] **ATLAS Collaboration** Collaboration, G. Aad *et al.*, *Search for third generation scalar leptoquarks in pp collisions at  $\sqrt{s} = 7$  TeV with the ATLAS detector*, *JHEP* **1306** (2013) 033, [1303.0526].
- [12] **ATLAS Collaboration** Collaboration, G. Aad *et al.*, *Search for second generation scalar leptoquarks in pp collisions at  $\sqrt{s} = 7$  TeV with the ATLAS detector*, *Eur.Phys.J.* **C72** (2012) 2151, [1203.3172].
- [13] **ATLAS Collaboration** Collaboration, G. Aad *et al.*, *Search for first generation scalar leptoquarks in pp collisions at  $\sqrt{s} = 7$  TeV with the ATLAS detector*, *Phys.Lett.* **B709** (2012) 158–176, [1112.4828].
- [14] D. Berdine, N. Kauer, and D. Rainwater, *Breakdown of the Narrow Width Approximation for New Physics*, *Phys.Rev.Lett.* **99** (2007) 111601, [hep-ph/0703058].
- [15] N. Kauer, *Narrow-width approximation limitations*, *Phys.Lett.* **B649** (2007) 413–416, [hep-ph/0703077].
- [16] N. Kauer, *A Threshold-improved narrow-width approximation for BSM physics*, *JHEP* **0804** (2008) 055, [0708.1161].
- [17] G. Passarino and M. Veltman, *One-loop corrections for  $e+e$  annihilation into  $+$  in the weinberg model*, *Nuclear Physics B* **160** (1979), no. 1 151 – 207.
- [18] R. K. Ellis, W. Giele, and Z. Kunszt, *A Numerical Unitarity Formalism for Evaluating One-Loop Amplitudes*, *JHEP* **0803** (2008) 003, [0708.2398].
- [19] G. Ossola, C. G. Papadopoulos, and R. Pittau, *Reducing full one-loop amplitudes to scalar integrals at the integrand level*, *Nucl.Phys.* **B763** (2007) 147–169, [hep-ph/0609007].
- [20] G. Ossola, C. G. Papadopoulos, and R. Pittau, *CutTools: A Program implementing the OPP reduction method to compute one-loop amplitudes*,



- JHEP* **0803** (2008) 042, [0711.3596].
- [21] T. Binoth, J.-P. Guillet, G. Heinrich, E. Pilon, and T. Reiter, *Golem95: A Numerical program to calculate one-loop tensor integrals with up to six external legs*, *Comput.Phys.Commun.* **180** (2009) 2317–2330, [0810.0992].
  - [22] P. Mastrolia, G. Ossola, T. Reiter, and F. Tramontano, *Scattering AMplitudes from Unitarity-based Reduction Algorithm at the Integrand-level*, *JHEP* **1008** (2010) 080, [1006.0710].
  - [23] A. van Hameren, *OneLOop: For the evaluation of one-loop scalar functions*, *Comput.Phys.Commun.* **182** (2011) 2427–2438, [1007.4716].
  - [24] R. K. Ellis and G. Zanderighi, *Scalar one-loop integrals for QCD*, *JHEP* **0802** (2008) 002, [0712.1851].
  - [25] T. Kinoshita, *Mass singularities of feynman amplitudes*, *Journal of Mathematical Physics* **3** (1962), no. 4 650–677.
  - [26] T. D. Lee and M. Nauenberg, *Degenerate systems and mass singularities*, *Phys. Rev.* **133** (Mar, 1964) B1549–B1562.
  - [27] G. Altarelli and G. Parisi, *Asymptotic freedom in parton language*, *Nuclear Physics B* **126** (1977), no. 2 298 – 318.
  - [28] B. Harris and J. Owens, *The Two cutoff phase space slicing method*, *Phys.Rev.* **D65** (2002) 094032, [hep-ph/0102128].
  - [29] S. Catani, S. Dittmaier, M. H. Seymour, and Z. Trocsanyi, *The Dipole formalism for next-to-leading order QCD calculations with massive partons*, *Nucl.Phys.* **B627** (2002) 189–265, [hep-ph/0201036].
  - [30] T. O. Eynck, E. Laenen, L. Phaf, and S. Weinzierl, *Comparison of phase space slicing and dipole subtraction methods for  $\gamma^* \rightarrow Q\bar{Q}$* , *Eur.Phys.J.* **C23** (2002) 259–266, [hep-ph/0109246].
  - [31] J. Pumplin, D. Stump, J. Huston, H. Lai, P. M. Nadolsky, *et al.*, *New generation of parton distributions with uncertainties from global QCD analysis*, *JHEP* **0207** (2002) 012, [hep-ph/0201195].

- [32] D. Stump, J. Huston, J. Pumplin, W.-K. Tung, H. Lai, *et al.*, *Inclusive jet production, parton distributions, and the search for new physics*, *JHEP* **0310** (2003) 046, [[hep-ph/0303013](#)].
- [33] H. Lehmann, K. Symanzik, and W. Zimmermann, *Zur formulierung quantisierter feldtheorien*, *Il Nuovo Cimento* **1** (1955), no. 1 205–225.
- [34] M. E. Peskin and D. V. Schroeder, *An Introduction To Quantum Field Theory*. Westview Press, 1995.
- [35] J. A. M. Vermaseren, *New features of FORM*, *ArXiv Mathematical Physics e-prints* (Oct., 2000) [[math-ph/0010025](#)].
- [36] W. Siegel, *Supersymmetric dimensional regularization via dimensional reduction*, *Physics Letters B* **84** (1979), no. 2 193 – 196.
- [37] A. Martin, R. Roberts, W. Stirling, and R. Thorne, *Parton distributions incorporating QED contributions*, *Eur.Phys.J.* **C39** (2005) 155–161, [[hep-ph/0411040](#)].
- [38] A. Belyaev, N. D. Christensen, and A. Pukhov, *CalcHEP 3.4 for collider physics within and beyond the Standard Model*, *Comput.Phys.Commun.* **184** (2013) 1729–1769, [[1207.6082](#)].
- [39] R. Ellis, D. Ross, and A. Terrano, *The perturbative calculation of jet structure in  $e+e$  annihilation*, *Nuclear Physics B* **178** (1981), no. 3 421 – 456.
- [40] G. 't Hooft and M. Veltman, *Regularization and renormalization of gauge fields*, *Nuclear Physics B* **44** (1972), no. 1 189 – 213.